May 2014

Fabric and Microstructural Analysis of the Loch Borralan Pluton, Northwest Highlands, Scotland

Justin Calhoun
University of Wisconsin-Milwaukee

FABRIC AND MICROSTRUCTURAL ANALYSIS OF THE LOCH BORRALAN PLUTON, NORTHWEST HIGHLANDS, SCOTLAND

by

Justin Calhoun

A Thesis Submitted in

Partial Fulfillment of the

Requirements for the Degree of

Master of Science

in Geosciences

at

The University of Wisconsin-Milwaukee

May 2014

ABSTRACT

FABRIC AND MICROSTRUCTURAL ANALYSIS OF THE LOCH BORRALAN PLUTON, NORTHWEST HIGHLANDS, SCOTLAND

by

Justin Calhoun

The University of Wisconsin-Milwaukee, 2014
Under the Supervision of Professor Dr. Dyanna Czeck

The Loch Borralan pluton was emplaced within the Assynt Region of the Moine Thrust zone during the Scandian event (ca. 435-425 Ma) of the Caledonian Orogeny (478-425 Ma). It consists of two major magma suites, the syenitic early suite (431.1 ± 1.2 Ma), and the quartz syenitic later suite (429.2 ± 0.5 Ma). The region is characterized by a series of in-sequence thrust faults that strike NE-SW and dip approximately 20° to the SE, including (from lower to upper): the Sole Thrust, the Borralan Thrust (hypothesized, but not exposed), the Ben More Thrust, and the Moine Thrust. A series of imbricate thrusts between the Sole and Borralan Thrusts juxtapose repeated Cambrian and Ordovician strata. The Loch Borralan pluton intruded between the Sole and Ben More thrust faults, and may be bounded below by a hypothesized Borralan Thrust fault. Based on the overlap in pluton crystallization age and orogenic activity, the combination of macroscopic field lineation and foliation measurements, anisotropy of magnetic susceptibility (AMS) lineation and foliations measurements, mineral shape preferred orientation (SPO) analysis, and petrographic deformation microstructure analysis will be used to determine if the pluton expresses deformation features and fabrics corresponding to thrust fault tectonics.

The dominant magnetic mineralogy as determined by thermomagnetic data and hysteresis plots was determined to be magnetite and titanomagnetite. Some paramagnetic

components were seen in the early suite, and can be attributed to biotite. Both minerals contributed to the AMS signal that was used to interpret pluton fabrics.

The pluton contains S>L (foliation stronger than lineation) fabrics throughout, defined by alignment of alkali feldspar grains. The foliation strike of both the early and late suites are subparallel to the thrust faults, providing evidence that the fabrics are related to deformation.

The early suite is only well exposed in the southeast at the top of the Borralan thrust sheet, and proximal to the bottom of the Ben More Thrust fault. Foliations strike approximately 030 and dip 20° SE. Mineral lineations were not readily seen in the early suite. AMS results show mean principal susceptibilities ($K_1>K_2>K_3$) parallel to field measurements.

Mineral foliations in the late suite have a similar strike to early suite foliations, but dip roughly 50-60° both to the NW and SE. AMS foliations parallel mineral foliations, and strike generally NE-SW. AMS foliation dips are more variable, spanning the range of possible dip angles. The variance in foliation dips are likely caused by a composite magnetic fabric resulting from thrusting combined with thrust parallel flattening. Lineations in the late suite are scarce, but generally plunge shallowly to the NE and SW indicating horizontal extrusion parallel to the strike of the thrust faults. Similarly, most late suite AMS lineations plunge shallowly perpendicular to thrust transport direction corroborating the field measurements. Some late suite AMS lineations plunge parallel to thrust transport direction, suggesting there are also components of simple shear related to thrusting, with partitioning varying throughout the late suite.

The foliation dip degree variation between the two suites could be the result of the spatial relationships and/or timing. The pluton is interpreted to have been emplaced syn-kinematically, deformed via thrusting related simple shear in the early suite, and with a component of flattening and lateral extrusion added in the late suite.

Shape preferred orientation (SPO) measurements were conducted using the intercept method of image analysis to relate mineral fabrics to AMS measurements. SPO are generally weak, and have low shape ratio values. Mineral orientation parallels magnetic mineral fabric within each thin section, which supports AMS measurements as representative of mineral fabric.

Petrographic microstructural thin section analysis was performed to analyze deformation mechanisms to deformation conditions. Feldspars exhibited both crystal plastic (ductile) and brittle microstructures. Examples of crystal plastic microstructures seen in feldspars include: perthite and myrmekite, undulose extinction, grain boundary bulging. Feldspars also showed quartz filled fractures (brittle deformation), which occasionally formed conjugate sets relative to AMS principal susceptibilities. Quartz was primarily seen only in the northwest extent of the pluton. Quartz also had both crystal plastic and brittle microstructures. Crystal plastic microstructures seen in quartz include: dynamic recrystallization, undulose extinction (recrystallized and primary grains), and grain boundary bulging. Examples of brittle microstructures in quartz are intragranular fractures. Deformation temperature conditions range from high grade to low grade. The presence of structures such as perthite and myrmekite textures infer deformation temperatures of around 600°C, and on the low end brittle deformation in either quartz or feldspars suggest sub 300°C. The range of deformation temperatures suggest that the

pluton was emplaced synkinematically and deformation continued throughout its cooling history.

The strong agreement between field and AMS measurements combined with evidence for high temperature deformation conditions suggests the pluton intruded syn-tectonically. The majority of deformation is seen in the early suite, and southeastern late suite. These locations are closest to the Ben More thrust, suggesting that movement along this thrust caused the majority of deformation. Based on AMS orientations, deformation in the early suite is accommodated as thrust motion related simple shear. Late suite deformation has a combination of thrusting simple shear, general flattening, and lateral extrusion. Since the pluton was likely roofed by thrust faults restricting upward flow, space for the magma was created through lateral extrusion.

Dedicated to those who love the Earth, and all of its inhabitants.

TABLE OF CONTENTS

LIST OF FIGURES

LIST OF TABLES

ACKNOWLEDGEMENTS

I would like to thank Dr. Dyanna Czeck, my advising professor, for her support and guidance throughout this project. She stayed right by me through thick and thin, and forced me to think in ways I've never thought before.

I'd like to thank my committee members Dr. Bill Kean, and Dr. Barry Cameron. Their thoughts and kind words put my work into perspective. Big thanks to Julie Bowles for helping me with the majority of my magnetic mineralogy characterization. It's unfortunate that the defense didn't work out with your field schedule.

I also thank Dr. Basil Tikoff for his help in starting this project with Dyanna, which ultimately brought me to a closer understanding of the earth than I ever dreamed possible. I will never forget singing songs while taking gravity measurements in peat forests. His enthusiasm in and out of the field reminds me of how lucky we are to be geologists.

I'd like to thank my long legged, scruffy, and talented field partner Jack Graham. It was a pleasure working with you, and you are wise beyond your years. I'm sure we've made our ancestors are proud.

Thanks to everyone who has helped fund this project; The UW-Milwaukee/UW-Madison Intercampus Research Incentive Grants Program, UW-Milwaukee Center for International Education Faculty/Academic Staff Travel Awards, The Geological Society of America Student Research Grant Program, and Wisconsin Geological Society Student Grant Program.

Thanks to Dr. Tom Hooyer for allowing me to use his kappabridge. Brian Hess at UW-Madison for his work on my thin sections, Mike Jackson at the Institute of Rock Magnetism for his help on the VSM, Jerry Becker in the UWM Machine Shop for getting the drill press working, and Alba at the Altnacaelgach Inn for giving two poor students a manageable rate at one of the most scenic locations in Scotland, thank you.

Thanks to Kathryn Goodenough for suggesting this project to Dyanna and Basil. Your research in the Highlands laid much of the groundwork needed to get this project in motion.

Finally, a big thanks to all my family and friends who never stopped believing in me, urged me to work harder, and kept me sane during this adventurous time of my life.

1. Introduction

1.1 Purpose of Study

The Loch Borralan pluton intruded between two thrust faults within the Moine Thrust Zone in the Assynt Region of Scotland. Recently developed crystallization ages of the pluton fall within the age of ductile movement along the Moine Thrust (Freeman et al. 1998 and Goodneough et al. 2011). The Loch Borralan pluton's deformational history is largely unknown due to the majority of the pluton contacts being unexposed, and discrete localized zones of deformation fabric seen in the field. Interpretations of whether or not the pluton is pre-, syn-, or post-kinematic have been discussed and revised over many years (Wooley 1970, van Breemen 1979; Searle et al. 2010, Goodenough et al. 2011). Recent workers believe the pluton is largely syn-kinematic (Searle et al. 2010 and Goodenough et al. 2011). In order to characterize deformation of the pluton a combination of macroscopic mineral measurements, anisotropy of magnetic susceptibility measurements (AMS), shape preferred orientation (SPO) analysis, and petrographic microstructural analysis were employed. The project aims to relate both the mineral and magnetic fabrics to regional thrust kinematics. Understanding the deformational history of this pluton will not only aid future workers in understanding the deformation history of the pluton and region, but it will also provide insight into how plutons behave within contractional tectonic regimes.

1.2 Fabrics in Deformed Igneous Rocks

A rock fabric is an ordered alignment of minerals in either planar or linear arrangements. Fabrics develop from different rotation rates of crystal shapes within

magma and/or by rotation or crystallization of minerals during deformation, which may be accompanied by metamorphism. Pluton fabrics record magmatic flow, deformation of crystallizing magma mush, and/or deformation of the solidified pluton during or after cooling. The fabric provides information on the magmatic flow geometries, regional tectonic strain during intrusion, and in some cases evidence for a tectonic overprint that formed during or post emplacement (Bouchez and Gleizes 1995, Pignotta and Benn 1999, and Zak et al. 2005).

Pluton fabrics that hold no geometric relationship to deformation features in the country rock represent the flow kinematics of the magma. There are three end-member types of magmatic fabric patterns (Figure 1.2.1; Paterson et al. 1998). One of the more common ways magmatic fabrics develop is in an ‘onion skin’ pattern in circular to sub-elliptical plutons. In ‘onion skin’ plutons, foliation intensity increases towards the pluton margins, and mineral lineations are weak throughout (Paterson et al. 1998). Another common pattern occurs in elongated plutons. The magmatic fabrics in these types of plutons form subparallel to the long dimensions of the intrusion and/or the regional structural trend (Paterson et al. 1998). The third end member occurs in plutons that have complex lobe geometries or batholith scale intrusions. These magmatic fabrics often are very complex and have little continuity with host rock patterns (Paterson et al. 1998). Complex fabrics are often a combination of the previously mentioned end members and are the most challenging to interpret (Paterson et al. 1998).

In the case of tectonically deformed granites, local textures can represent emplacement flow. However, these fabrics cannot be used to determine flow kinematics, because these textures have likely been overprinted to some degree by tectonic

deformation. In granites that are weakly deformed, the seemingly undeformed fabrics can be used as a tectonic strain indicator (Benn 2009). Bulk textures in tectonically deformed granite can be used to determine the style of deformation, the tectonic setting such as incidence of collision, and the kinematic partitioning behavior between the granite and host rock.

In order to differentiate between magmatic fabrics (first order processes) and structurally deformed fabrics (second order processes), the first step is always to measure and map all foliations and lineations. Then there are some field and laboratory observations that can aid in identifying the fabric type. In the field, finding features that indicate timing of fabric development of magmatic features, such as enclaves, layering, or contacts, to features formed during chamber construction, like stoped blocks and faults, and/or to features formed during regional deformation will give clues as to what to expect from the foliation and lineation measurements (Paterson et al. 1998). If such structures are visible then searching for deflections of fabrics across marker boundaries, or using geologic laws such as, the law of cross cutting relationships or the law of inclusions can be used to interpret the relative timing of emplacement. If the fabrics within markers are sporadic and discontinuous, then the fabrics are likely magmatic. If the deflections are continuous throughout markers, then the fabrics are likely a result of regional deformation (Paterson et al. 1998).

Secondly, structural and microstructural observations can be used to determine the rheological state during fabric formation and whether fabrics formed during suspension or grain supported flow (Paterson et al. 1998).

Third, it is essential to determine fabric ellipsoid shapes (strain, magnetic susceptibility, SPO, etc.) at multiple locations, and if possible within multiple markers (enclaves, feldspars, micas, etc.). Each marker will behave slightly differently, and combining fabric ellipsoid shape with kinematic data provides information about localized magma displacement paths (Paterson et al. 1998). These displacement paths can then be used to interpret magmatic fabrics (e.g., convection or magma surges) or strain fabrics. Magmatic fabrics have large displacement gradients in marker shapes, sizes, or orientations due to the nature of convection type flow patterns (Paterson et al. 1998). If fabrics resulted from regional strain, the marker displacement gradients should occur in both the pluton and the host rock (Paterson et al. 1998). If there is no clear magmatic fabric or strain fabric seen in the pluton, the use of magnetic mineral fabric orientations through Anisotropy of Magnetic Susceptibility (AMS) techniques can be employed to develop fabric ellipsoid shapes and orientations.

Determining the emplacement history of a pluton is difficult because the resultant fabrics are only a snapshot of the final stages of the pluton's history (Bouchez 1997, Paterson et al. 1998). However, these studies are worthwhile because of the wealth of information that can come from such a small snapshot of time. Combined with absolute age dating geochronology, one may be able to constrain dates for specific deformation activity such as fault movements, something that is not easily done unless the fault creates a new rock that has new minerals suitable for dating techniques (e.g. micas within a mylonite).

1.3 Moine Thrust Zone

One ideal location to study a number of intrusions that are related to deformation is the Moine Thrust Fault Zone, also termed the Assynt Culmination, in the Northwest Highlands of Scotland (Figure 1.3.1). The region is known for its beautifully exposed thrust faults, and syn-tectonic alkaline igneous intrusions. The igneous intrusions provide a wealth of information about the tectonic history of the region in the form of strain marker fabrics (Elliott & Johnson 1980, Halliday et al. 1986). The thrust faults within the Moine Thrust Zone developed mainly in-sequence from hinterland to foreland with the earliest thrust sheets riding passively on top of later thrust sheets in an in sequence "piggy-back" style (Elliott & Johnson 1980). The major thrust faults in the region, from structurally low (youngest) to high (oldest), are the Sole Thrust Fault, Glencoul Thrust Fault, Ben More Thrust Fault, and the Moine Thrust Fault (Figure 1.4.1 and 1.4.2; Elliott & Johnson 1980). All strike NE-SW and dip approximately 20° to the SE (Elliott & Johnson 1980).

Directly along the Moine Thrust Fault itself, rocks underwent intense mylonitization (Freeman 1998, Law 2010). The Moine Thrust plane is often the site of thick mylonites (meter scale) in both the footwall and hanging wall (Peach et al. 1907). The mylonites are often characterized by a strong foliation sub-parallel to the thrust plane, which dip gently (16-30°) to the ESE, and a weak grain shape stretching lineation plunging down dip within the foliation plane sub-parallel to the thrust transport direction (Law et al. 2010). Country rock proximal to the fault plane may display a very weak grain shape fabric (Law et al. 1986).

During the Ordovician-Silurian, the Iapetus Ocean was closing, and eventually sutured Laurentia to Baltica (Figure 1.4.3). This suture then started a convergent margin subducting oceanic crust below Laurentia (van Breemen & Bluck 1981, Oliver et al. 2008). The granitoid magmatism throughout Scotland is attributed to this new subduction zone on the western margin of Laurentia (van Breemen & Bluck 1981, Stephenson et al. 1999, and Oliver et al. 2008). A major pulse of magma occurred during the late Silurian and early Devonian caused from slab break-off (Neilson et al. 2009). The NW Highlands of Scotland are littered with plutons, dikes, and sills across the Moine Thrust Zone and throughout the foreland and hinterland (Peach et al 1907, Parsons 1999). The most voluminous of these intrusions occurred within the Assynt Culmination, including the Loch Ailsh Pluton (Parsons 1965) and the Loch Borralan Pluton (Woolley 1970, 1973), the focus of this study.

1.4 The Loch Borralan Pluton

In the southern part of the Assynt culmination two large alkaline intrusions, the Loch Ailsh and Borralan intrusions, have been mapped within the Moine Thrust Fault Zone. The Loch Borralan intrusion consists of an early suite of pyroxenites, nepheline syenites and syenites, and a later suite of feldspathic syenites and quartz syenites (Woolley 1970, 1973; Figure 1.4.1). U-Pb zircon ages of the Loch Borralan intrusion yielded crystallization ages between 430.6-425 Ma (Goodenough et al. 2011), coinciding favorably with the Scandian phase (435-425 Ma) of the Caledonian Orogeny (478±8 - 425 Ma; Oliver 2000, Strachan et al. 2002, Strachan & Thigpen 2007). Rb-Sr dating of synkinematically crystallized white micas in Moine mylonites along the Moine Thrust Fault plane constrained the age of ductile movement in the Moine Thrust Fault to be

between 437-408 Ma, with the majority of deformation ending around 430 Ma (Freeman et al. 1998). However, most studies found no clear observable indicators that the pluton experienced strain from tectonic movements during emplacement (Woolley 1970). The pluton is bounded on top by the Ben More Thrust Fault and by the recently proposed Borralan Thrust Fault below (Figure 1.4.2; Searle et al. 2010). Initially the pluton was thought to be post-tectonic due to lack of strong internal fabrics (Woolley 1970), but new U-Pb isotopic ages and structural field relationships suggest the latest suite of magma was emplaced syn-tectonically (Searle et al. 2010, Goodenough et al. 2011).

1.5 Research Questions

The primary aim of this project is to document the fabrics and microtextures within the recently dated Loch Borralan pluton in Northwest Scotland in order to constrain the relative timing of intrusion and motion along the neighboring Moine and Ben More thrust faults. AMS and shape preferred orientation (SPO) fabrics are used to determine if there is a relationship to regional thrust fault kinematics. Microstructures are evaluated to determine the deformation mechanisms and deformation conditions, specifically deformation temperature. Microstructures are analyzed to determine if deformation occurred when the pluton was magmatic, solid at hot temperature (crystal-plastic microstructures), or solid and cold (brittle microstructures). In particular, the study will address the following questions:

1. Do fabrics within the pluton correlate with strain patterns associated with thrust faulting?
2. If so, how far do deformation fabrics from the thrust fault propagate within the pluton?

3. Can we use deformation features within the pluton along with precise crystallization age to constrain absolute timing of motion along neighboring thrust faults?

This project was undertaken in conjunction with a detailed gravity survey conducted by Dr. Basil Tikoff from the University of Wisconsin-Madison. The microgravity survey will determine the shape of the pluton at depth, and determine where the pluton has intruded relative to the adjacent thrust faults.

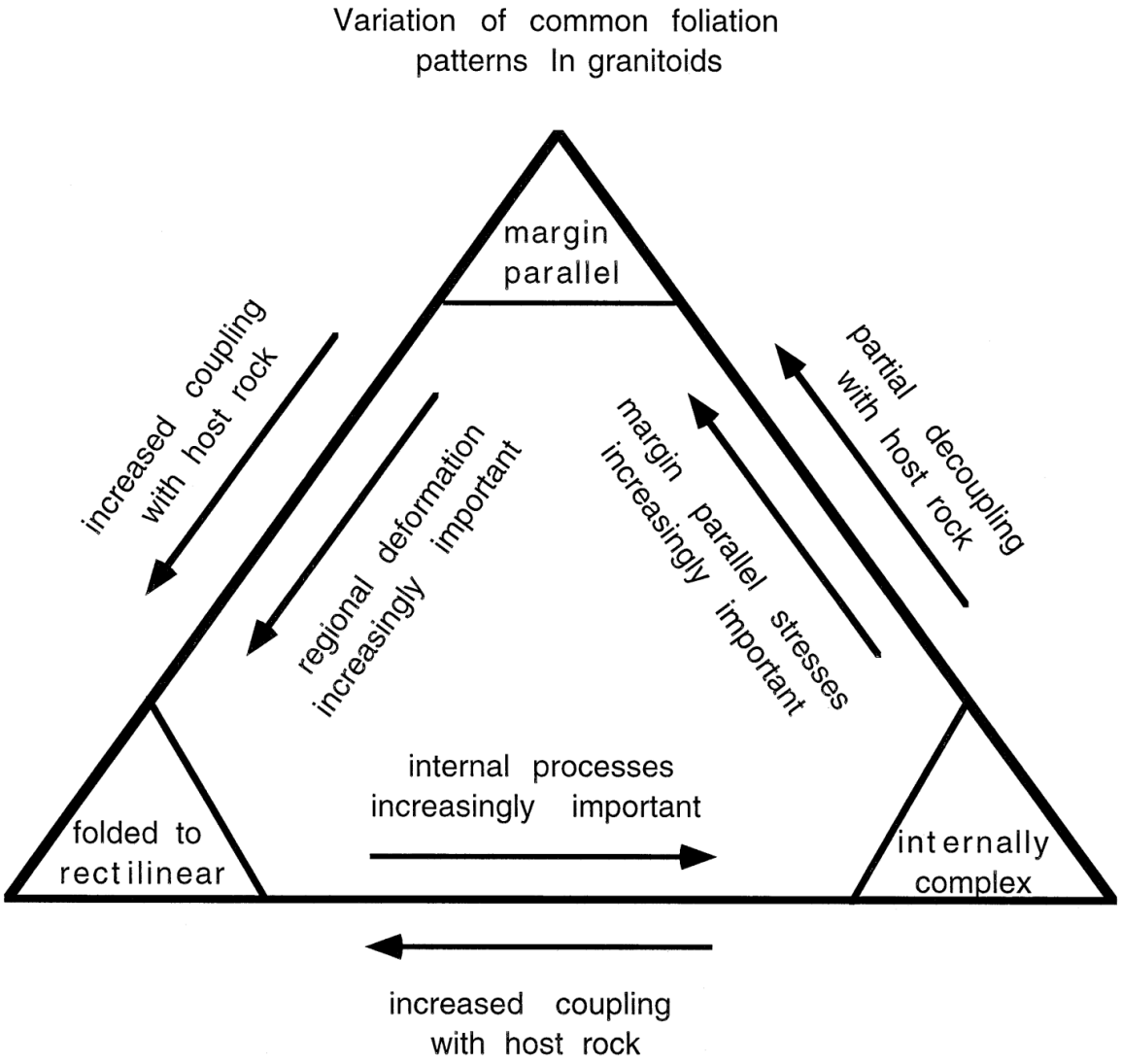

Figure 1.2.1: End-member types of magmatic fabric patterns in plutons. Margin parallel fabrics are the "onion-skin" type patterns where foliation strike is parallel to the pluton margins. These are typically seen in circular and elliptical plutons. Folded to rectilinear fabrics are fabrics that coincide with regional strain patterns in the country rock. Internally complex fabrics are typically found in elongated plutons (length to width ratio greater than 3). Elongated plutons tend to have more complex geometries with lobes and flow gradients. Magmatic structures of internally complex plutons will cut across igneous contacts, and occasionally across host rock contacts. These fabrics can also result from a combination of both regional strain and complex magmatic patterns. Many plutons have components are a combination of multiple pattern types (Paterson et al. 1998).

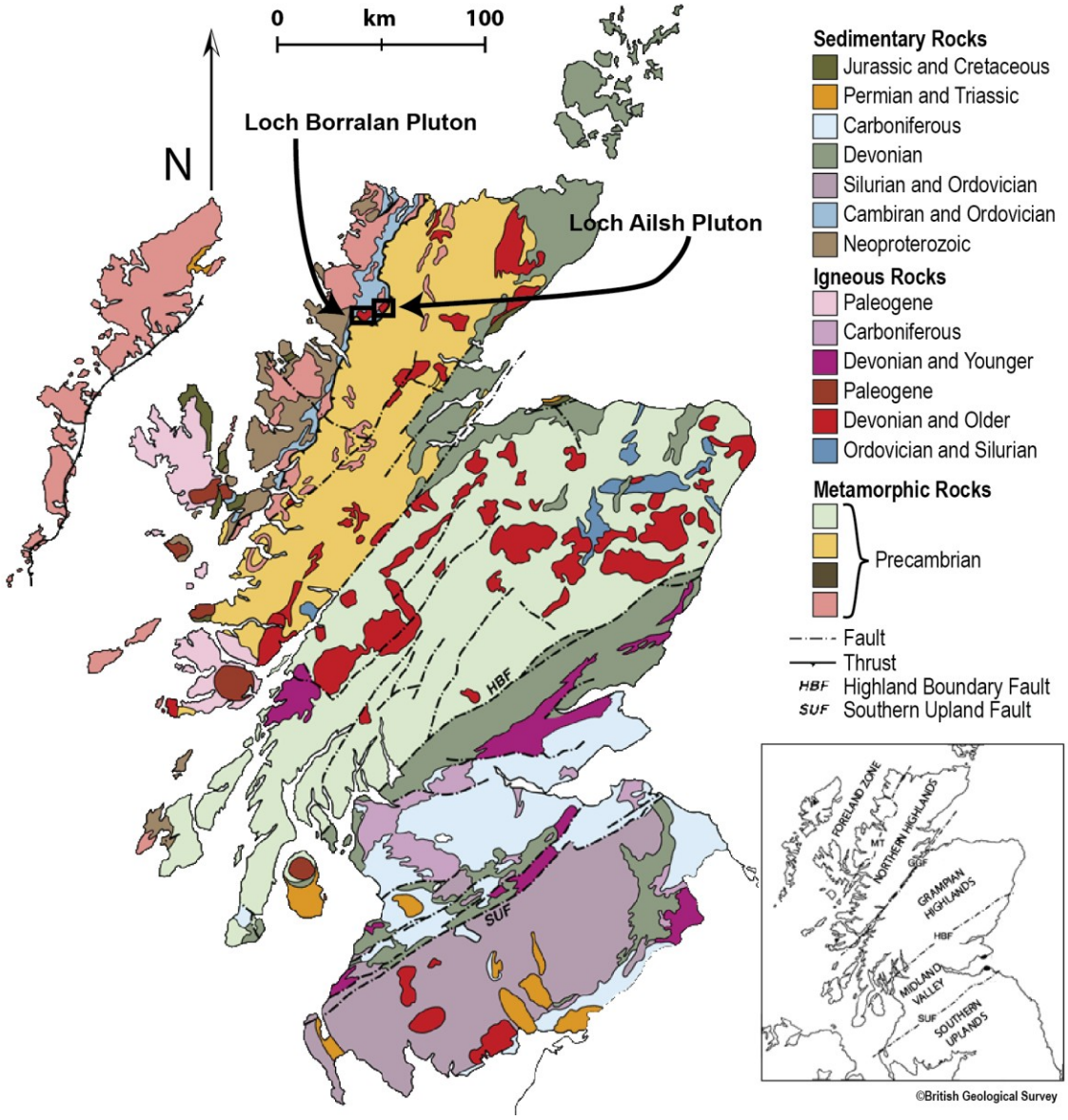

Figure 1.3.1: Simplified geologic map of Scotland showing the study area within the black box. The inset map shows the 5 geologic terrains of Scotland. Modified from the British Geological Survey.

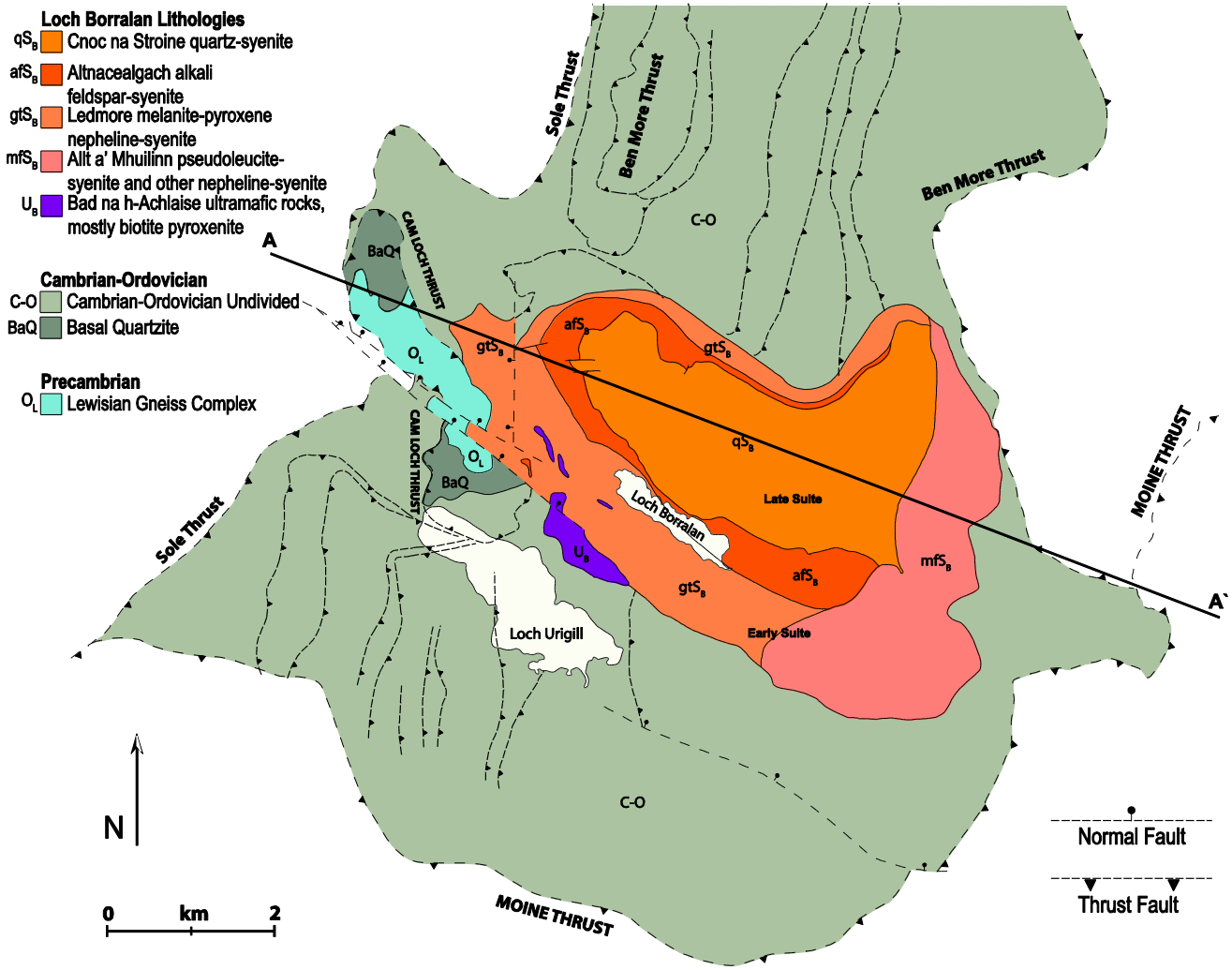

Figure 1.4.1: Structural overview of the Loch Borralan Pluton and the surrounding rock units and many neighboring thrust faults (Modified from Woolley 1965). Approximate cross-section line A-A' depicted on Figure 1.4.2.

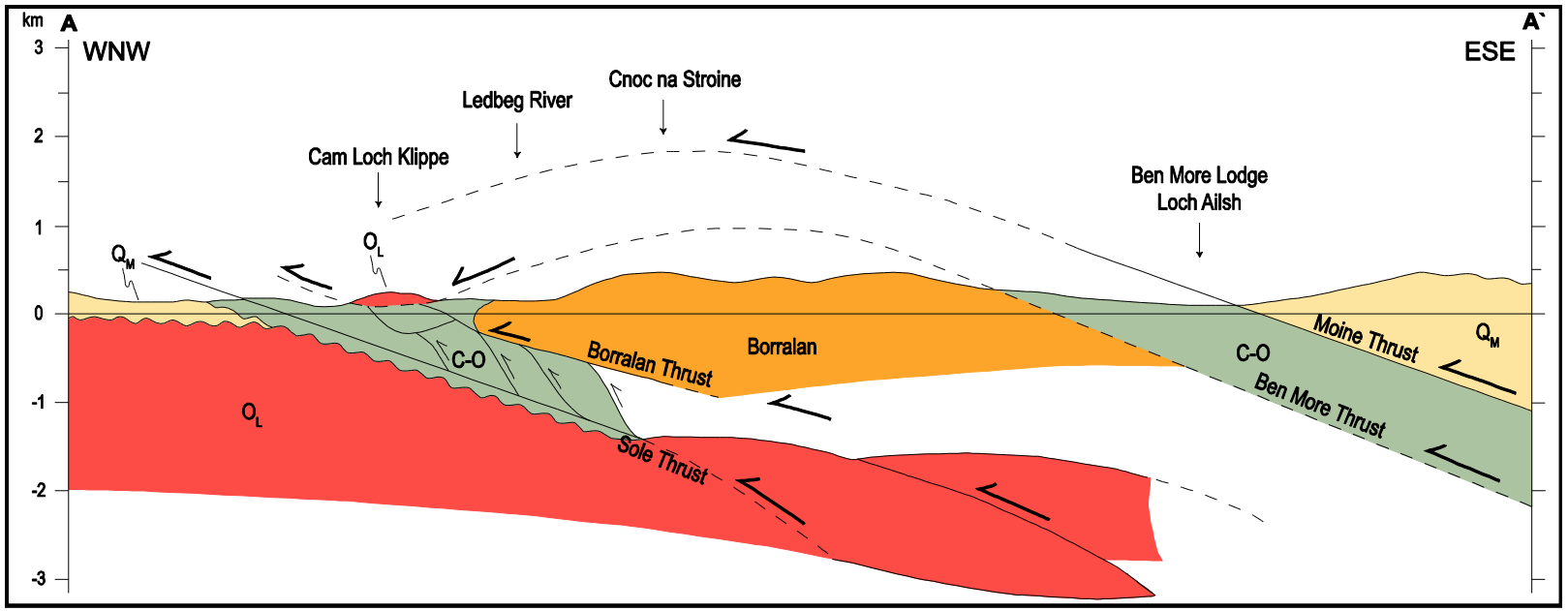

Figure 1.4.2: Cross section by Searle et al. (2010) showing the newly proposed "Borralan Thrust" at the base of the Loch Borralan Pluton. Cross-section location depicted on map, Figure 1.4.1.

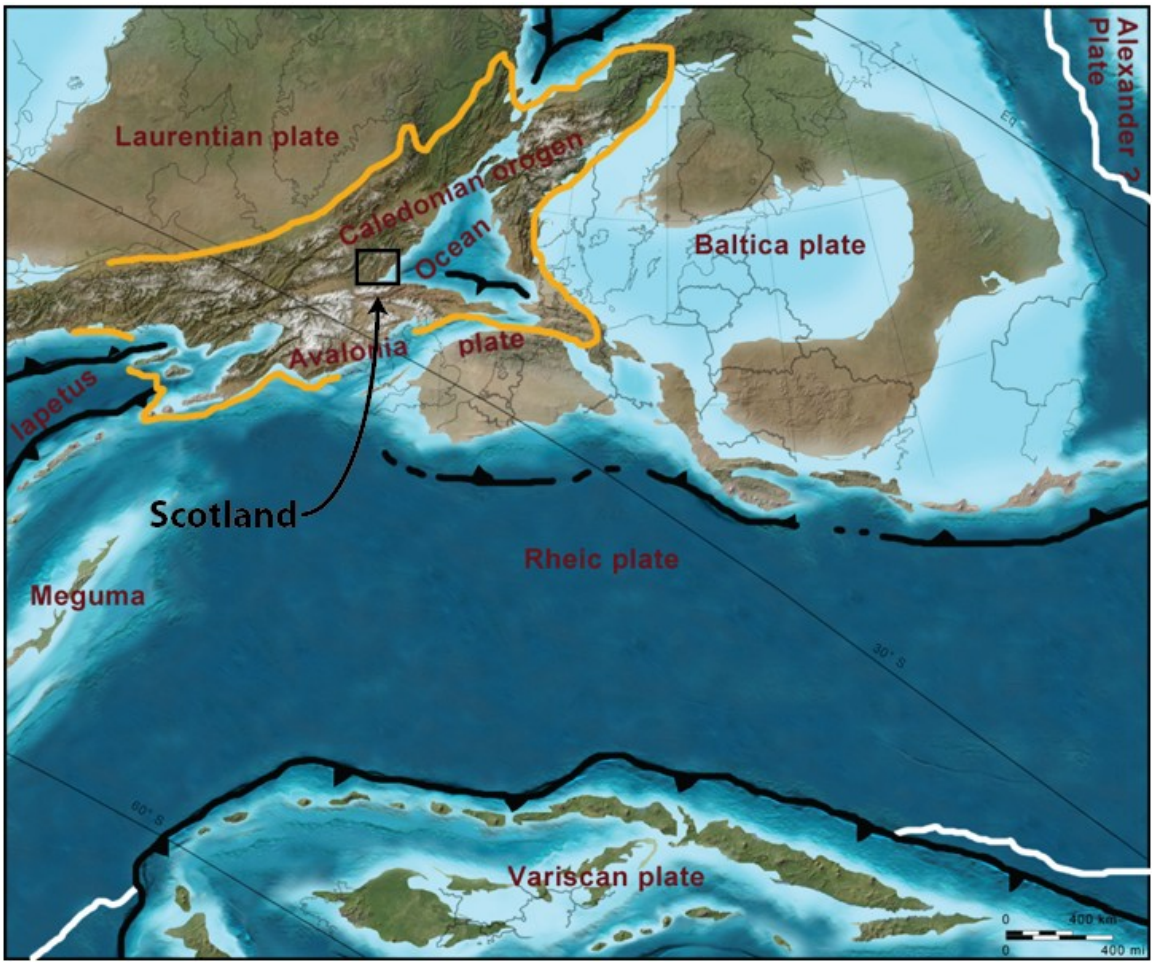

Figure 1.4.3: Paleogeographic reconstruction (Blakey 2010) showing the closure of the Iapetus Ocean, and the formation of the Scottish Highlands and Appalachian Mountains resulting from the collision of Baltica and Laurentia.

2. Background

2.1 Regional Geology

The Northwest Highlands of Scotland were shaped by the Caledonian orogenic belt, which extends from Svalbard, through Scandinavia, East Greenland and the British Isles, to the Appalachian Mountains of North America (Figure 1.4.3). The Caledonian orogeny occurred between 480-425 Ma in two stages, the Grampian event (480-465 Ma) and the Scandian event (435-425 Ma; Strachan *et al.* 2002; Strachan & Thigpen 2007). The result was a collision between paleo-continents Baltica and Laurentia, along with the closure of the Iapetus Ocean (Figure 1.4.3). One of the major thrust faults active during the Caledonian orogeny, the Moine Thrust Fault in northwest Scotland, has been of fundamental importance in the interpretation of thrust fault geometries, and the sequence and timing of thrusting since the initial mapping of Peach and Horne (1884, 1914) and Peach et al. (1888, 1891, 1907).

The Moine Thrust Fault zone forms the northwestern margin of the Caledonian orogeny in Scotland. The foreland, west of the Moine Thrust Fault, is comprised of Archean to Palaeoproterozoic Lewisian Gneiss basement (tonalitic, trondhjemitic, mafic and ultramafic gneisses intruded by granodiorites and granites) and is unconformably overlain by Meso- to Neoproterozoic clastic sedimentary rocks belonging to the Stoer, Sleat and Torridon Groups. These three groups are sometimes combined under the term Torridonian. Cambrian-Ordovician shallow marine sedimentary rocks unconformably overlie both Lewisian and Torridonian Group rocks (Peach et al. 1907, Park et al. 2002).

East of the Moine Thrust Fault lie the metasedimentary rocks of the Early Neoproterozoic Moine Supergroup in the North Highlands (Figure 1.3.1; Strachan et al. 2002).

2.2 Previous Work

The initial geologic investigations in the Scottish Highlands were started by the British Geological Survey, and focused on creating geologic maps of the region. Workers such as John Macculloch (1836), Robert Hay Cunningham (1841), and James Nicol (1844) mapped the simpler geology to the north of the Assynt Window where rocks are flat lying and in stratigraphic order, but it wasn't until Roderick Impey Murchinson was appointed Director of the Geological Survey did work begin on the complex structurally deformed parts of the Northern Highlands. Murchinson and Nicol's original interpretations of the region stated that the rocks abided by simple stratigraphic rules similar to the rocks found north of the Highlands. They failed to adequately explain the cause for field relationships such as Proterozoic gneiss lying stratigraphically above Ordovician sandstones and limestones. Murchinson and Nicol's interpretations were the cause for much debate in the early 1880's about the controversial field relationships seen in the NW Scottish Highlands. The debate started a research effort by the Geological Survey of Great Britain to investigate these "tectonic contacts that repeated rock section" (Callaway 1883; Lapworth 1883). Lapworth later went on to describe what Murchinson & Geikie (1861) called bedding in the metamorphic rocks to actually be a tectonic foliation which he termed 'mylonite' (Lapworth 1885). The then Director General of the Geological Survey, Archibald Geikie, sent two of his most experienced geologists Ben Peach and John Horne to disprove Lapworth. Rather than disproving Lapworth, however, Peach and Horne confirmed his findings, and Geikie recanted his previous work and

coined the term ‘thrust’ in his Geikie (1884) paper taking credit for the re-interpretation. Lapworth, Callaway, Geikie, Peach, and Horne continued to map and study the NW Highlands using their new approach of combining petrological and paleontological data to the stratigraphic relationships. The work was summarized and compiled by Peach and Horne into the detailed 1907 memoir. The work became influential to structural geologists because it depicted some of the first documented accounts of thrust fault structure and thrust processes.

It wasn’t until the advancement of structural geologic theories and models did work get rekindled in the region. A.R. Woolley was a prominent researcher of the structure and petrology of the Highlands and published work specifically on the alkaline intrusions of the region including the Loch Borralan Pluton (Woolley 1965, 1970, 1973). His main goal was to unravel the timing and structural relationships between the intrusions and the thrust faults. Woolley also defined the initial rock types comprising the Loch Borralan Pluton. Woolley (1970) separated the Loch Borralan pluton first in-to two suites of magmas. The early suite is comprised of three rock types, the Ledmore, Pseudoleucite, and Nepheline syenite types. The late suite is simply one type of syenite grading to quartz syenites. Woolley’s structural history and timing suggested deformation had virtually stopped before the late suite syenites were emplaced. However, Woolley mentions some movements had to have taken place after both suites were emplaced and solidified (Woolley 1973).

More recently with the advent of precise U-Pb isotopic age dating, the ages of most of the rocks in the region have been absolutely dated allowing for much better interpretations about the tectonic history of the Scottish Highlands. Searle et al. (2010)

published the first combined geochronologic and structural interpretation of the Loch Borralan and Loch Ailsh Plutons (Figure 1.3.1). Searle et al. (2010) concluded that the Loch Ailsh and Borralan plutons were intruded simultaneously at about c. 430 Ma prior to thrusting along the Moine and Ben More Thrusts. The Loch Borralan intrusion likely is underlain by a thrust, the Borralan Thrust (Searle et al 2010). The Borralan thrust does not outcrop anywhere, but was proposed because the intrusion sits above a set of imbricate duplexes associated with the stratigraphically lowest thrust, the Sole Thrust. Interpretations about the nature of the Loch Borralan pluton's contacts are non-existent due to exposure being almost entirely covered by peat bogs. Only one very poor contact is exposed on the eastern side of the pluton showing an intrusive contact between the early suite and the Cambrian-Ordovician quartz arenite country rock (Woolley 1970).

Searle's work on the Loch Borralan Pluton was based on U-Pb dates done by van Breemen et al. (1979). Goodenough et al. (2011) revised van Breeman (1979) U-Pb ages with more accurate techniques, but the interpretations did not change much about the plutonic activity from the ideas in Searle et al. (2010). Goodenough et al. (2011) new U-Pb ages updated van Breemen et al. (1979) date of 430 ± 4 Ma for the Loch Borralan Pluton to 431.1 ± 1.2 Ma for the early suite, and 429.2 ± 0.5 Ma for the late suite. The Loch Ailsh Pluton was dated to 430.6 ± 0.2 Ma (Goodenough et al. 2011). With these new U-Pb dates and observable tectonic deformation fabrics seen in the Loch Borralan early suite, Goodenough et al. (2011) confirmed that final motion along the Moine and Ben More Thrusts occurred after 430 Ma, and that motion along some thrusts likely occurred while both Loch Ailsh and Borralan Plutons were hot or cooling (Searle et al 2010). Flattened pseudoleucites in the early suite of the Loch Borralan Pluton display

foliation and stretching lineations showing that high-temperature fabrics were formed after crystallization, but while the pluton was still at a high temperature (c. 500-550 °C, Searle et al. 2010).

2.3 Similar Studies

Many workers have used AMS analysis of magnetic fabrics in their research to study emplacement and deformation characteristics of plutonic rocks. Particularly relevant is the work of Bouchez et al. (1990), Launeau and Cruden (1998), Cruden et al. (1999), Aranguren et al. (2003), Czeck et al. (2006), Maes et al. (2007), and Archanjo et al. (2011). These studies all use a combination of AMS derived mineral orientations combined with petrographic analysis. AMS measurements generally parallel mineral lineations and foliations. This is very useful for plutons that have localized or weak fabrics, and AMS can be used to fill in gaps where field measurements were not obvious or present. Microstructural analysis determines which deformation mechanisms, if any, are present. Deformation mechanisms have specific temperature and pressure conditions where they occur, and can give insight into the relative timing of emplacement and deformation (e.g. hot and ductile vs. cool and brittle).

Launeau and Cruden (1998) used AMS and SPO analyses in the Lebel Stock, a syenite intrusion in Ontario, CA, with a similar mineralogic composition to the Loch Borralan pluton to determine the petrographic significance of the magnetic fabrics, and compare petrofabrics of silicate and magnetic minerals in both deformed and undeformed syenites from the same magma. The study heavily employed SPO measurements in their interpretations using a technique developed by Launeau and Robin (1996), called

intercept method of image analysis. Thin sections were prepared for each sampling locality and were cut along three mutually perpendicular AMS derived faces (K_1>K_3, K_1>K_2, and K_2>K_3). Images of the thin section are then collected and K-feldspar, clinopyroxene, and biotite + magnetite were classified in the images using threshold filters. Using the program INTERCEPT.EXE by Launeau & Robin (1996) mean mineral lengths and mineral boundary intercept directions of the 3 mineral classes were measured plotted as ellipses for easy comparison. Launeau & Cruden (1998) found that the long axes of all three mineral classes were parallel.

Czeck et al. (2006) investigated the Algoman suite of granites and granodiorites within the Rainy Lake region of the Superior Province. They used a combination of AMS, SPO, and petrographic analysis to determine the relationship between pluton fabrics and regional kinematics. Similar to initial accounts of the Loch Borralan pluton, the rock suite's apparent lack of structures was originally thought to constrain the end of deformation in the region. However, magnetic foliations coincided well with regional deformation foliations within neighboring rocks, as well as the macroscopic foliations within the rock suites where present. Limited crystal-plastic quartz microstructures were also found within the plutons, further supporting the argument that these plutons were syn-tectonic rather than post-tectonic.

Maes et al. (2007) encountered an interesting problem within the Sonju Lake layered intrusion, northeast Minnesota, where a small population of sample localities displayed a 90° offset between field and AMS foliation/lineation measurements. Of the 32 sites sampled in the area 26 had normal magnetic fabrics, while 6 displayed the offset fabrics. Maes et al. (2007) also used the INTERCEPT.EXE by Launeau & Robin (1996)

along 3 perpendicular AMS faces. Thin section images were taken, and plagioclase and magnetite were isolated using image threshold filters. Mean mineral lengths of plagioclase and magnetite were measured separately and plotted similarly to the Launeau and Cruden (1998). The SPO measurements showed that the plagioclase was within a reasonable orientation of the magnetic lineation, ranging between 6-30° offset. However, there was a significant offset between the opaque and plagioclase petrofabrics. The plagioclase SPO mean length showed a crystallographic arrangement that was ~90° different than the magnetite mean lengths. Thus, AMS orientations are controlled by the pseudo-single-domain (PSD) and multi-domain (MD) magnetite that is crystallographically accommodating the orientations of the silicates (ie plagioclase).

3. Methods

3.1 Fieldwork

One hundred fourteen oriented samples of the Loch Borralan pluton have been collected covering the entirety of the late magma suite, but only a portion of the southeastern extent of the early suite (Figure 3.1.1). Due to poor exposure of the early magma suite, very few samples could be obtained. Sample stations were selected based on available exposure. A previous team consisting of Bryn Benford and Kelly Hoehn from the University of Wisconsin-Madison collected 12 of the 114 samples in 2008. A second team consisting of myself, Dr. Dyanna Czeck (UW-Milwaukee), Dr. Basil Tikoff (UW-Madison), Dr. Vasileios Chatzaras (University of Patras), and undergraduate Jack Graham, collected oriented samples, mineral fabric data, and microgravity measurements from May to June 2012. For this study, the mineral fabric data and oriented samples are utilized. The microgravity is being studied by other members of the research group.

Mineral foliations and lineations of aligned alkali feldspar crystals were measured using a Brunton compass at sample locations where present, and occasionally measured where sampling was not possible (Figure 3.1.2A and 3.1.2B). For outcrops that contained multiple foliation orientations, only the most dominant fabric was measured. Other structural features such as shear zones and faults were noted and measured where observed.

3.2 Anisotropy of Magnetic Susceptibility (AMS) and Identification of Magnetic Mineralogy

AMS has proved to be a useful tool in characterizing planar and linear fabrics in rocks where microstructural and field observations are insufficient (e.g. Borradaile 1988; Bouchez et al. 1990; Borradaile and Henry 1997). AMS is a tool that when combined with field measurements, petrographic analyses, magnetic mineralogy analyses, and/or geochronologic techniques can be used to relate pluton fabrics to regional strain orientations. AMS data can be represented as a second rank tensor, or geometrically as an ellipsoid (Jelinek 1981), making AMS analysis ideal for strain analysis. The principal axes of the magnetic anisotropy ellipsoid ($K_1 \geq K_2 \geq K_3$) often correlate to the principal axes of the finite strain ellipsoid (Borradaile 1988; Borradaile and Henry 1997), and have been often used as a proxy for strain measurements in granitoid rocks (e.g. Bouchez et al. 1990; Launeau and Cruden 1998; Cruden et al. 1999; Aranguren et al. 2003; Czeck et al. 2006).

At least two samples were collected from each station when possible, and two cores were drilled from each rock when possible. This sampling density allows statistical comparison of the AMS ellipsoids within and between samples. Forty-four samples were drilled for standard one inch cores, totaling 69 cores analyzed.

The AMS measurements were conducted at the University of Wisconsin-Milwaukee using the AGICO MFKA-1 Kappabridge. The Kappabridge creates a known and stable magnetic field in a contained environment. When a magnetizable sample is introduced to the induced field, the machine records the orientation and magnitude of the

field's offset which can be orientation dependent. Specimen cores are measured in three orientations in a continuously rotating sample holder that very accurately calculates the magnitudes and orientations of the principal susceptibility axes ($K_1 \geq K_2 \geq K_3$) as well as the bulk susceptibility of the specimen. The combination of these axes forms the AMS ellipsoid. The Kappabridge also supplies scalar AMS parameters, including K_m, P_j, and T that are the most important to this study. K_m is the bulk mean susceptibility value with contributions from all the minerals in the rock. P_j is the degree of anisotropy of the AMS ellipsoid. T_j is the anisotropy ellipsoid shape parameter ($T>0$ is oblate, $T<0$ is prolate).

In order to interpret the AMS measurements, understanding the mineralogy that causes the magnetic field is required.

To characterize the magnetic mineralogy, the vibrating sample magnetometer (VSM) at the Institute of Rock Magnetism (IRM) at the University of Minnesota was used. The VSM provided hysteresis loops for 40 representative samples throughout the Loch Borralan pluton (Appendix A). Hysteresis data are acquired by measuring the magnetization (M) of a vibrating sample within an alternating field. The rock is initially demagnetized at the maximum magnetic field (H) of 1 Tesla (T). The magnetic field is then gradually reduced to 0T, and then gradually shifted in the opposite direction to 1T. Magnetization is measured simultaneously with the field shift. H and M are then plotted to form the hysteresis loop. When the two parts of the loop are offset (typically are), the difference between the two is the remanence. The hysteresis data were used to measure the saturation magnetization (Ms), remanent saturation (Mr), and magnetic coercivity (Hc). These measurements allowed determination of the magnetic mineralogy in each sample, the contribution of magnetism types (dia-, para-, or ferromagnetic) and which

mineral(s) causes the magnetic fabric. By also measuring the coercivity of magnetic remanence (Hcr), the effective grain size of magnetite can be determined. The characterization of magnetic mineralogy is necessary to properly interpret the AMS fabrics, since the correlation between shape fabric and magnetic fabric differs by mineral type (Bouchez 1997). Petrographic studies were also conducted to further support the magnetic fabric AMS orientations.

3.3 Qualitative Petrographic Analysis

Ten thin sections from 5 field stations were used in this microstructural analysis (Figure 3.1.1). Stations were selected to most accurately represent the geographic extent, different lithologies, and structures present within the Loch Borralan pluton. Each station chosen for analysis had 2 thin sections cut with respect to the orientations of the principal magnetic susceptibilities. One cut was made parallel to lineation and perpendicular to foliation ($K_1 \geq K_3$), and another perpendicular to both lineation and foliation ($K_2 \geq K_3$). In one case (LB12-40B), I did not have any AMS data for that exact location to use for the cut orientations, so I used the nearest station with AMS results (LB08-06) to approximate foliation and lineation orientations. At least two separate cuts are necessary to get the most accurate representation of all types of microstructures present.

Microstructures were analyzed to determine if deformation occurred when the pluton was magmatic, solid at hot temperature (crystal-plastic microstructures), or solid and cold (brittle microstructures). Examples of magmatic textures include parallel or subparallel alignment of elongate euhedral crystals, imbrication of elongate euhedral crystals that are not internally deformed, elongation of enclaves without plastic

deformation, flow lines/foliations, and layering. Examples of deformation microstructures include fractures, selvage seams, twinning (mechanical), deformation lamellae, undulose extinction, sub-grains, and grain boundary bulges. Each of these microstructures is indicative of a particular microscopic deformation process: diffusive mass transport (DMT), dislocation creep, or cataclasis. The microstructural analysis is qualitative with the purpose of noting the types of microstructures present and interpreting the likely deformation mechanisms.

Brittle microstructures such as cataclastic texture, microveins, and microfractures commonly occur in the upper crust (Vernon 2004). Brittle microstructures are most often seen in the first 10-15km of continental crust, termed the frictional flow regime (Stewart et al. 2000). Brittle deformation is also associated with low temperatures (0-300 ± 50ºC; Sibson 1982). Exact temperatures and pressures associated with brittle deformation are dependent on rock properties including mineralogy, grain size, and water content.

Crystal plastic microstructures occur in mid crustal levels beyond 10-15 km, called the frictional-viscous transition zone (Stewart et al. 2000), and temperatures of about 300 ± 50ºC (Sibson 1982). Crystal plastic microstructures form through a process called dislocation creep, where deformation is attained through the movement of dislocations through the crystal lattice (Vernon 2004). Dislocations are linear crystal defects that form during crystallization or subsequently when stress is applied to a mineral. Examples of microstructures forming during dislocation creep are mechanical twinning, sub-grain formation, undulose extinction, and bulged grain boundaries (Vernon 2004). Dislocations can ‘tangle’ and interfere with each other hindering their propagation. Recovery and recrystallization processes reduce the concentration and/or

tangling of dislocations, allowing deformation to continue. Examples of typical recovery process microstructures are evenly spaced sub-grain boundaries, and aggregates of newly recrystallized strain-free grains (Vernon 2004).

Diffusive mass transfer (DMT) occurs when fluids aid in dissolving and reprecipitating minerals (Vernon 2004). Because DMT is so greatly dependent on fluids, it may occur in all levels of the crust, but is most abundant in low-grade metamorphic rocks (Vernon 2004). Examples of microstructural evidence for DMT include remnant zones of insoluble material called selvage seams and shadows around rigid grains (Vernon 2004). Veins may also form with fluid flow through rocks, but generally require a combination of brittle fracturing and precipitation of minerals from fluids (Passchier and Trouw 2005).

Mineralogy, grain size, composition of the intergranular fluid, lattice-preferred orientation, porosity, and permeability are all internal controls on deformation type (Passchier and Trouw 2005). Examples of external controls are temperature, lithostatic pressure, differential stress, fluid pressure, and strain rate. Generally, temperature (metamorphic grade) is the greatest controlling factor on the types of deformation microstructures (Passchier and Trouw 2005), but the presence of fluids greatly influences deformation as well. Deformation in quartz, for example, is highly dependent on the presence of water in the crystal lattice (Passchier and Trouw 2005). Even at low-grade conditions (<400°C), quartz can display dislocation creep microstructures with high water pressure in pore spaces (Passchier and Trouw 2005). Crystal-plastic deformation in feldspars generally occurs at relatively high temperatures (Passchier and Trouw 2005). Quartz has the potential to begin to deform crystal plastically at temperatures below

400°C, but feldspars commonly will not display this type of deformation until a temperature of around 450-600°C is reached. Brittle deformation is favored in low temperatures, high stress, or high strain rates (Passchier and Trouw 2005). Crystal plastic deformation structures are typically found in high temperature, high pressure, and low strain rate sites (Passchier and Trouw 2005).

3.4 Shape Preferred Orientation (SPO)

As an independent test to check the origin of the magmatic fabric, shape-preferred orientations (SPO) analysis will be conducted. The SPO analysis was conducted on all 10 thin sections separately for alkali feldspar grains and opaque minerals. While there is no generally accepted number of grains needed for a properly representative SPO analysis, ideally hundreds to thousands of grains would be used, depending on fabric strength. On the high end of analyzed grains, Hastie et al. (2010) measured the SPO of 2,500-3,500 plagioclase grains per thin section. Lower end studies (e.g. Izquierdo-Llavall et al. 2012) analyzed 478 biotite preferred orientations in one thin section. Generally, SPO analysis for Loch Borralan thin sections in the early suite included <30 feldspar grains, and <20 opaque minerals. In the late suite, a typical thin section consisted of approximately 100-500 feldspar grains, and 20-100 opaque grains. The number of grains included in the SPO analysis was dictated by the grain size and size of the thin sections.

While there are many ways of conducting an SPO analysis, SPO was measured here using the intercept method of image analysis (Launeau and Robin 1996), which has been used in many studies with success (Maes et al. 2007, Hastie et al. 2011, Archanjo et al. 2012, and Izquierdo-Llavall et al. 2012). The intercept method counts the number of

intercepted segments of a set of mineral grains on the image by a set of parallel scan lines along 180° directions across a digital photograph of a thin section (Figure 3.4.1). Because we see some discrepancies between the orientations of the magnetic and macroscopic mineral foliations, the SPO of the feldspar minerals forming the macroscopic foliation, and the magnetic fabric minerals (magnetite) were measured. Digital image processing threshold filters were used on the thin section images to contrast the alkali feldspars from the magnetic minerals. The program INTERCEPT.EXE by Launeau and Robin (1996; available on the internet) was used to automate the counting and measuring of the mineral orientations. Once the mineral boundary intercepts are counted, the INTERCEPT.EXE program outputs intercept direction, mean length, boundary direction, and inertia tensor ellipse and rose diagrams. In this project, the mean length ellipse is most useful to determine the fabric orientations because it represents the mean orientation of the long axis of the mineral. The intercept and boundary direction ellipses show the direction of boundary intercepts which can be skewed with complex grain shapes, see (Figure 3.4.2).

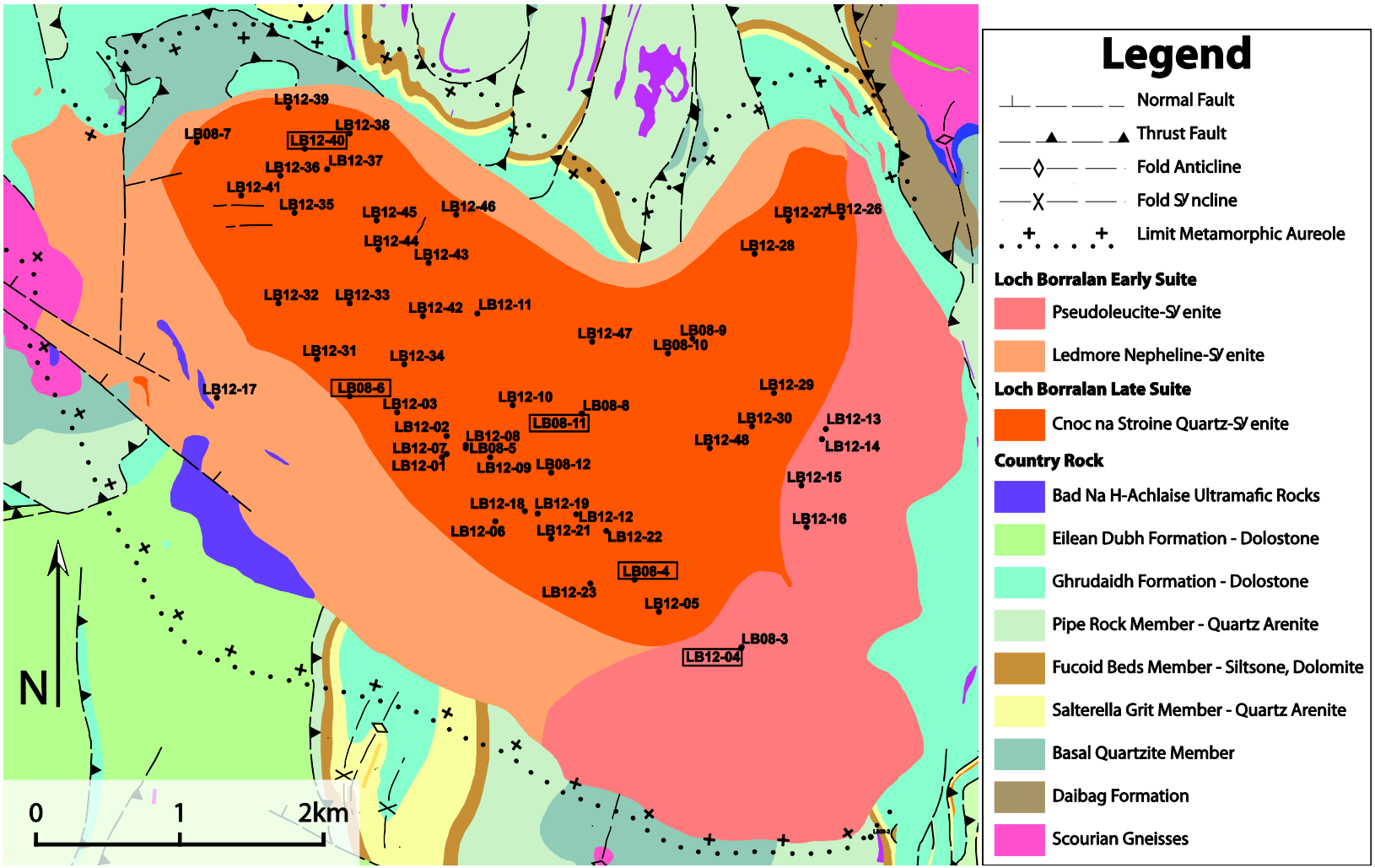

Figure 3.1.1: Location map showing Loch Borralan and the field station locations throughout the pluton. Station locations with box represent sites where thin sections were made and analyzed. Modified from British Geological Survey (2013).

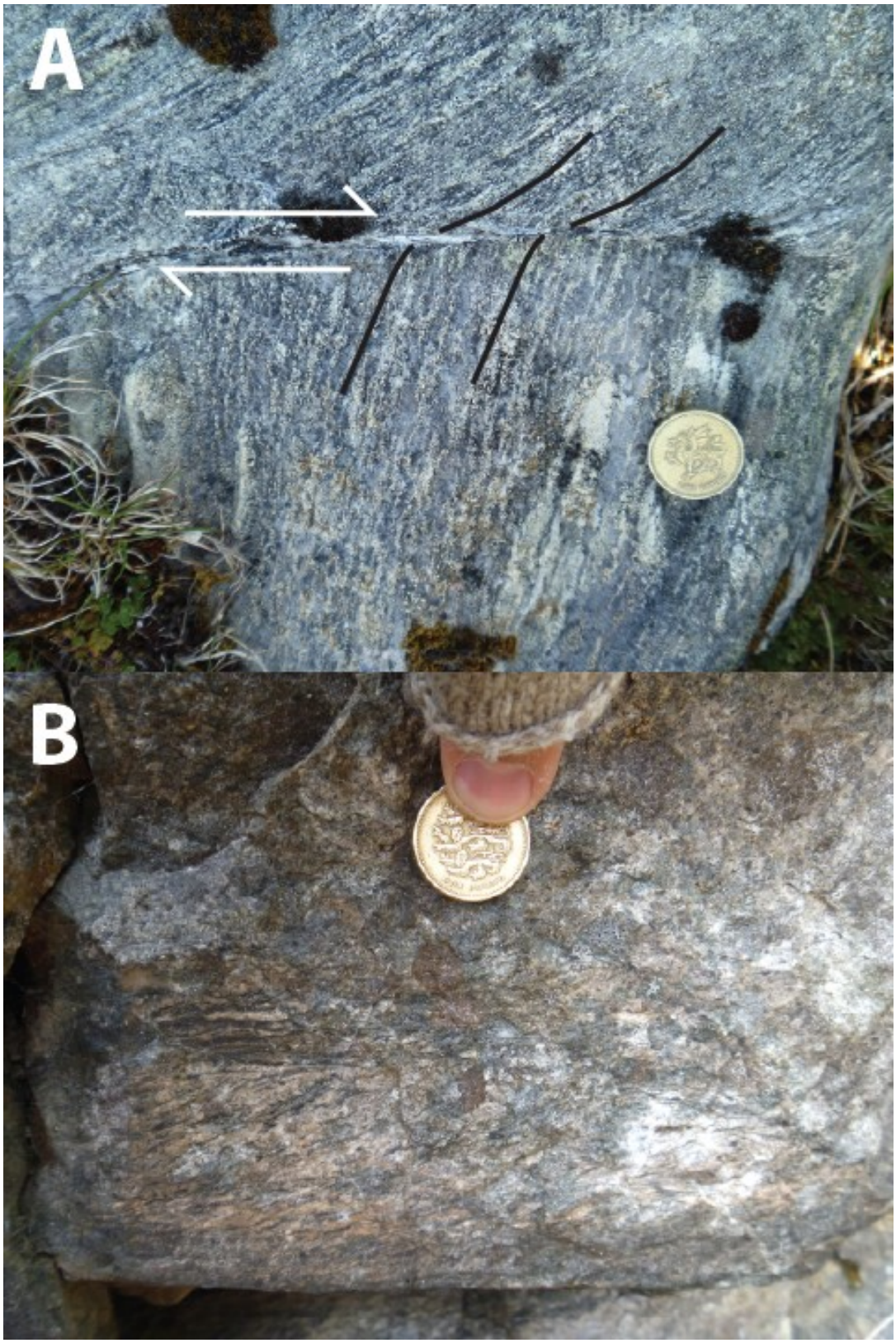

Figure 3.1.2: (A) Photos of well developed and (B) poorly developed fabrics in the field. Photo A also features a thin shear zone with clear shear sense indicating dextral shear.

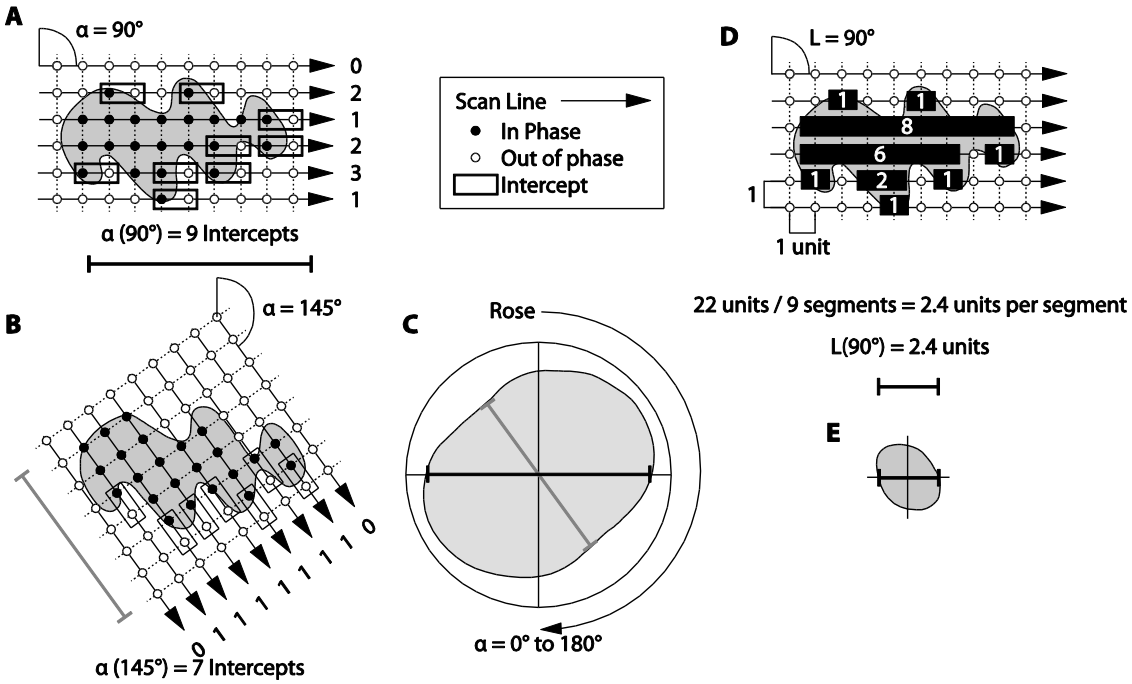

Figure 3.4.1: Processes behind the INTERCEPT.EXE Program by Launeau & Robin (1996). To create the intercept ellipse (C), the grain was scanned with parallel paths at 180° increments. Two angle scan paths are theoretically represented in (A) and (B). For the mean length calculations (D) the same 180° paths are used, but rather than counting boundary intercepts the program counts the length, in user defined units, the scan path takes through a grain. The length measurements of the grain are then averaged over the total path taken, and then finally a mean length ellipse (E) is calculated.

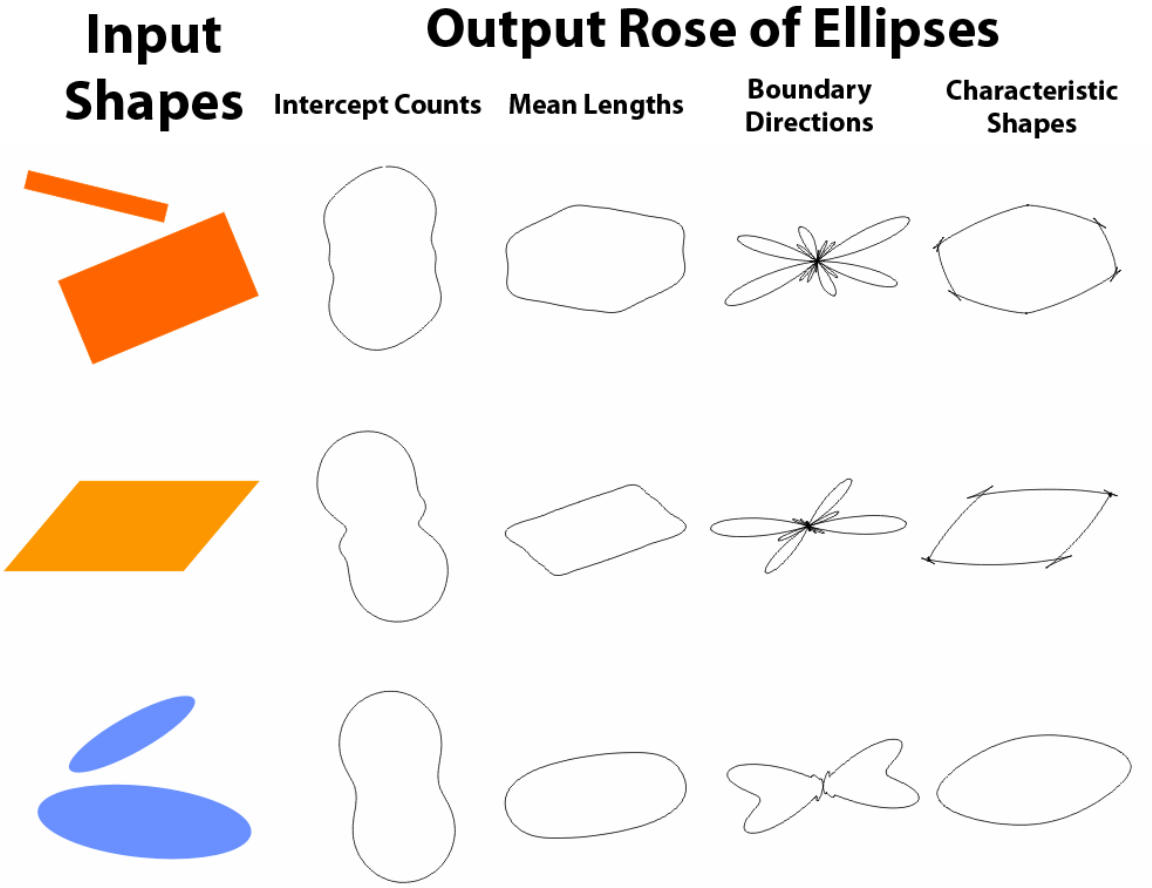

Figure 3.4.2: Calculated Fourier series rose of ellipses calculated from simple input shapes using the INTERCEPT.EXE program (Launeau & Robin 1996). Intercept counts rose of ellipse long axis point towards the direction in which the most grain boundary intercepts were encountered. The mean length rose of ellipse long axis parallels the averaged grain shape long axis orientation. Similar to the mean length rose of ellipse the boundary direction rose of ellipse, points towards the grain shape's long axis, but does not average the measurements. Characteristic shape is calculated to represent the average shape and orientation of the measured grains. This characteristic shape is used in the final SPO analysis.

4. Results

4.1 Field Data and Observations

Macroscopic foliations and lineations of alkali feldspars were measured throughout the Loch Borralan Pluton at 48 field stations (Figure 3.1.1). In total there were 118 foliations, 24 lineations, 31 shear zone planes, 18 fault planes, and 1 fold measured (Figure 4.1.1-4.1.2; Table 4.1).

Due to the poor exposure of the early suite, the majority of the measurements were taken from the late suite.

Foliations and lineations were formed by an ordered alignment of alkali feldspar minerals. Foliations are strongly developed throughout the entirety of the pluton, whereas lineations are generally more scarce and poorly developed (S>L fabrics). In the Aultivullin quarry (station LB12-04, Figure 3.1.1) on the SE margin of the pluton, an exposure of early suite displays stretched pseudoleucite aggregates that were measured by Searle et al. (2010).

The measured foliations dominantly strike NE-SW, which parallels the adjacent thrust faults (Figure 4.1.4). The early suite foliations strike approximately 030 and dip 20° SE (Figure 4.1.2). Foliations in the late suite have a similar strike orientation to the early suite, but dip roughly 50-65° to the SE and NW (Figure 4.1.2). The strike of foliations in both late and early suites is subparallel to the regional thrust faults (Sole, Ben More, Glencoul, and Moine Thrusts). The foliation dip within the early suite is subparallel to the regional thrust faults. The foliation dip within the late suite is

subparallel to the imbricate thrust faults mapped in adjacent Cambrian-Ordovician quartz arenite.

The late suite lineations generally plunge shallowly towards the NE in a direction parallel to the strike of the thrust faults (Figure 4.1.2 and 4.1.3). Only two lineations were confidently measured within the early suite making interpretations difficult.

Brittle faults were observed in outcrop within the late suite, and ductile shear zones were observed throughout the entire extent of the pluton (Figure 4.1.2). The SE, NW, and west central portions of the late suite have dominantly ductile shear zones, while the central and NW portion of the pluton have small (1-30cm offset) brittle faults. Both the shear zones and fault planes are sub-parallel to the NE-SW strike of the macroscopic mineral foliation (Figure 4.1.2).

Eighteen brittle faults were measured in the late suite. All brittle faults had a NE-SW strike and steep dips to the SE (60-80°). The faults offset quartz veins with a typical offset of 2-3 cm for both normal and reverse sense of motion. Of the eighteen faults measured fifteen had a reverse sense of motion, and three had a normal sense of motion. Both reverse and normal faults could be seen offsetting the same quartz vein.

Thirty ductile shear zones were measured, identified by a reduction in grain size, and clear fabric (alkali feldspar alignment) being “dragged” into the slip plane (Figure 3.1.2A). In the early suite, they were approximately 3-5 cm wide. In the late suite, they were approximately 1 cm wide. The lateral extent of the shear zones was difficult to measure as outcrops were commonly patched with peat and moss, and the shear zones would continue underneath. In the early suite, the dip was moderate to steep (30-70°)

generally to the NE and SE. In the late suite, the shear zones generally dipped steeply (50-85°) to the SE and NW, parallel to the brittle faults.

The apparent shear sense was able to be determined for twenty-three shear zones indicated by deflections of fabric. Seven of those shear zones in the early suite were observed on vertical planes: four with apparent normal shear sense and three with apparent reverse sense of motion. The shear zones with reverse sense generally dipped E sub-parallel to thrust faults. The normal sense shear zones dip directions varied between NE and SE. True three-dimensional sense of shear could not be determined due to lack of full three-dimensional exposure.

In the late suite, apparent shear sense of motion for all eighteen shear zones was observed on subhorizontal planes. True three-dimensional sense of shear could not be determined due to lack of full three-dimensional exposure. Nearly all shear zones were located in the SE and W central portion of the late suite. Only two shear zones were seen in far NE corner of the pluton and one in the NW corner. Seven shear zones had apparent sinistral sense of motion, and nine showed apparent dextral sense of motion. Both sinistral and dextral shear zones can been found within the same outcrop. The late suite shear zones dominantly strike NE-SW, but dip direction varied for both sinistral and dextral.

4.2 Magnetic Mineralogy

The characterization of the magnetic mineralogy using the vibrating sample magnetometer (VSM) at the Institute of Rock Magnetism (IRM) provided hysteresis loops for 40 samples throughout the Loch Borralan Pluton (Appendix A). The majority of

the samples were dominated by ferromagnetic mineralogy, but a few samples in the early suite contained some paramagnetic components (Appendix A). This can be determined by comparing the blue line (ferromagnetic data) to the red line (bulk data). If the blue line does not follow the red exactly, then there is a component of paramagnetism also present in the rock. The mineral causing the paramagnetic signal is biotite. Biotite's magnetic susceptibility strongly mimics mineral shape (Bouchez 1997). Therefore, AMS to strain interpretations in samples with paramagnetic components remain straightforward.

The possibility for inverse fabrics caused by single domain magnetite was ruled out with the creation of a Day plot representing the populations of single (SD), pseudosingle (PSD), and multi-domain (MD) mineralogy (Figure 4.2.1; Dunlop 2002). Inverse fabrics occur because the magnetization within an SD grain has no domain walls to shift in the presence of an oblique magnetic field. The result is a slight shift in the easy axis of the SD grain's magnetic field, causing AMS measurements to be offset from true orientation. No samples plotted within the Dunlop (2002) boundaries for SD grains, all samples are either PSD or MD. The early suite is entirely multi-domain, and the late suite has a mixture of both pseudosingle, and multi-domain grains. The Day plot (Figure 4.2.1) can also reveal relative grain size, as the remnant coercivity (H_{rh}/H_c) increases grain size increases. Generally MD grains are larger than PSD, and PSD are larger than SD grains. Multi-domain AMS fabrics commonly coincide with deformation strain orientations (Bouchez 1997).

Curie temperature measurements were conducted to determine which ferromagnetic mineral is responsible for the AMS fabric. Both samples from the early suite and late suite showed the same Curie point temperature of ~560ºC (Figures 4.2.2

and 4.2.3). This Curie temperature is slightly low for pure magnetite (~580ºC), but fits well for a composition of titanomagnetite of approximately 80% magnetite to 20% titanomagnetite (Hunt et al. 1995). The rightward shift of the Day plot samples also coincides with a titanomagnetite signature (Figure 4.2.1; Dunlop 2002). The thermomagnetic data was irreversible on cooling suggesting that new material is being created at high temperatures (Butler 1992). The cause for the creation of new magnetic material is due to oxy-exsolution, sometimes referred to as "deuteric oxidation" (Butler 1992). During oxy-exsolution, ilmenite will convert to magnetite near 700ºC (Butler 1992). The combination of the sub ~560ºC Curie temperature, and the shifted Day plot suggest a dominant magnetic mineralogy of titanomagnetite with slight oxidation.

4.3 Anisotropy of Magnetic Susceptibility (AMS)

All AMS results are shown in Appendix B and the site averaged results are shown in Table 4.2. Bulk susceptibility (K_m) measurements corroborate the hysteresis and thermomagnetic data throughout the pluton with strong site averaged K_m values generally between 10^{-2} to 10^{0} SI, indicating titanomagnetite as the dominant mineralogy (Table 4.2; Borradaile and Jackson 2010). Anisotropy magnitude (P_j) values are similar throughout the pluton and between each suite, generally between 1.010 and 1.150 (Table 4.2). The anisotropy shape parameter (T) is prolate ($T<0$) in the eastern and south-eastern portion of both the early and late suite, but the majority of the pluton has oblate fabric ($T>0$; Table 4.2). The early suite has a higher average T value than the early suite. The largest magnetic grain sizes seen in the early suite correspond with the larger average K_m values in the early suite (Table 4.2 and Figure 4.2.1).

Comparison between AMS orientations and outcrop scale measurements was made for 15 stations where both field and AMS data was available (Figure 4.3.1). In the early suite, AMS K_1 directions generally parallel field lineation, and K_3 directions trend parallel to field pole to foliation measurements. In the late suite where field lineation measurements are available, K_1 measurements follow similar trends. Field pole to foliation measurements are more variable and differ from K_3 measurements.

Complete AMS data can be seen in Appendix B. Any outlying, inconsistent, or standard deviations from suite averages were not included in the final analysis (Figure 4.1.1 and 4.3.1, Table 4.2). Measurements that had standard deviations ($L>0.4$, $F>0.1$, $P_j>0.1$), or ($K_m>20{,}000$) in the late suite were not considered for interpretation. These measurements are likely either isolated anomalies or contaminated samples. K_m values ranged widely between stations, but remained constant within each sampling station. Therefore, K_m was not used as criteria for elimination in the early suite.

The AMS lineations (K_1) of the early suite generally plunge shallowly to the southeast, parallel to thrust transport direction (Figure 4.1.1 and 4.3.2). These lineation directions are parallel with the long axes of internal pseudoleucite aggregates measured by Searle et al. (2010) in the Aultivullin quarry (stations LB08-03 and LB12-04; Figure 3.1.1) on the southeastern margin of the Loch Borralan Pluton. Foliations in the early suite strike approximately 030, and dip roughly 20° to the southeast (Figure 4.1.1 and 4.3.3). Foliations are subparallel to the strike of both the major and minor regional thrusts. Nearly all early suite measurements show oblate fabrics ($T>0$; Table 4.2).

The late suite mean orientation of AMS lineations (K_1) plunges extremely shallowly (~1°) to the southwest (195°; Figures 4.1.1 and 4.3.2). The majority of lineation measurements plunge shallowly to either the southwest or northeast sub parallel to the strike of the thrust faults (Figure 4.1.1). Less dominant orientations of lineations in the northwest parallel thrust transport direction, and steeply dipping central lineations parallel regional strike thrust. Foliations in the late suite range widely in dip degree, but all generally strike NE-SW parallel to thrust faults (Figure 4.1.1 and 4.3.3). There are dominantly oblate fabrics ($T>0$) in the late suite, but some prolate fabrics ($T<0$) also exist (Table 4.2).

4.4 Petrographic Analysis

The mineralogy in the early suite (Figure 4.4.1 and 4.4.2) is characterized by approximately 85% orthoclase feldspars, 5% natrolite, 5% melanite, 3% plagioclase, 1% biotite, and 1% opaque minerals including titanomagnetite and ilmenite. Late suite mineralogy in the southeastern portion of the pluton (Figure 4.4.3) was very rich in orthoclase/microcline (93%), with some minor plagioclase (3%), quartz (2%), biotite (1%), and opaque minerals (1%). The central and northwestern parts of the late suite (Figure 4.4.4) have similar mineralogies with approximately 80% orthoclase/microcline, 15% quartz, 3% plagioclase, 1% biotite, and 1% opaque minerals.

The early suite has a very large orthoclase feldspar grains (5-10 mm diameter), while natrolite, melanite, and plagioclase are typically <1-2 mm. The large orthoclase feldspars continue in the southeastern portion of the late suite with grains typically on the scale of approximately 3-7 mm, and plagioclase <2-3 mm. In the northwestern extent of

the late suite, orthoclase grain size is reduced to 2-5 mm, plagioclase is typically <1 mm, and quartz <0.5 mm.

Feldspars

Both the early and late suites are dominated by orthoclase feldspars. In all thin sections, a perthitic texture is present (Figure 4.4.1 and 4.4.5). Perthite, and its closely related structure myrmekite (seen occasionally, Figure 4.4.4), are an intergrowth of albite lamellae in K-feldspar (quartz and K-feldspar in myrmekite), formed by solid-state exsolution of a homogeneous alkali feldspar solid solution during slow cooling in igneous and metamorphic rocks (Simpson and Wintsch 1989; Vernon 2004). Plagioclase can be seen both faulted (Figure 4.4.2) and bent (Figure 4.4.3). Both orthoclase and plagioclase developed strong undulose extinction (Figure 4.4.6 and 4.4.7). Straight microfractures cut across both orthoclase and plagioclase grains, and in the late suite, these fractures are typically filled with quartz. Grain boundaries of orthoclase are highly irregular and 'bulged' which occurs during the transition from magmatic to solid-state deformation (Figure 4.4.2; Vernon 2004).

Quartz

Quartz is only seen in the late suite magma, and predominantly exists only in the northwestern extent of the pluton. Quartz exists in three forms: some grains are around 0.5-1mm with irregular 'bulged' boundaries (Figure 4.4.8), some grains of similar size have clear boundaries (4.4.9), and the others are smaller recrystallized grains (<0.1mm) with very well defined boundaries (Figure 4.4.4 and 4.4.8). All three types of quartz grains exhibit undulose extinction (Figure 4.4.8). Microfractures do not typically cut

quartz grains, but in some cases they do (Figure 4.4.8). Rather, quartz fills in the fractures that cut feldspars (Figure 4.4.10).

Fractures typically cut alkali feldspars and plagioclase grains. Some fractures cut across multiple grains (Figure 4.4.5). The fractures are typically straight, and do not have any obvious preferred orientation. Some fractures form 60-120° conjugate sets relative to the $K_1>K_2>K_3$ directions, but this relationship is not present in all thin sections (Figure 4.4.5). Locally, microfractures offset grain boundaries. The quartz in the southeastern portion of the pluton has more pervasive bulged grain boundaries (Figure 4.4.11).

Other Minerals

The early suite hosts melanite garnet, a member of the andradite garnet group (Figure 4.4.12). Melanite is a Ti-rich garnet that is a primary mineral commonly found in undersaturated alkaline igneous rocks (Deer et al. 1982). Natrolite is considered a low-grade zeolite facies metamorphic mineral, common to mafic igneous intrusions. However, in alkaline intrusions, particularly nepheline syenites, natrolite is derived from fluid enhanced, late stage cooling, deuteric alteration reactions with nepheline (Deer et al. 2004). Natrolite is seen as fibrous intergrowths between orthoclase grains (Figure 4.4.13). Muscovite mica is seen rarely as an accessory mineral in the early suite. Neither muscovite, natrolite, nor melanite exhibits any preferred alignment suggesting they are all primary igneous minerals, and not produced by metamorphic reactions.

There were no noticeable differences in microstructures between thin sections cut parallel, or perpendicular to magnetic lineation. No obvious primary magmatic textures were seen in any thin sections.

4.5 Shape Preferred Orientation (SPO)

SPO measurements are generally weak with the average shape ratio (R) being 1.147 for feldspars, and 1.193 for opaque minerals (Figure 4.5.1). The shape ratios for the plane parallel to lineation (K1>K3) has a higher average shape ratio at 1.164 compared to 1.130 for the lineation perpendicular face (K2>K3), but the variability of shape ratios within a plane are greater than the difference between planes. Shape ratios for feldspars are slightly higher in the early suite and the southeastern portion of the late suite, and lower in the northwestern part of the late suite. Sites that are closer to pluton or suite margins exhibit higher shape ratios (e.g. LB12-04C, LB08-04B, LB08-06B). Mean length vector (A) does not vary much between feldspar and opaque grains within each plane.

The dominant orientations of feldspars in the K_1>K_3 plane for the early suite is approximately 24°→079, and 08°→005 for the late suite (Figure 4.5.2). The dominant orientations of feldspars in the K_2>K_3 plane for the early suite is approximately 12°→212, and 23°→042. The mean K_1 orientation for the early suite is 34°→115, and 01°→195 for the late suite. The mean K_2 orientation for the early suite is 03°→206, and 18°→105 for the late suite. The SPO for the early suite and the late suite K_1>K_3 plane parallels the AMS data very well. There is a difference in the K_2>K_3 orientation of about 60° between the SPO and AMS orientations in the late suite.

The shape ratio can also determine whether the minerals generally have a stronger foliation or lineation when comparing the average ratios between the K_1>K_3 and the K_2>K_3 planes. The SPO measurements indicate that the rock has a stronger foliation since

K_1 and K_2 have similar magnitudes. The average shape ratio of the K_2>K_3 plane is actually slightly larger (1.18) than the K_1>K_3 plane (1.16). This is consistent with strong foliations and poor lineations as observed in the field.

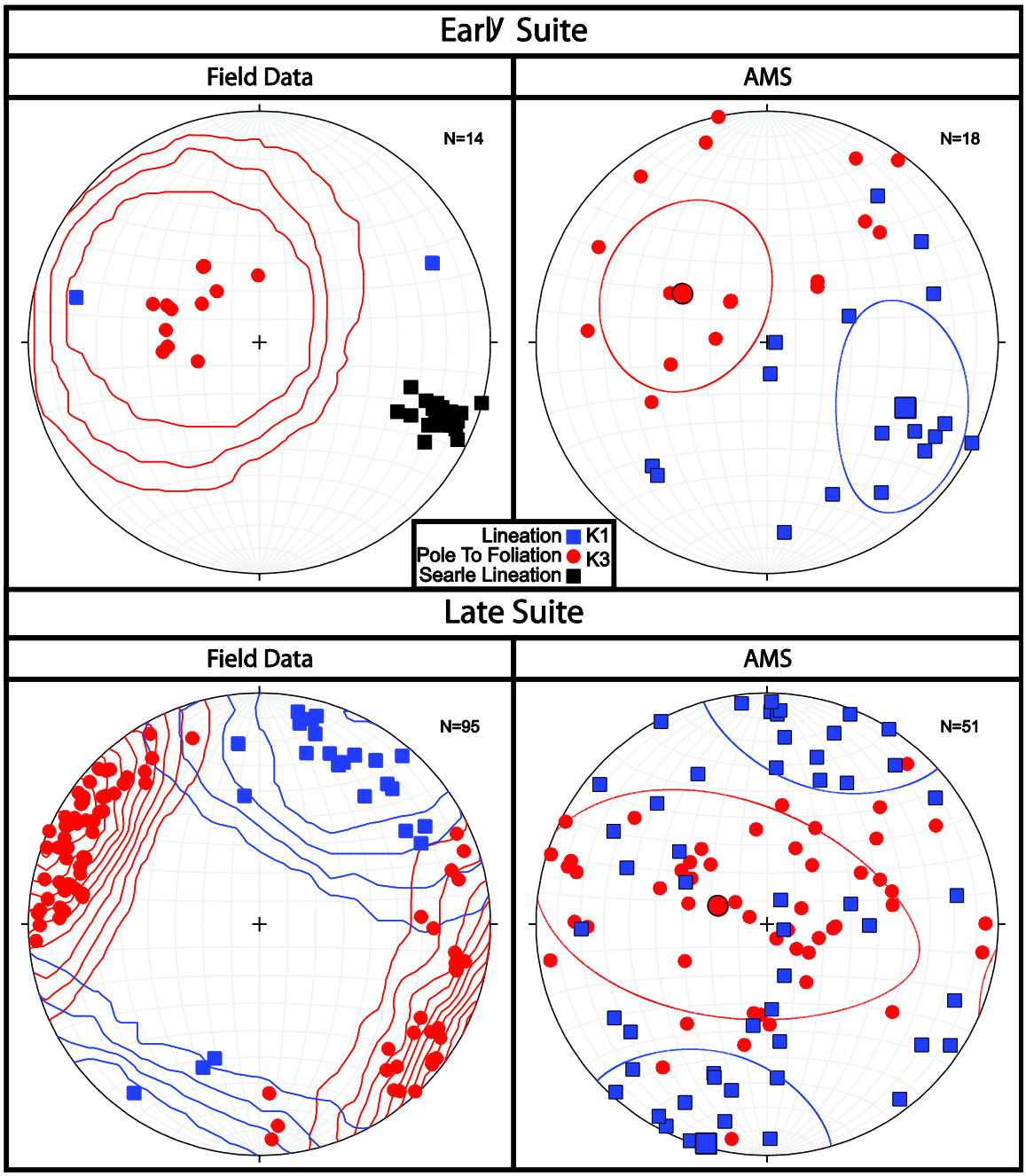

Figure 4.1.1: Lower hemisphere equal area stereonet projections of macroscopic alkali feldspar field foliation and lineation measurements (left), and AMS measurements (right) in early suite (top) and late suite (bottom). K_1 orientation corresponds to maximum strain axis (S_1), and K_3 to the minimum strain axis (S_3). Stretching lineations of pseudoleucite aggregates measured by Searle et al. (2010) shown overlain on early suite field data stereonet. Kamb (2%) contouring used for field data stereonets, and confidence ellipses (95%) calculated using Anisoft42.exe for AMS stereonets.

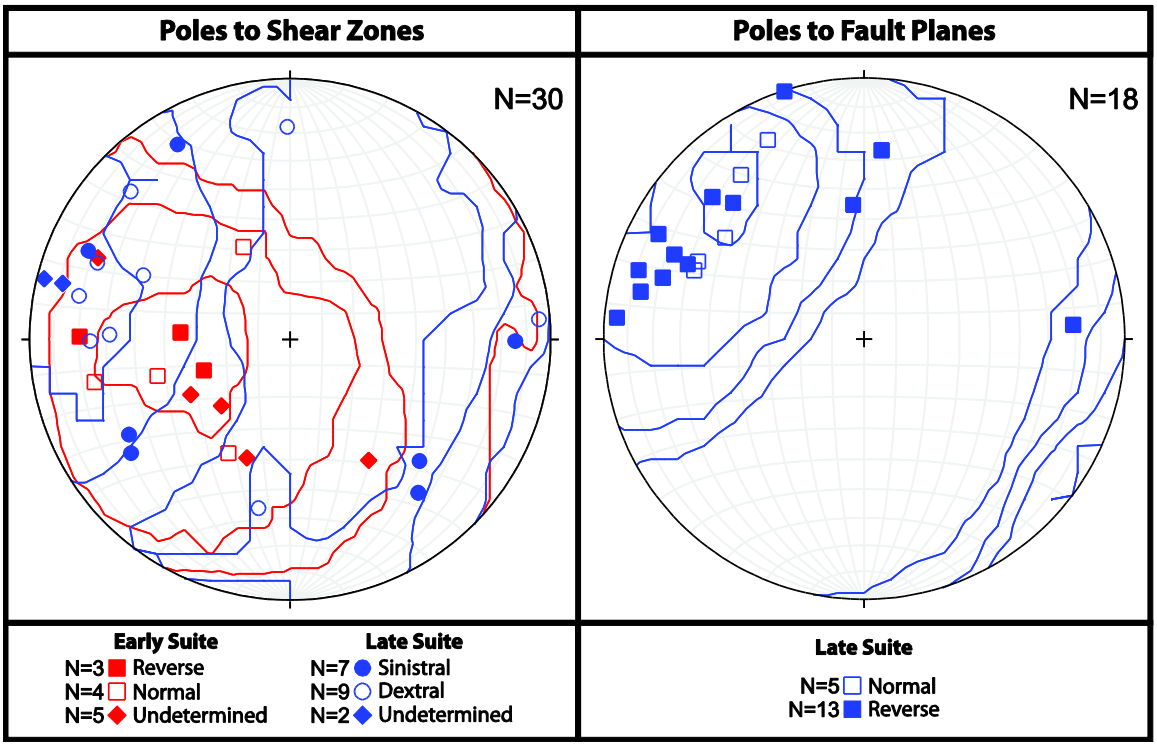

Figure 4.1.2: Poles to planes of shear zones and faults represented on lower hemisphere equal area stereonets. Kamb contouring (2%).

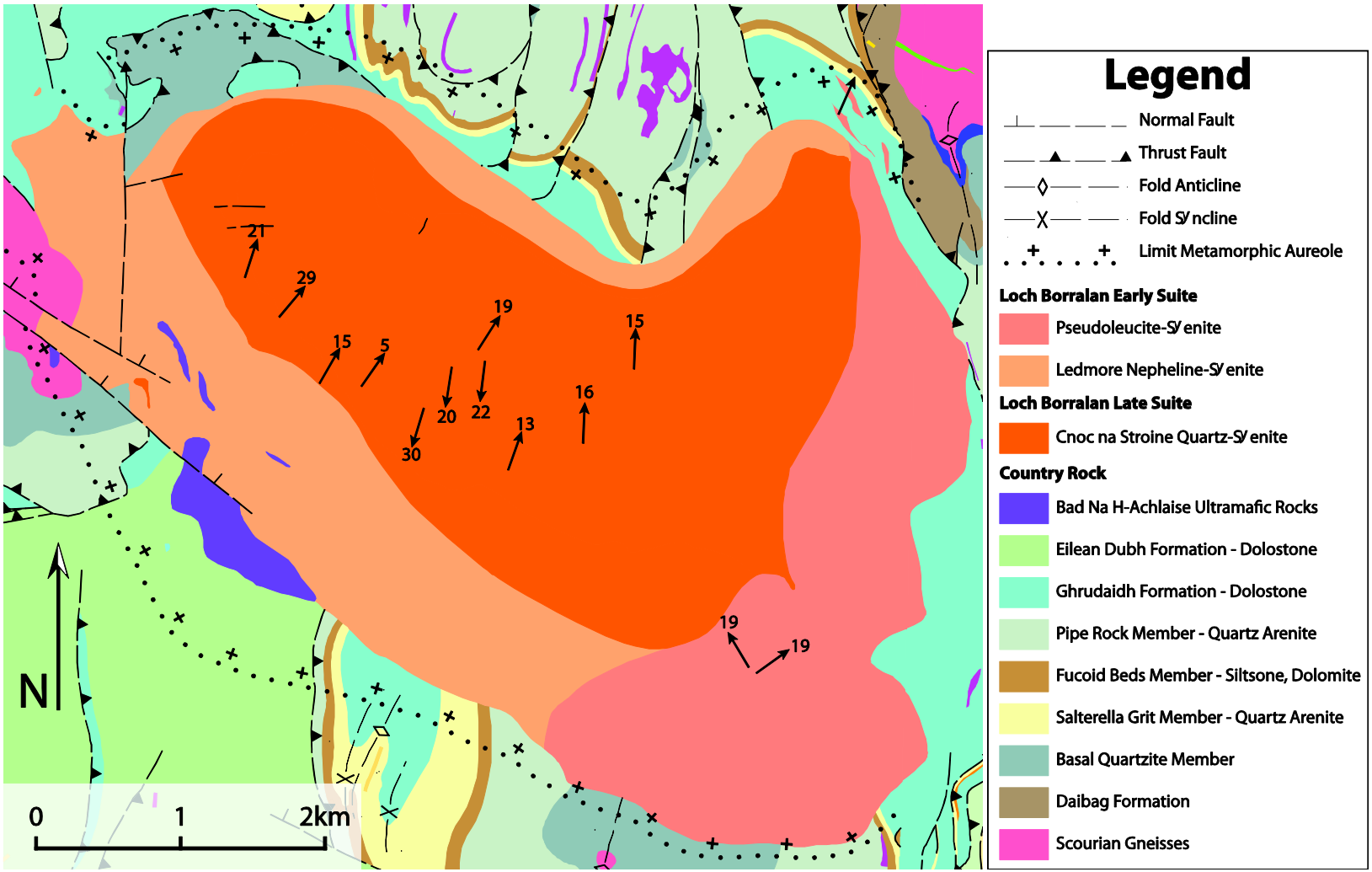

Figure 4.1.3: Map of Loch Borralan Pluton showing lineation field measurements of preferred orientation of alkali feldspar long axes. Modified from British Geological Survey (2013).

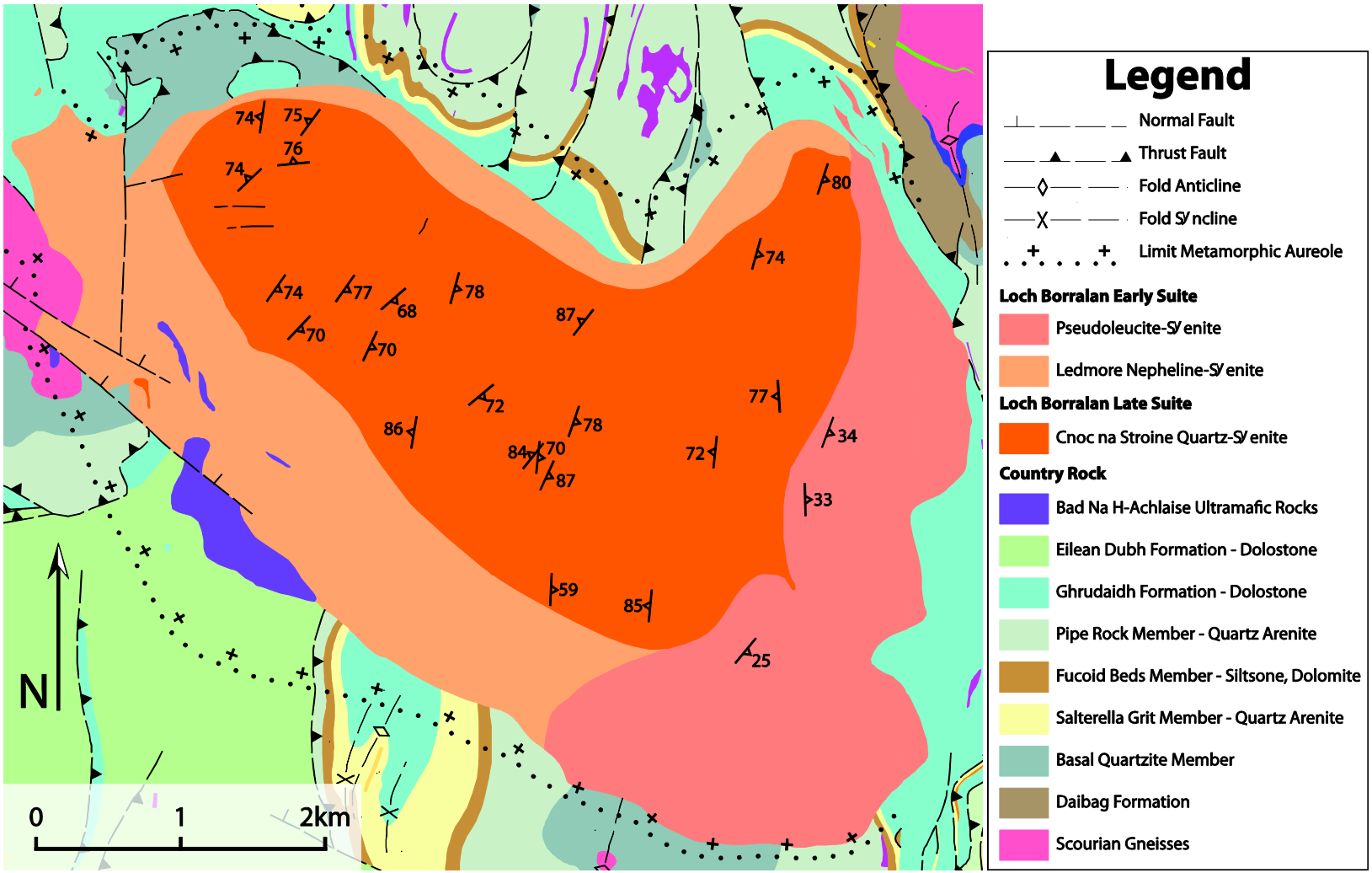

Figure 4.1.4: Map of Loch Borralan Pluton showing foliation field measurements of planar preferred orientation of alkali feldspars. Modified from British Geological Survey (2013).

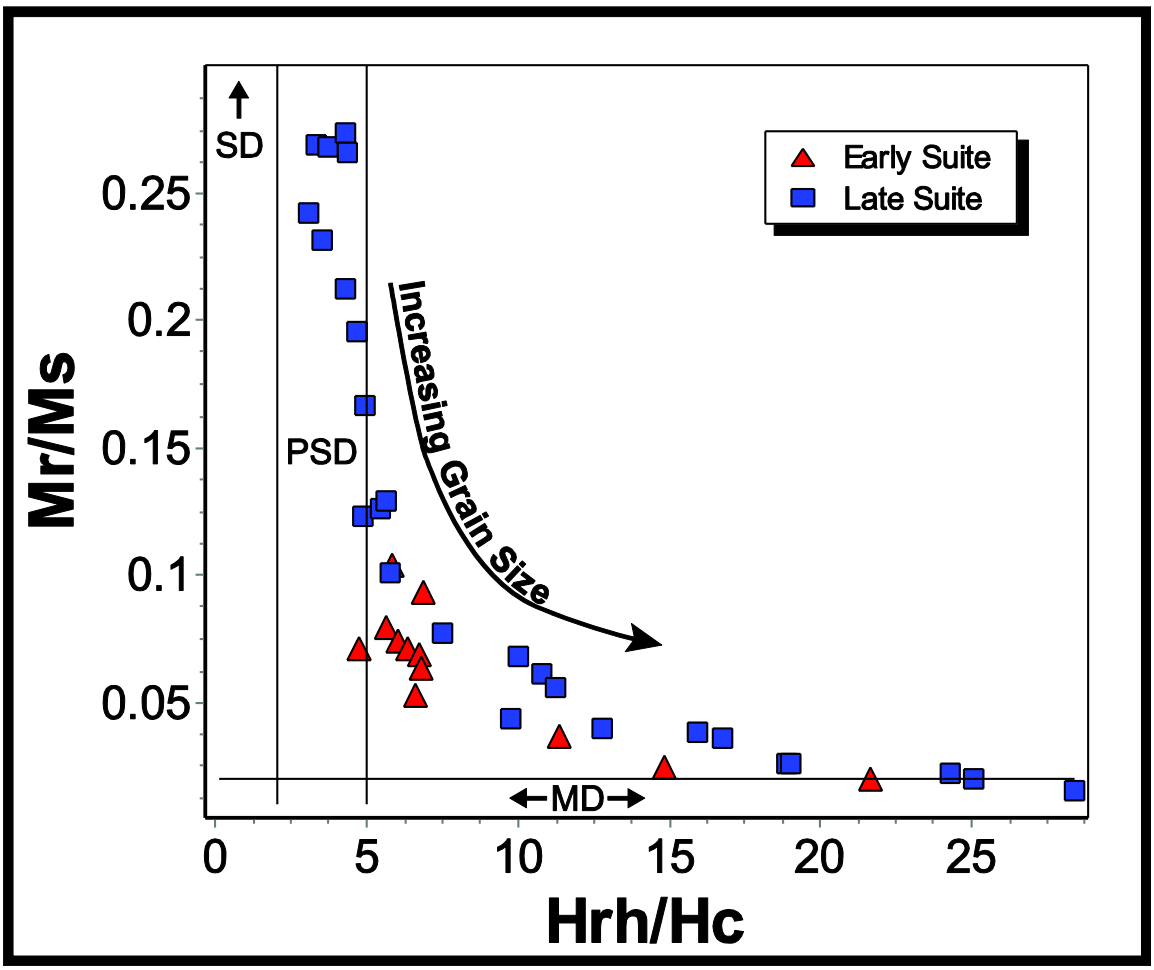

Figure 4.2.1: Day plot (Day et al. 1977) showing the distribution of samples from the Loch Borralan pluton with Dunlop et al. (2002) boundaries for single domain (SD), psuedosingle domain (PSD), and multidomain (MD) magnetite. Ms, saturation magnetization; Mr, remanent saturation; Hc, magnetic coercivity; Hrh, mass estimated coercivity of magnetic remanence.

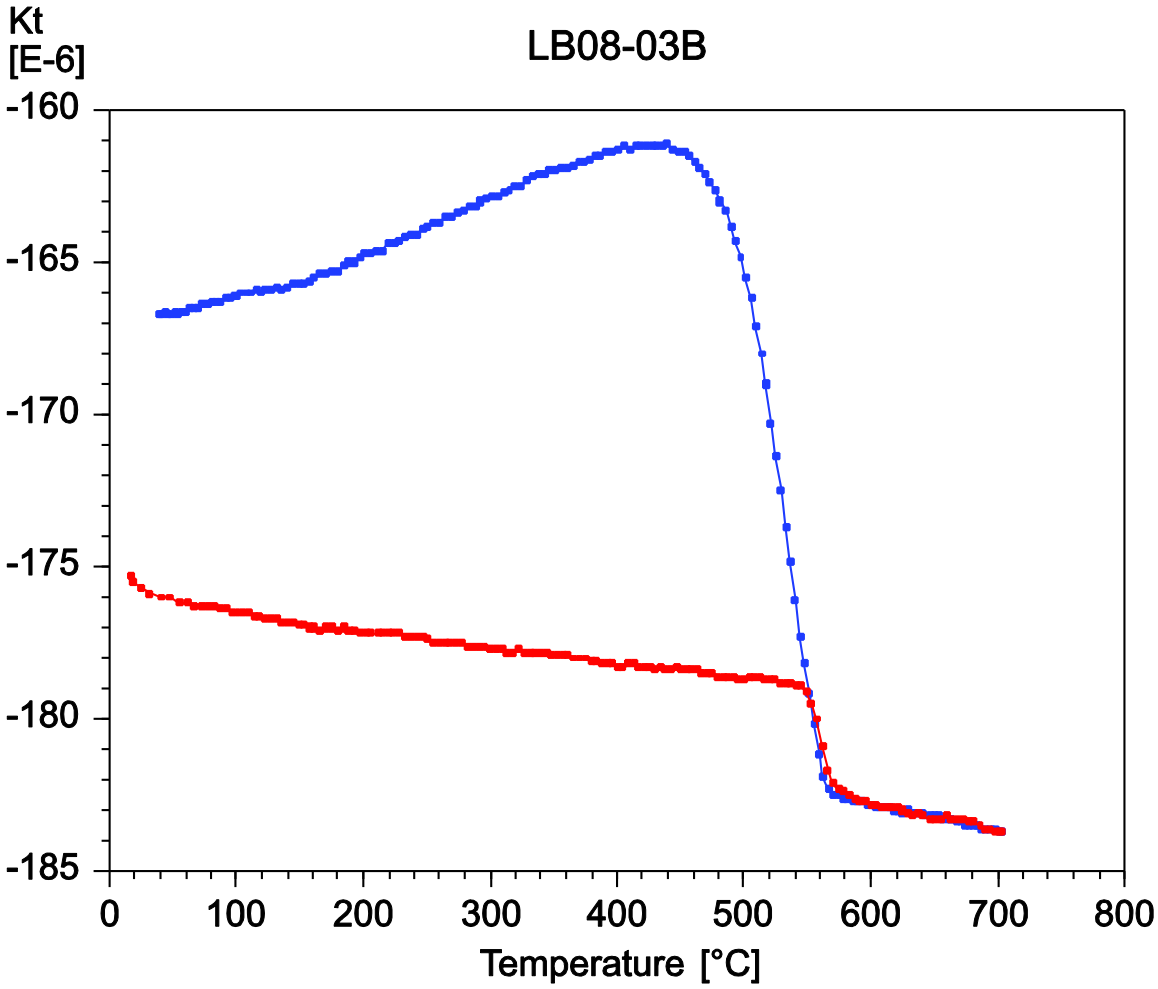

Figure 4.2.2: Curie point measurement of early suite sample showing approximate ~560°C temperature indicative of low temperature oxidation titanomagnetite. Red line is heating, blue line is cooling curve. Kt, total susceptibility.

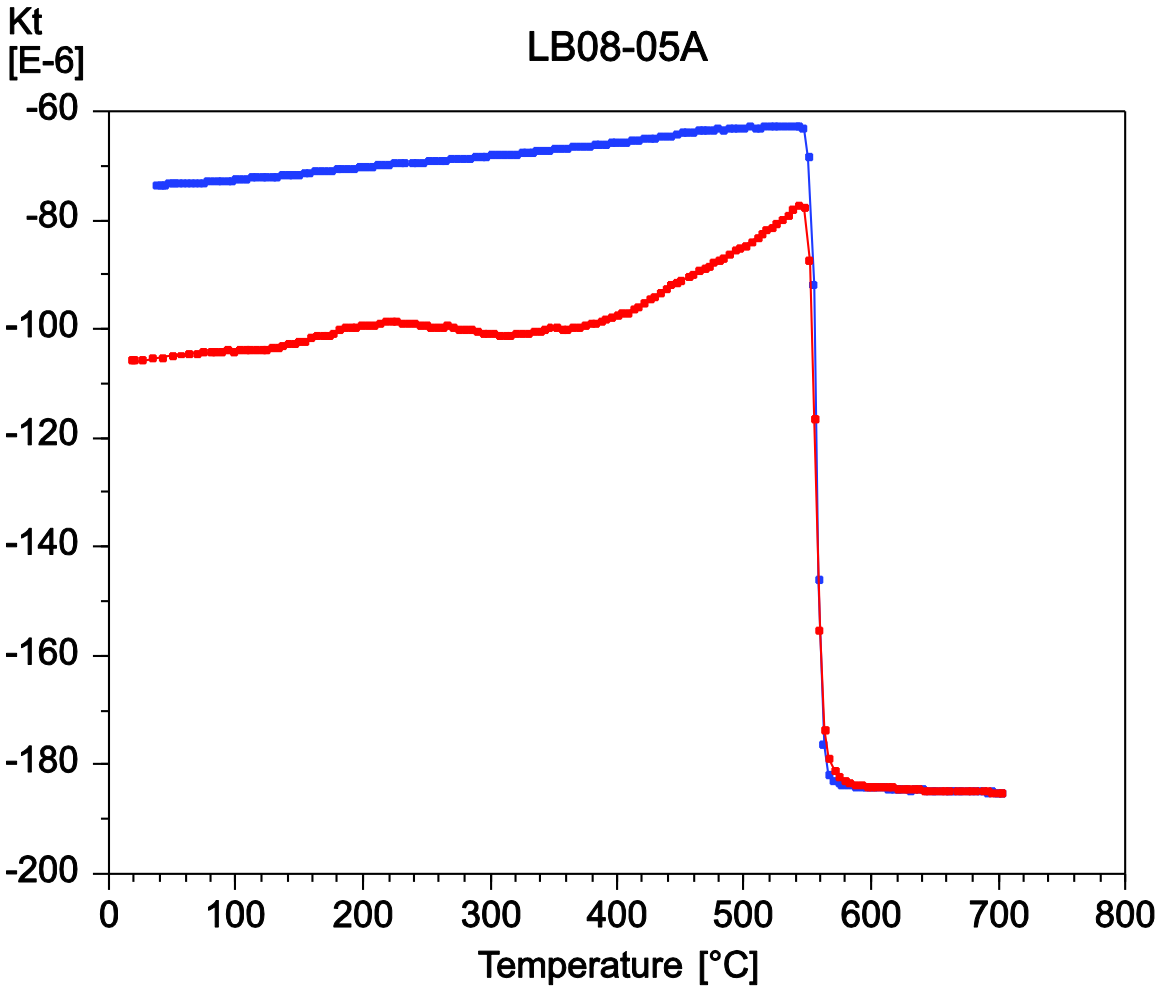

Figure 4.2.3: Curie point measurement of late suite sample showing approximate ~560°C temperature indicative of low temperature oxidation titanomagnetite. Red line is heating, blue line is cooling curve. Kt, total susceptibility.

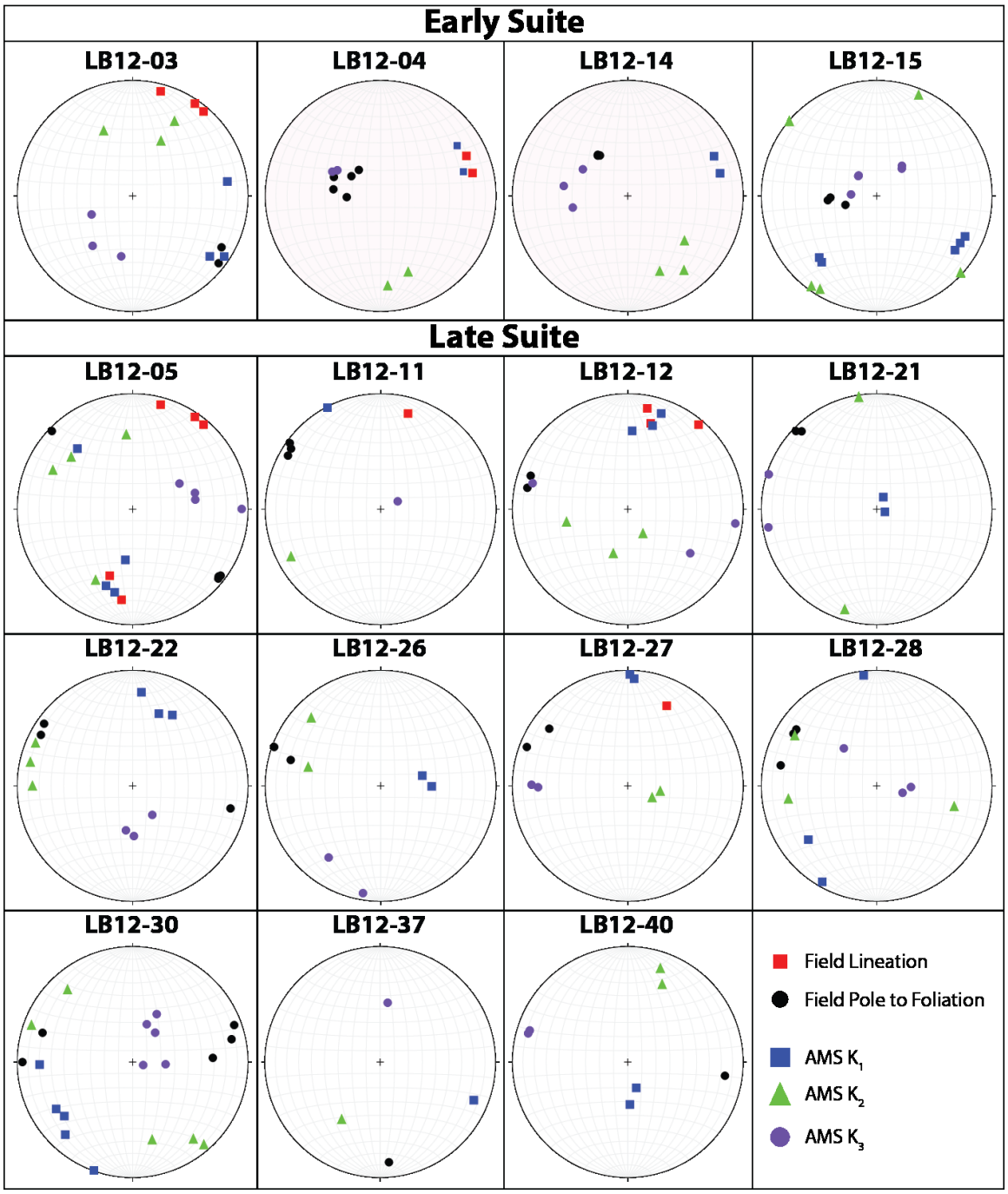

Figure 4.3.1: Comparison between AMS and field measurement. 15 stations had overlapping field and AMS measurements. K_1 parallels maximum strain axis (S_1), K_2 to intermediate strain axis (S_2), and K_3 to minimum strain axis (S_3).

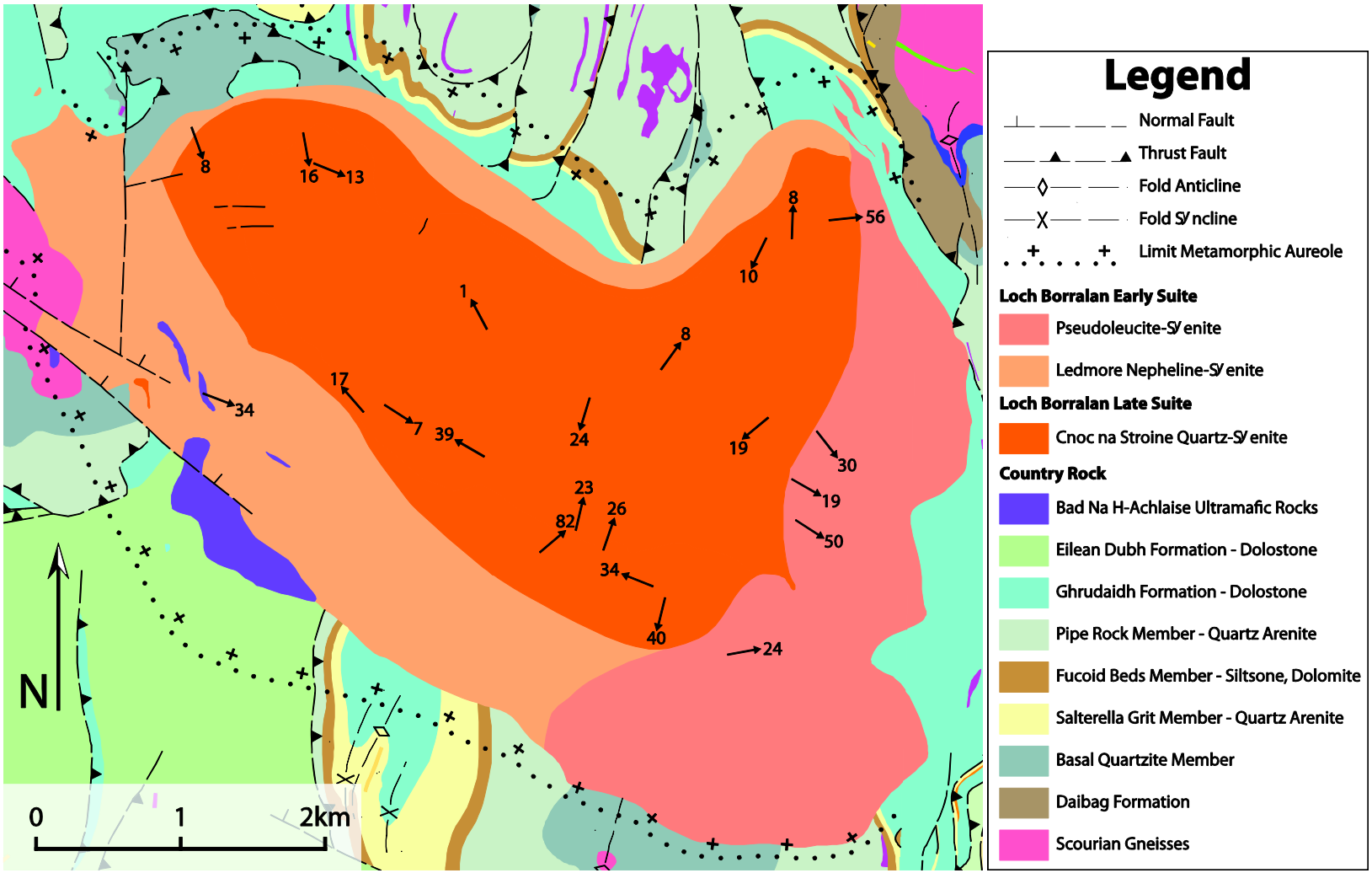

Figure 4.3.2: Map of the Loch Borralan Pluton showing AMS lineations. Modified from British Geological Survey (2013).

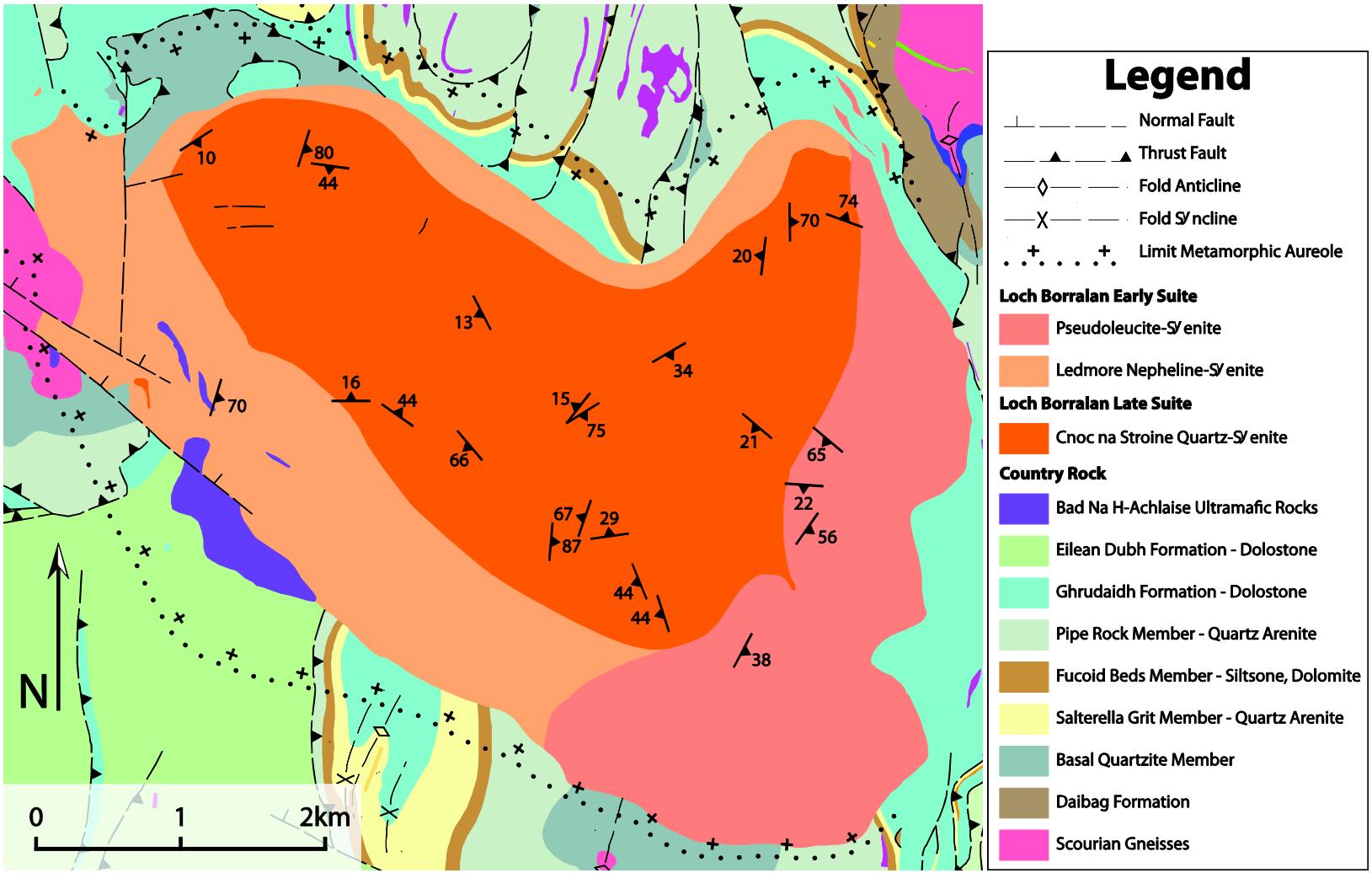

Figure 4.3.3: Map of the Loch Borralan Pluton showing AMS foliations. Modified from British Geological Survey (2013).

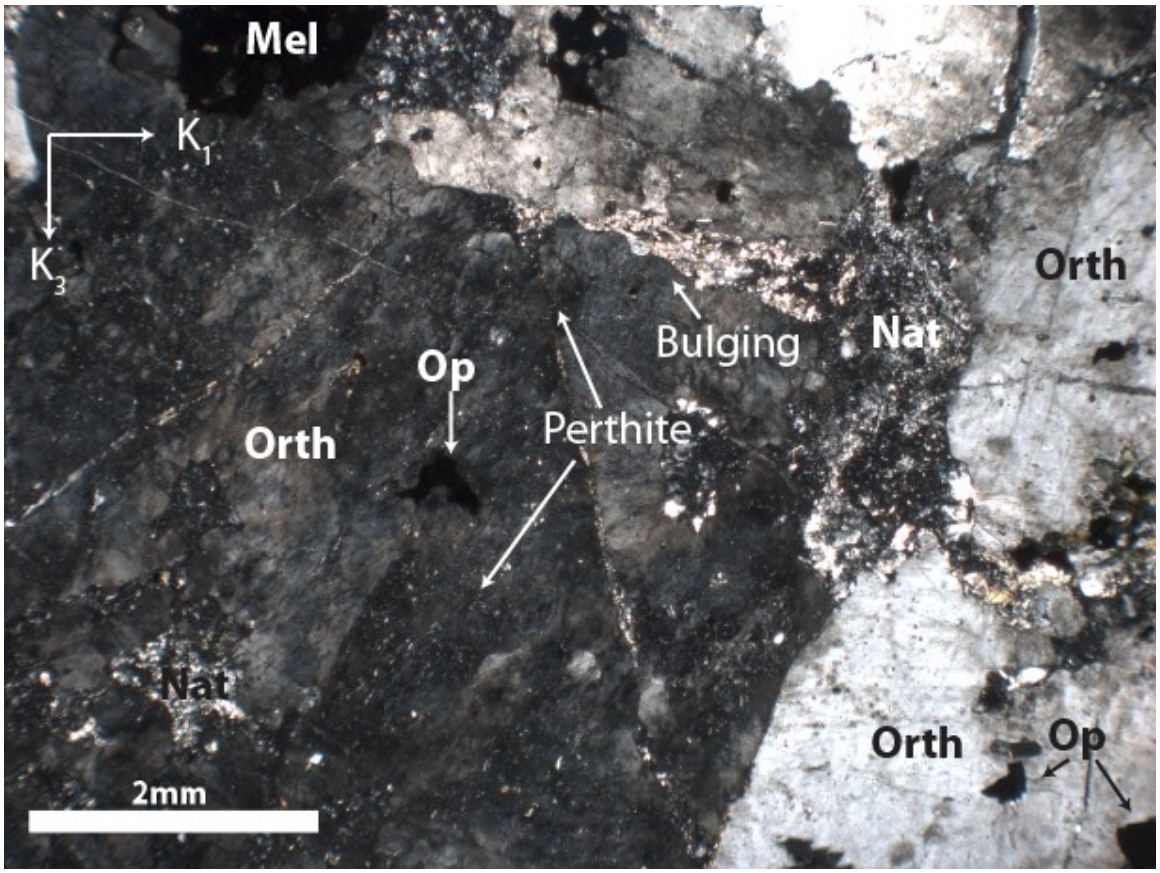

Figure 4.4.1: Early suite thin section (LB12-04C=; K_1K_3 plane, XPL) image showing multiple large orthoclase grains with well developed perthite texture. Bulging grain boundaries can also be seen around the rim of orthoclase grains. Orth, orthoclase; Nat, natrolite; Mel, melanite garnet; Op, opaque minerals.

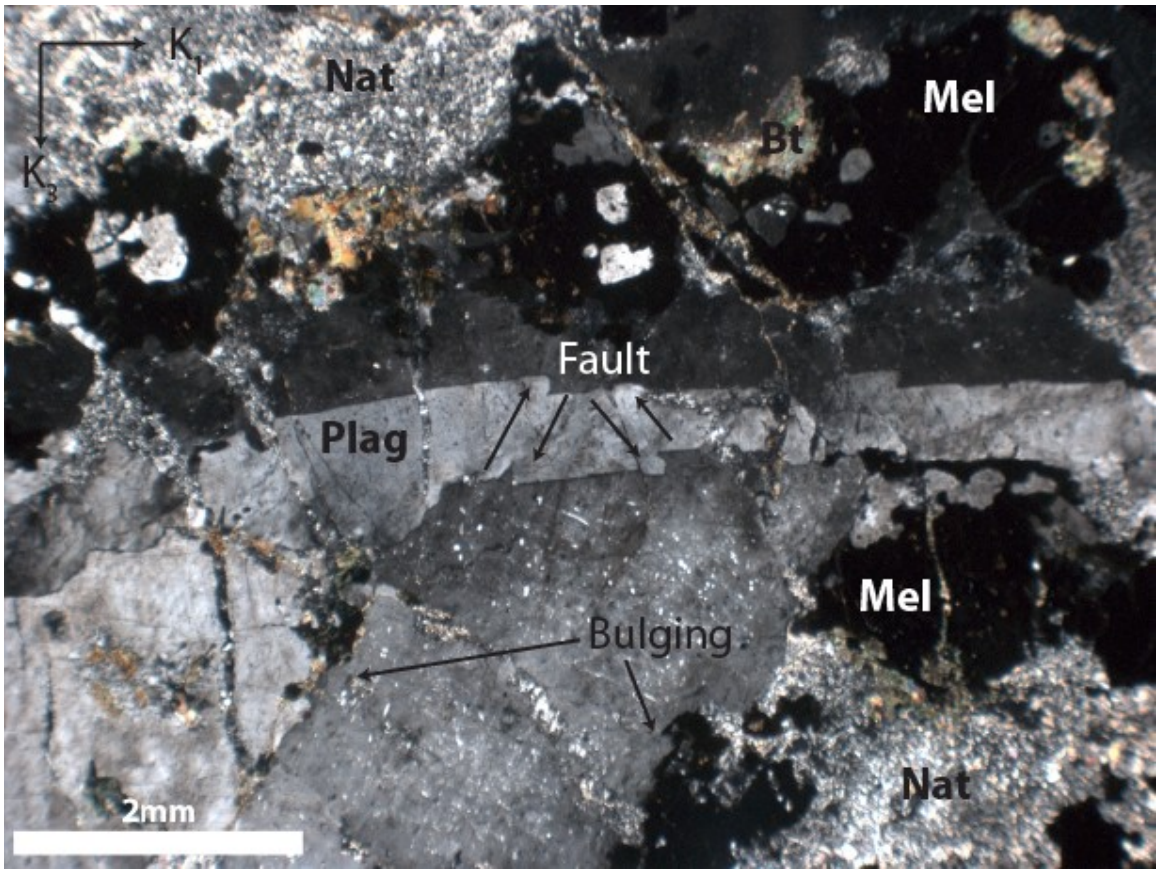

Figure 4.4.2: Early suite thin section (LB12-04C=; K_1K_3 plane, XPL) image showing a micro reverse fault within a plagioclase grain. Fibrous natrolite (Nat) and melanite (Mel) minerals in the surrounding matrix. Plag, plagioclase; Nat, natrolite; Bt, Biotite.

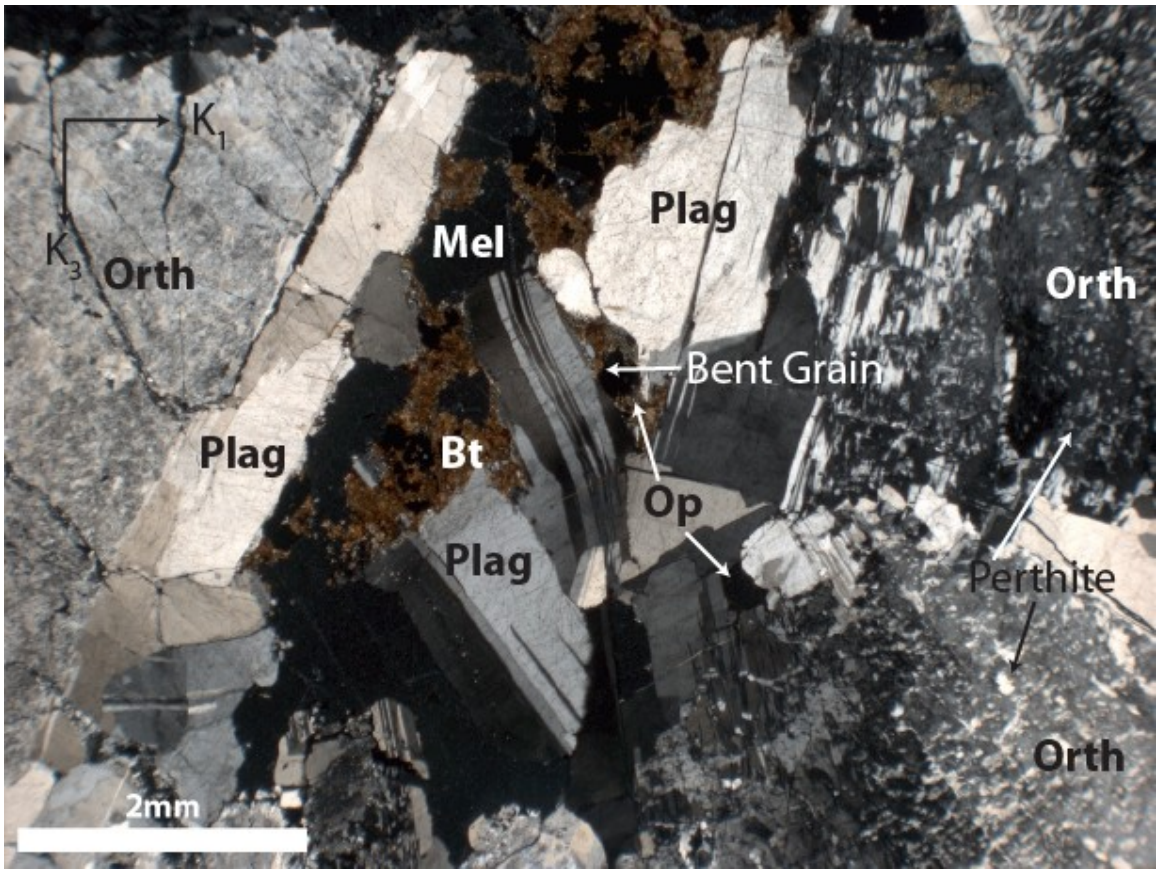

Figure 4.4.3: Late suite thin section (LB08-04B=; K_1K_3 plane, XPL) image showing a bent plagioclase grain (dislocation creep). Surrounding the plagioclase grains are highly perthitic orthoclase grains. The green-brown minerals are fine grained biotite. Orth, orthoclase; Plag, plagioclase; Mel, melanite garnet; Bt, biotite; Op, opaque minerals.

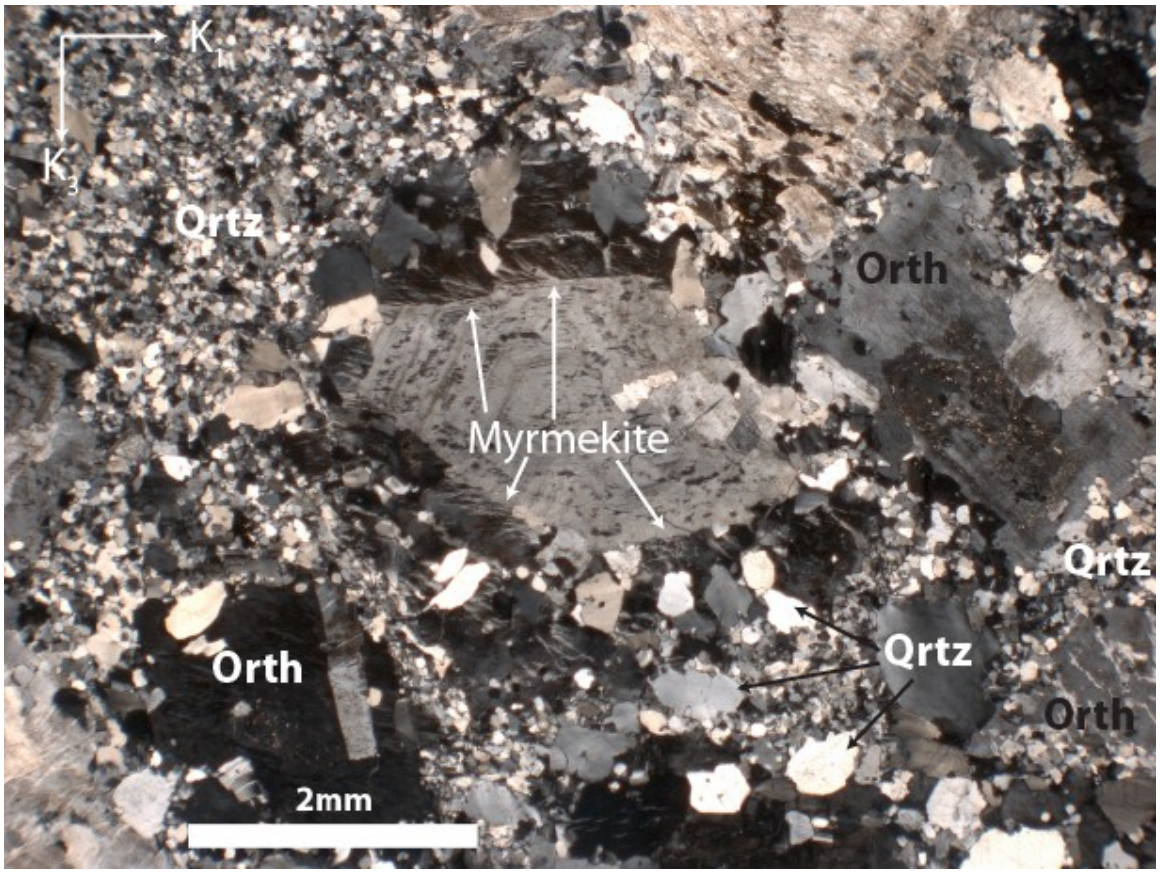

Figure 4.4.4: Late suite thin section (LB08-06B=; K_1K_3 plane, XPL) image showing a zoned feldspar crystal with myrmekite wings surrounding it. Myrmekite was occasionally seen in thin sections. Orth, orthoclase; Qrtz, quartz.

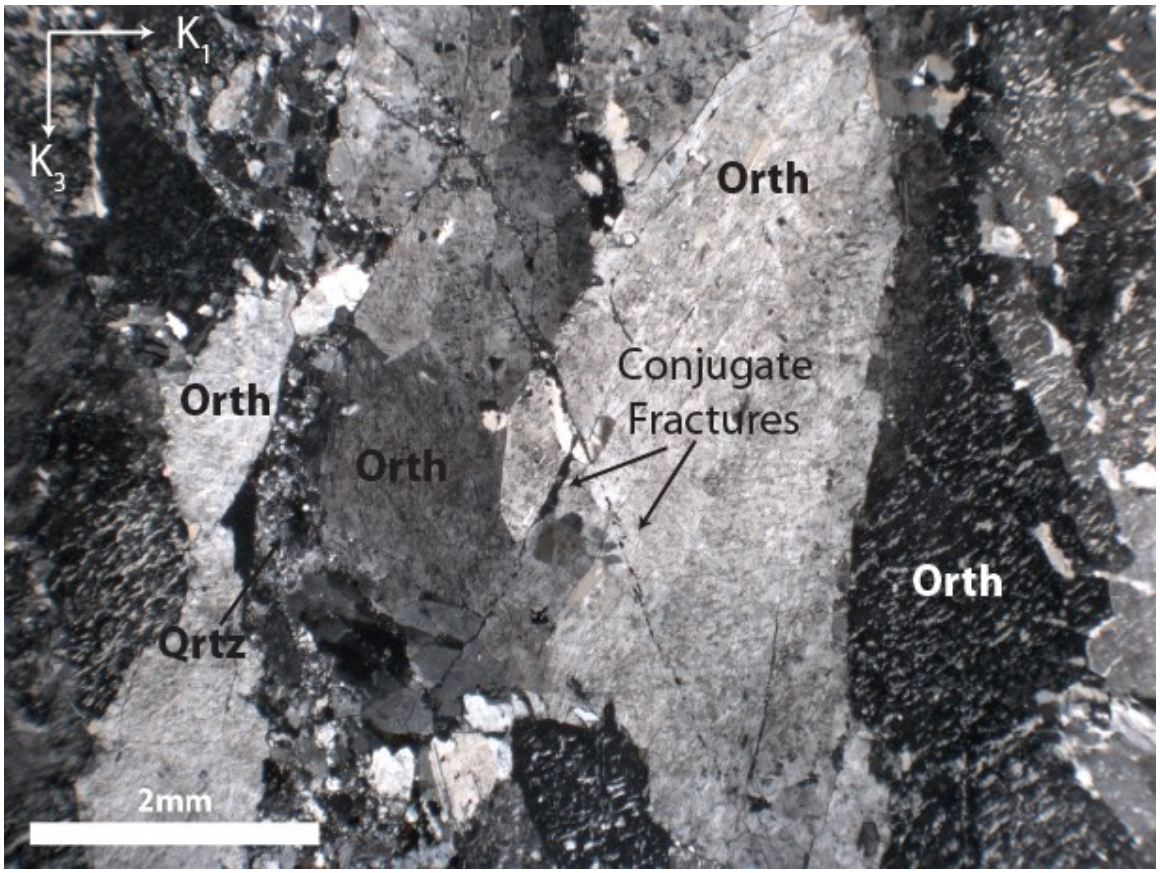

Figure 4.4.5: Late suite thin section (LB08-04B=; K_1K_3 plane, XPL) image showing a well developed microfracture that has since been partially filled with quartz. Intense perthite in surrounding orthoclase grains. Orth, orthoclase; Qrtz, quartz.

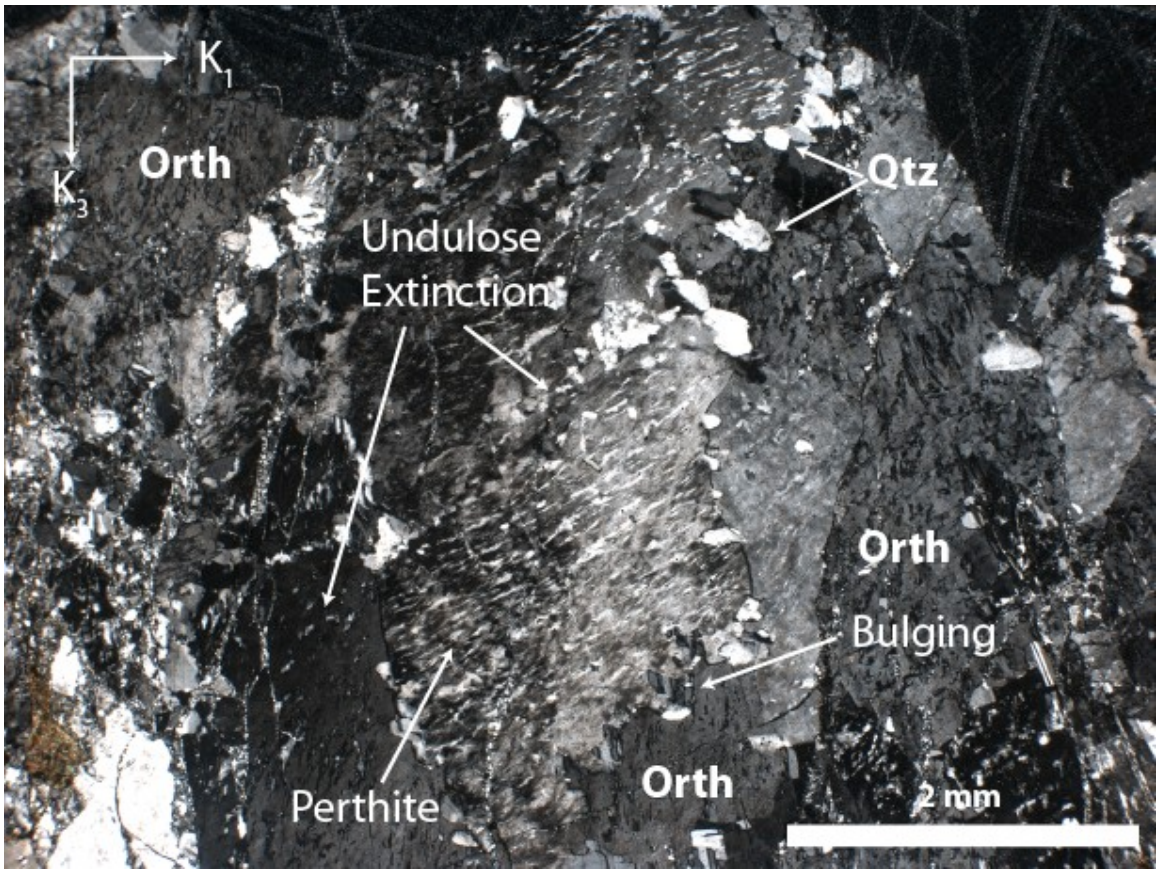

Figure 4.4.6: Late suite thin section (LB08-04B=; K_1K_3 plane, XPL) image showing a well developed undulose extinction in orthoclase feldspar with perthite texture. Orth, orthoclase; Qrtz, quartz.

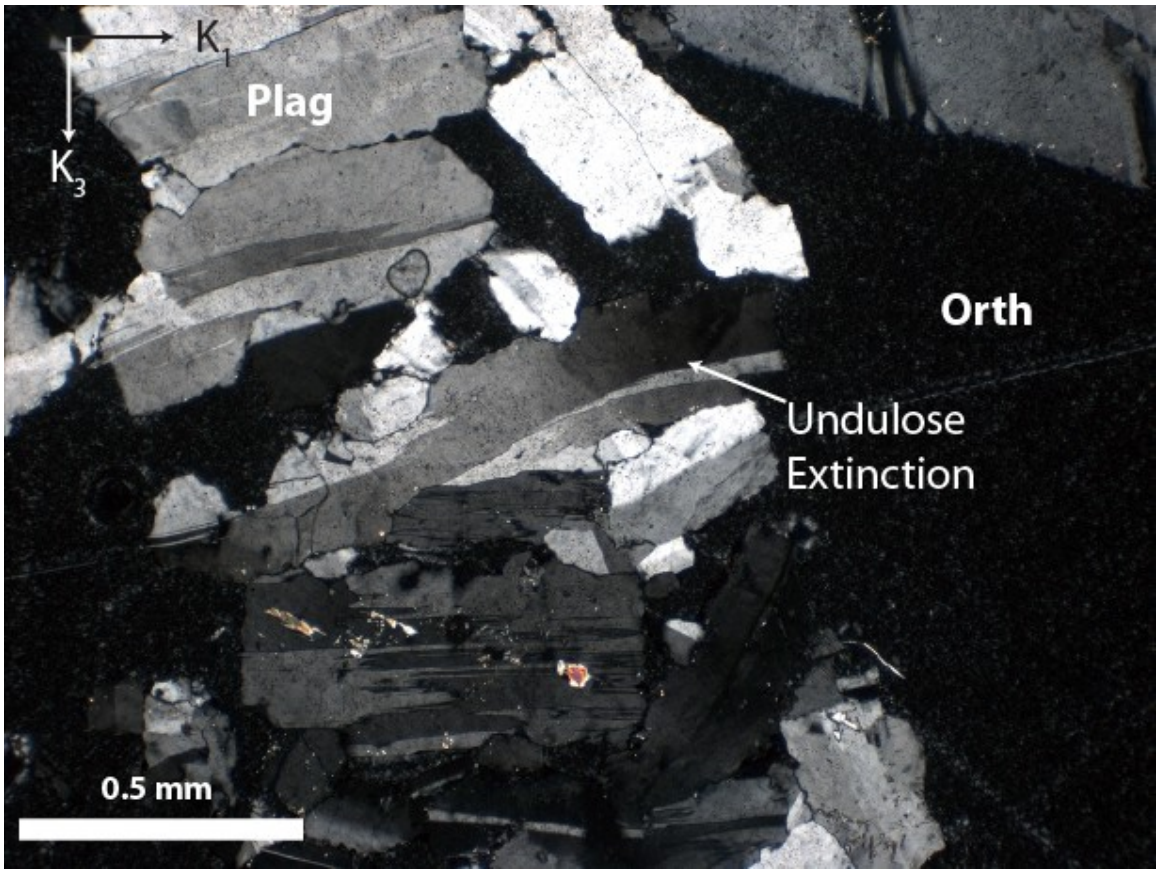

Figure 4.4.7: Late suite thin section (LB08-04B=; K_1K_3 plane, XPL) image showing undulose extinction of a plagioclase feldspar grain. Orth, orthoclase; Qrtz, quartz.

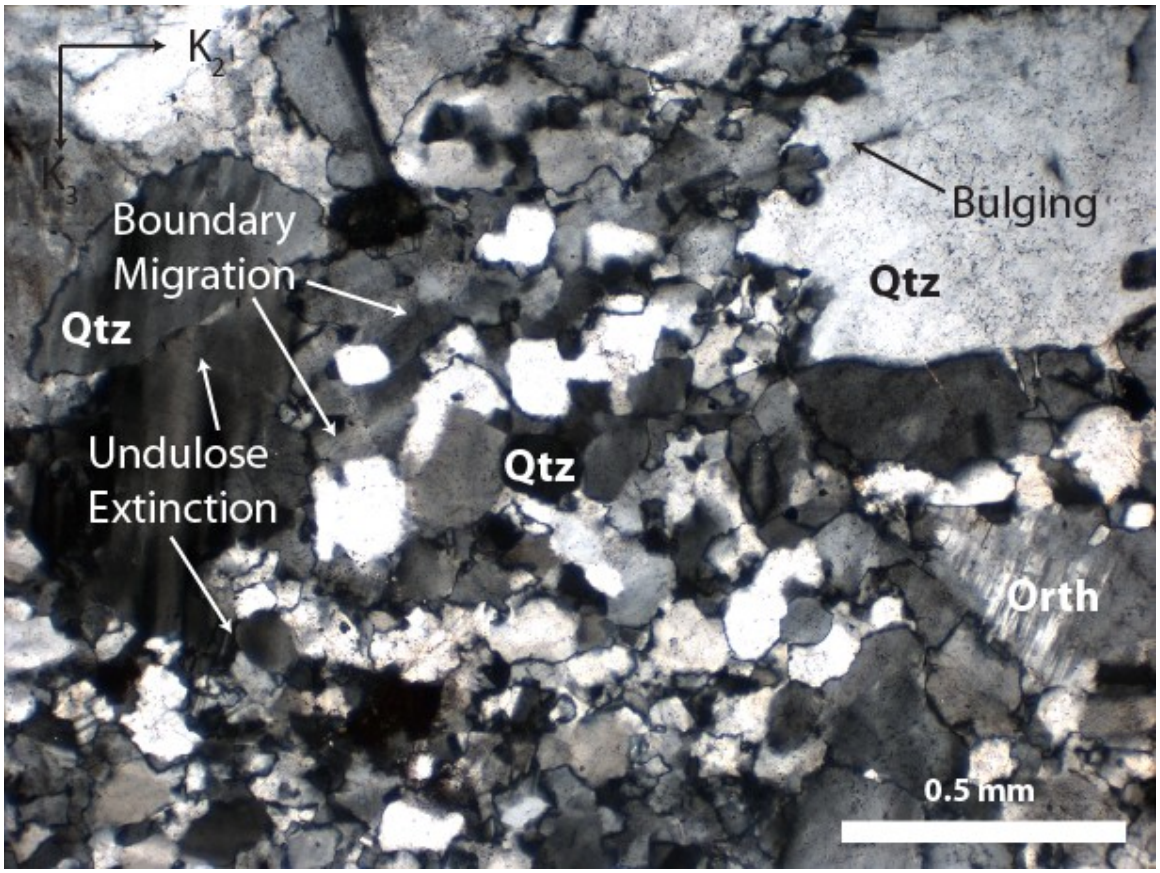

Figure 4.4.8: Late suite thin section (LB08-06B+; K_2K_3 plane, XPL) image showing undulose extinction of both large quartz grains (left) and smaller recrystallized quartz (center). The large quartz grains show intragranular fracture (left), and grain boundary bulging (right). The smaller quartz grains have been dyanamically recrystallized and are now aggregates formed from previous large quartz grains. Orth, orthoclase; Qrtz, quartz.

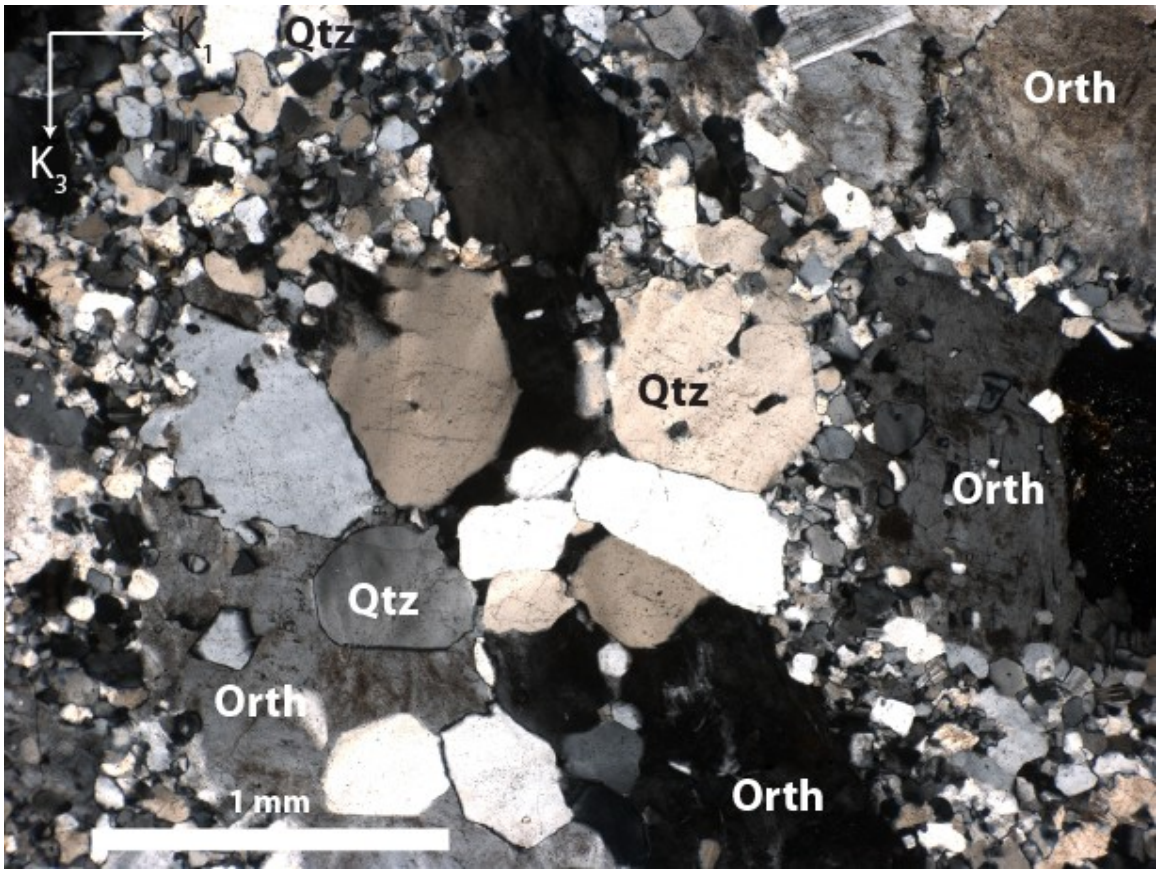

Figure 4.4.9: Late suite thin section (LB08-06B=; K_1K_3 plane, XPL) Clearly defined boundaries of quartz. Smaller recrystallized quartz seen in surrounding matrix. Orth, orthoclase; Qrtz, quartz.

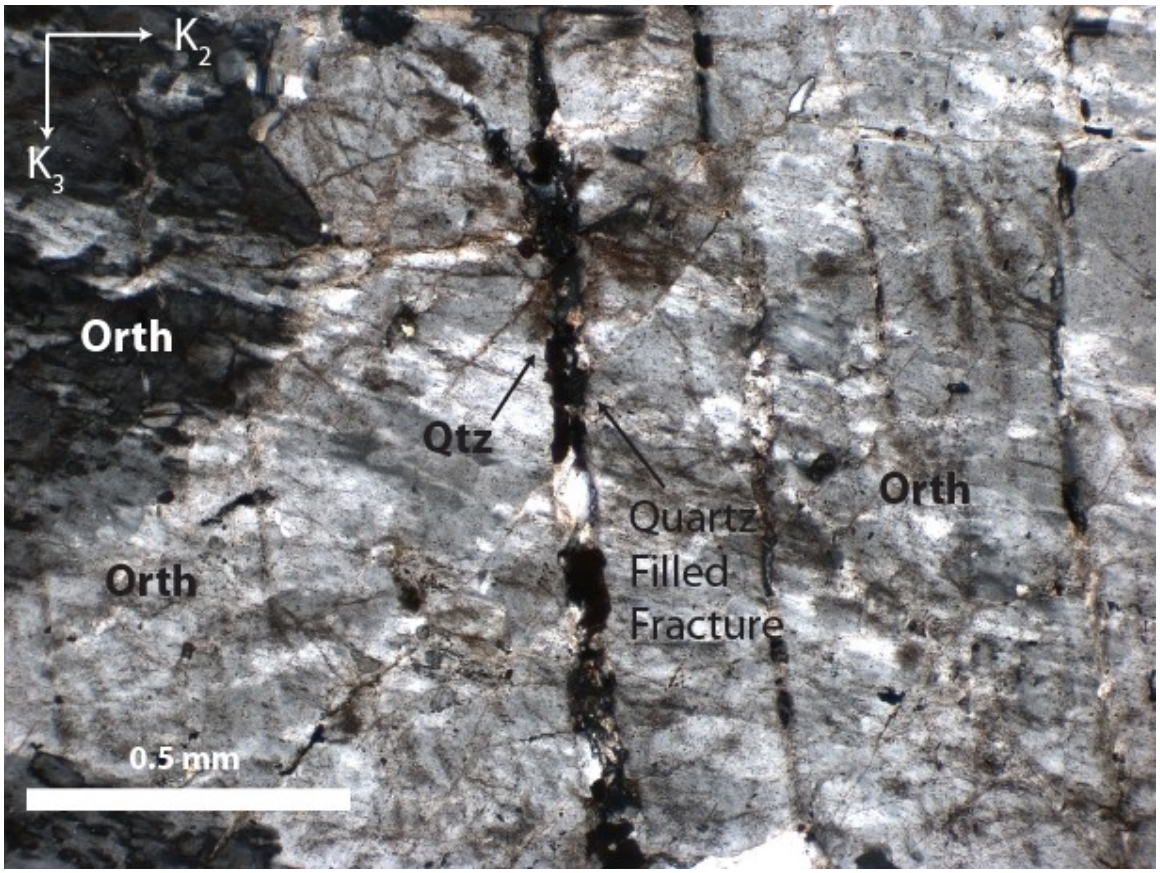

Figure 4.4.10: Late suite thin section (LB08-06B+; K_2K_3 plane, XPL) Intergranular fracture in orthoclase feldspar filled with quartz. Filled fracture is a conjugate and offseting smaller quartz filled fracture. Orth, orthoclase; Qrtz, quartz.

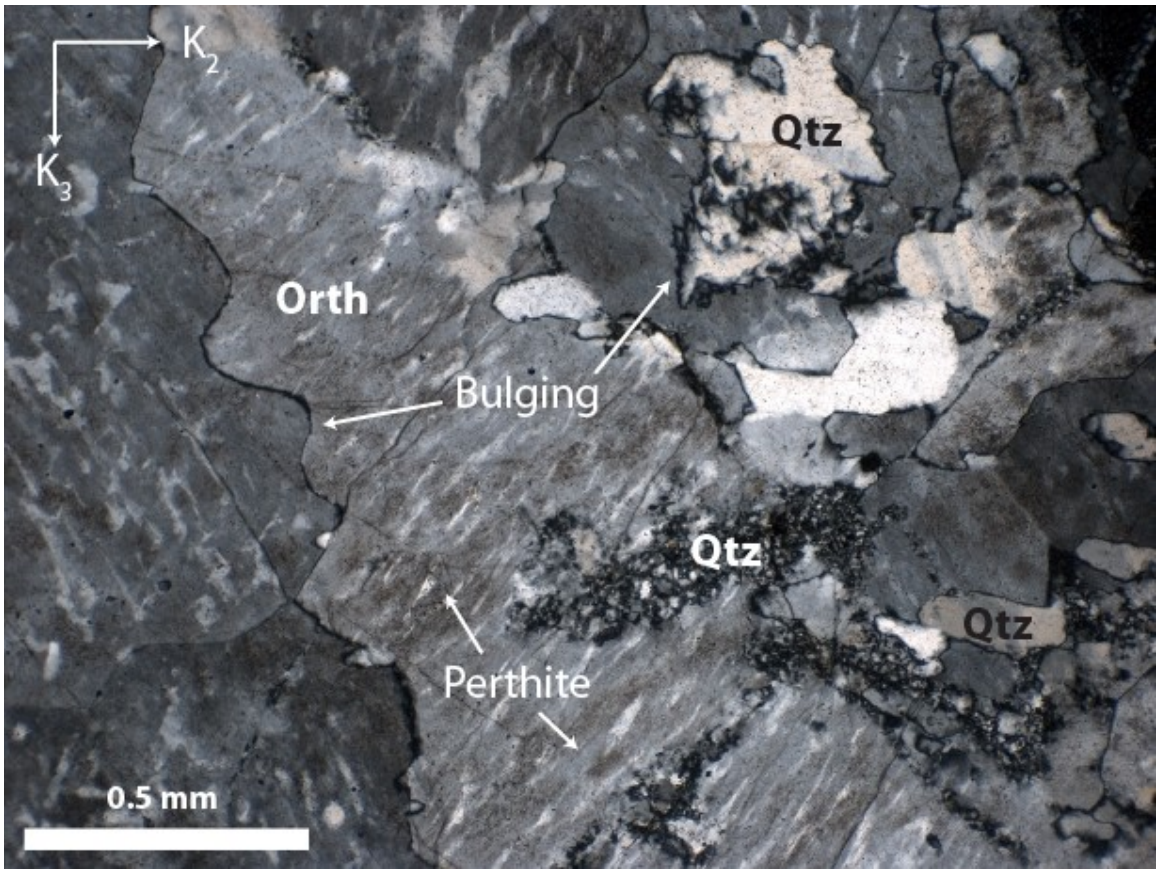

Figure 4.4.11: Late suite thin section (LB08-04B+; K_2K_3 plane, XPL) Intense grain boundary bulging seen in both quartz and orthoclase feldspar. Orthoclase also exhibits well developed perthite texture. Orth, orthoclase; Qrtz, quartz.

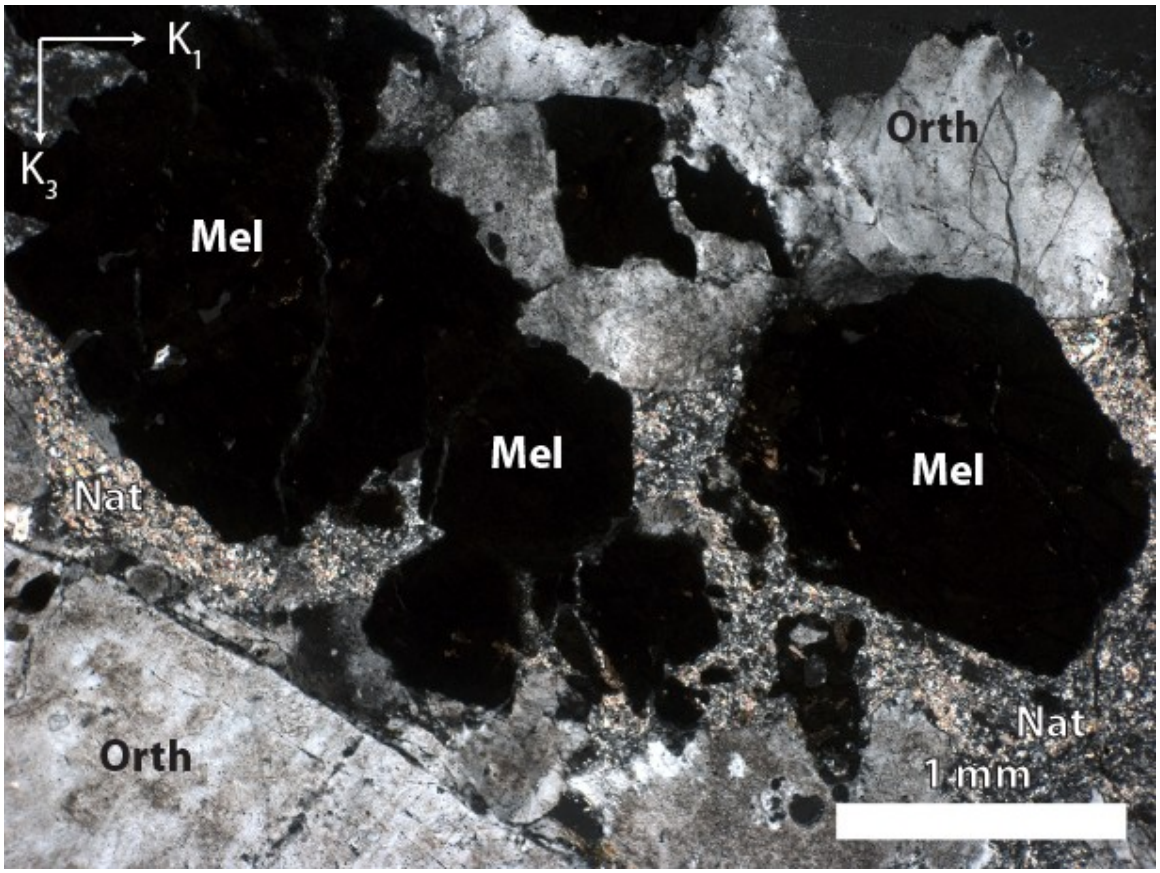

Figure 4.4.12: Early suite thin section (LB12-04C=; K_1K_3 plane, XPL) image showing the best examples seen of euhedral melanite (Mel). Fibrous natrolite (Nat) and orthoclase (Orth) in the surrounding matrix.

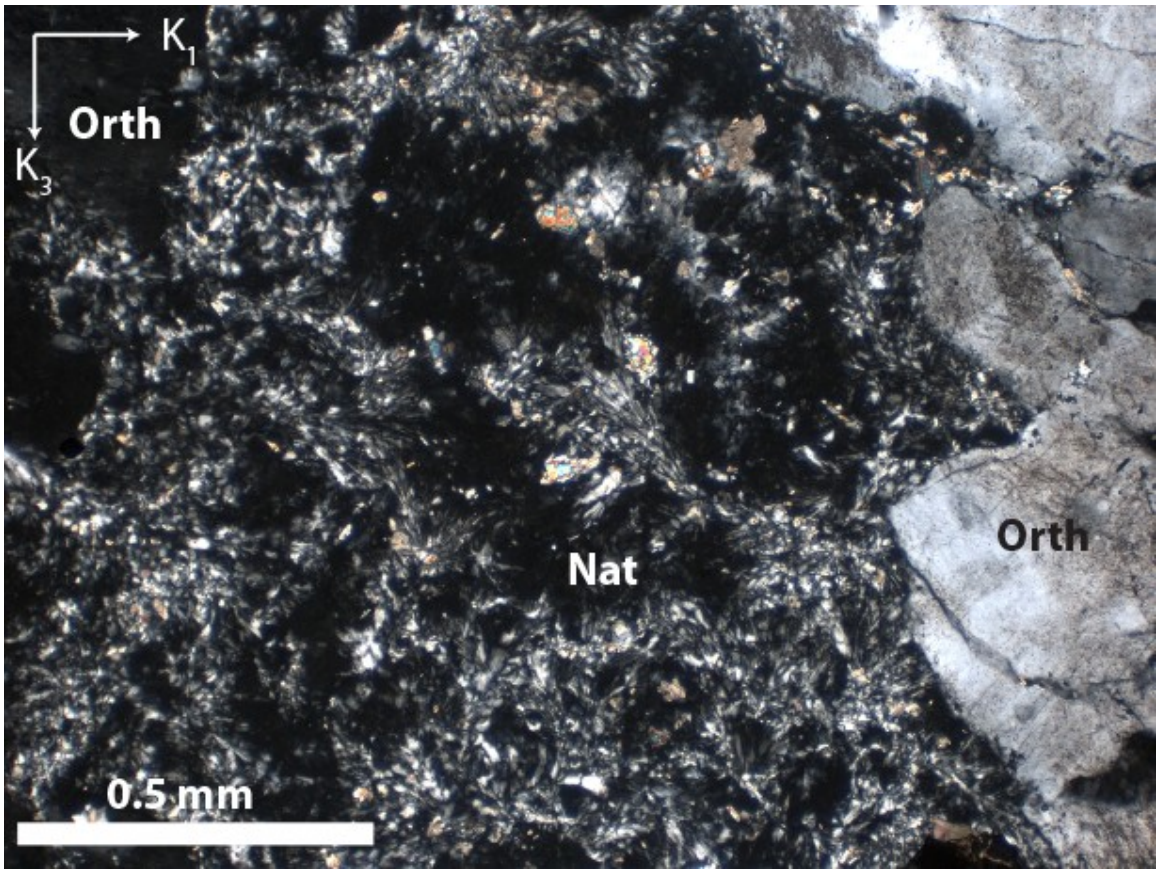

Figure 4.4.13: Early suite thin section (LB12-04C=; K_1K_3 plane, XPL) image showing fibrous natrolite (Nat) filling growing within spaces between orthoclase (Orth) grains.

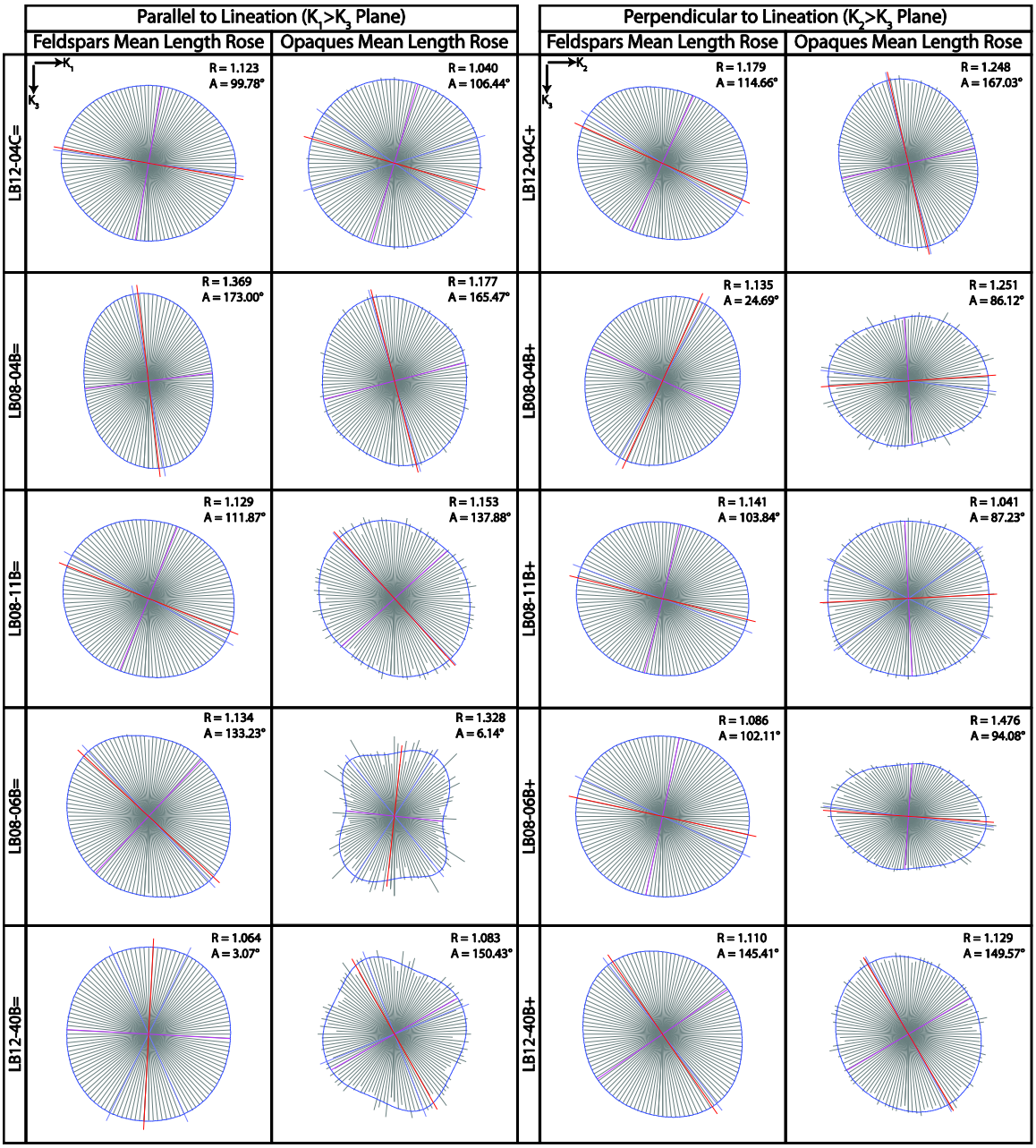

Figure 4.5.1: Mean length roses created using INTERCEPT.EXE (Launeau and Robin 1996). The "R" value represents the shape ratio or degree of anisotropy of the ellipse. The "A" value represents the mean length vector which corresponds to the orientation of the averaged long axis of the mineral. Left two columns are for the K_1K_3 plane with results from alkali feldspars (left) and opaque minerals (right). Right two columns are for the K_2K_3 plane with results from alkali feldspars (left) and opaque minerals (right). Top row (LB12-04) is early suite and four subsequent rows are from the late suite. Locations of samples are shown on Figure 3.1.1.

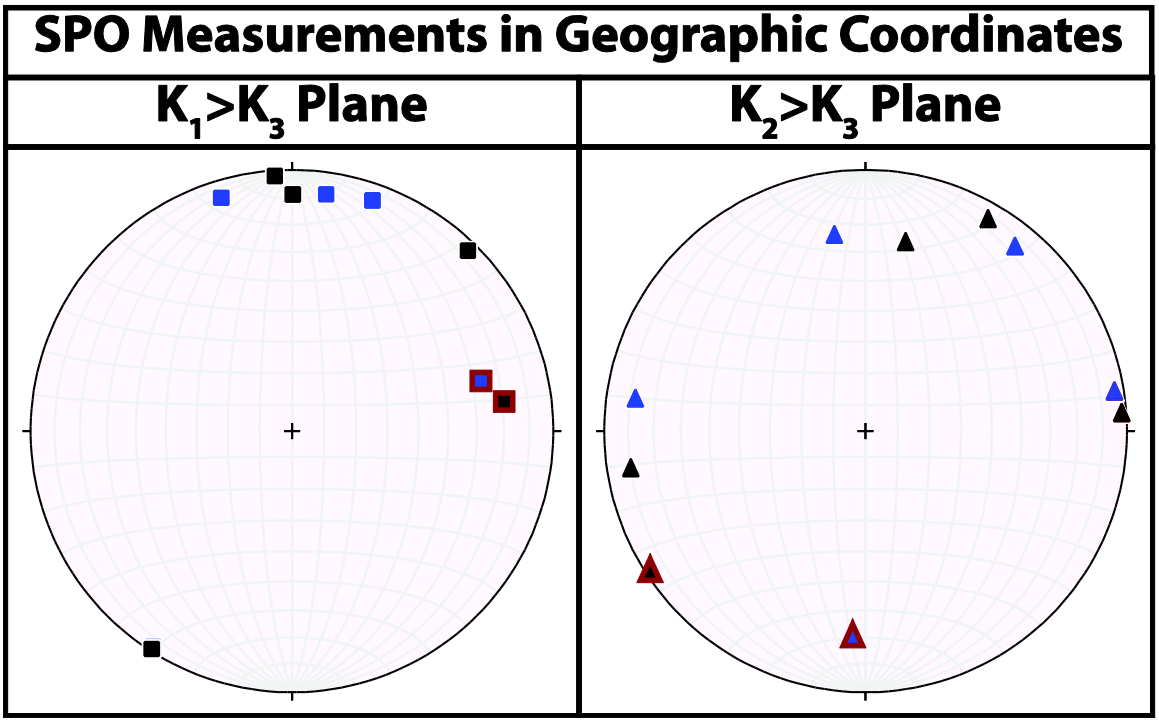

Figure 4.5.2: Equal area stereonet projections of the dominant orientations of feldspars (blue), and opaque minerals (black). The red border around symbols represents early suite measurements, and no border represents late suite measurements. Note that the planes were calculated separately for each outcrop based on the AMS measurements, so the measurements on each stereonet do not fall on a single plane.

FOLIATIONS					
Station	**Measurement**	**Ranking**	**Station**	**Measurement**	**Ranking**
LB12-01	N 29 E 86 SE	3	LB12-21	044 87 SE	3
LB12-01	N 24 E 90 SE	3	LB12-21	046 83 SE	3
LB12-02	N 11 E 75 NW	3	LB12-22	193 76 NW	1
LB12-02	N 32 E 76 NW	3	LB12-22	029 80 SE	2
LB12-03	N 36 E 84 SE	3	LB12-22	035 83 SE	2
LB12-03	N 29 E 80 SE	3	LB12-23	012 73 SE	1
LB12-04	N 50 E 24 SE	1	LB12-23	011 70 SE	1
LB12-04	N 34 E 25 SE	2	LB12-26	020 88 SE	3
LB12-04	N 8 E 34 SE	3	LB12-26	016 70 SE	3
LB12-04	N 88 W 24 SE	2	LB12-27	036 73 SE	2
LB12-04	N 22 E 36 SE	3	LB12-27	021 83 SE	2
LB12-05	N 47 W 88 NE	3	LB12-28	012 74 SE	3
LB12-05	N 12 E 85 SE	3	LB12-28	035 74 SE	3
LB12-05	N 4 E 85 SE	3	LB12-28	032 74 SE	3
LB12-05	N 3 E 86 SE	3	LB12-29	356 87 NE	2
LB12-05	N 2 E 76 SE	3	LB12-29	007 82 SE	3
LB12-06	N 57 E 75 SE	2	LB12-29	005 76 SE	2
LB12-06	N 10 E 77 NW	2	LB12-30	018 71 SE	2
LB12-06	N 10 E 79 NW	2	LB12-30	000 85 E	2
LB12-07	210 78 NW	3	LB12-30	177 59 SW	2
LB12-07	210 69 NW	3	LB12-30	167 77 SW	3
LB12-08	029 82 SE	3	LB12-30	160 83 SW	3
LB12-08	022 79 SE	2	LB12-31	045 84 SE	3
LB12-08	010 75 SE	3	LB12-31	040 76 SE	3
LB12-08M	042 74 SE	3	LB12-32	027 84 SE	3
LB12-08M	045 84 SE	3	LB12-32	046 74 SE	3
LB12-10	053 72 SE	3	LB12-32	040 86 SE	3
LB12-10	029 72 SE	2	LB12-33	039 77 SE	3
LB12-10	048 75 SE	3	LB12-33	031 77 SE	3
LB12-11	036 87 SE	3	LB12-34	021 71 SE	3
LB12-11	030 82 SE	3	LB12-34	024 82 SE	3
LB12-11	034 83 SE	3	LB12-36	226 74 NW	2
LB12-12	012 78 SE	3	LB12-37	265 76 NW	1
LB12-12	019 78 SE	3	LB12-38	215 70 NW	3
LB12-13	021 34 SE	3	LB12-38	212 81 NW	3
LB12-13	020 41 SE	3	LB12-39	267 62 NW	2
LB12-14	053 34 SE	2	LB12-40	188 74 NW	2
LB12-14	054 34 SE	3	LB12-42	051 68 SE	2
LB12-15	344 23 NE	2	LB12-43	070 75 SE	2

LB12-15	358 33 NE	3	LB12-44	224 66 NW	1
LB12-15	355 35 NE	2	LB12-46	267 82 NW	2
LB12-18	217 85 NW	3	LB12-47	218 84 NW	3
LB12-18	219 85 NW	3	LB12-47	230 83 NW	3
LB12-18	004 74 SE	3	LB12-48	181 64 NW	3
LB12-18	231 81 NW	3	LB12-48	229 72 NW	2
LB12-18	009 67 SE	3	LB12-48	155 83 SW	3
LB12-19	010 67 SE	3	LB12-48	164 75 SW	3
LB12-19	021 70 SE	3			

Table 4.1A: Field measurements of macroscopic feldspar foliations. The ranking system was used to distinguish between strong and poorly developed fabrics, 1 = poor and 3 = strong fabric. Plane measurements are presented in strike, dip format (examples: “164 75 SW” means strike = 164 and dip = 75 SW; “N 29 E 86 SE” means strike = N29E and dip = 86 SE).

LINEATIONS		
Station	**Measurement**	**Ranking**
LB12-01	22 N 27 E	2
LB12-01	10 S 37 W	1
LB12-01	14 N 35 E	2
LB12-01	43 S 7 W	2
LB12-01	34 S 22 W	2
LB12-02	18 N 59 E	1
LB12-03	5 N 40 E	2
LB12-03	4 N 34 E	3
LB12-03	7 N 15 E	1
LB12-04	19 N 65 E	3
LB12-04	19 N 76 W	3
LB12-05	39 S 19 W	3
LB12-05	22 S 7 W	2
LB12-06	26 N 57 E	3
LB12-06	7 N 10 E	2
LB12-08M	19 042	3
LB12-10	19 044	1
LB12-11	15 016	2
LB12-12	12 011	3
LB12-12	24 015	3
LB12-19	17 029	2
LB12-19	09 014	2
LB12-27	24 026	2
LB12-32	21 022	2

Table 4.1B: Field measurements of macroscopic feldspar foliations and lineations. Line measurements are presented in plunge, trend format (examples: “22 N 27 E” means plunge = 22 and trend = N27E; “09 014” means plunge = 9 and trend = 014).

SHEAR ZONE PLANES		
Station	**Measurement**	**Ranking**
LB12-04	N 59 W 39 NE	3
LB12-04	N 61 W 41 NE	2
LB12-04	N 29 W 36 NE	3
LB12-04	N 15 W 44 NE	3
LB12-04	N 12 W 66 NE	3
LB12-04	N 63 E 33 SE	3
LB12-04	N 63 E 33 SE	3
LB12-04	N 23 W 69 SE	3
LB12-04	N 19 W 29 NE	3
LB12-04	N 1 E 70 SE	3
LB12-07	089 71 SE	3
LB12-07	281 55 NE	3
LB12-07	180 75 NE	1
LB12-08	014 79 SE	3
LB12-08	N 60 E 76 SE	0
LB12-08	N 50 E 65 NW	0
LB12-08	N 43 E 57 NW	1
LB12-12	043 73 SE	3
LB12-15	004 35 SE	3
LB12-16	316 30 NE	2
LB12-16	290 40 NE	2
LB12-19	000 66 E	2
LB12-20M	325 64 NE	3
LB12-20M	330 61 NE	3
LB12-21	024 74 SE	3
LB12-23	002 59 SE	3
LB12-26	022 69 SE	3
LB12-26	014 87 SE	3
LB12-27	012 72 SE	3
LB12-33	175 85 SW	3
LB12-44	024 52 SE	3

Table 4.1C: Field measurements of shear zone planes. The ranking system was used to distinguish between strong and poorly developed fabrics, 1 = poor and 3 =strong fabric. Plane measurements are presented in strike, dip format (examples: “164 75 SW” means strike = 164 and dip = 75 SW; “N 29 E 86 SE” means strike = N29E and dip = 86 SE)..

FAULT PLANES		
Station	**Measurement**	**Ranking**
LB12-02	N 4 W 69 SW	3
LB12-36	036 56 SE	3
LB12-36	005 85 SE	3
LB12-36	053 68 SE	3
LB12-40	043 69 SE	3
LB12-40	025 60 SE	3
LB12-40	023 63 SE	3
LB12-40	022 60 SE	3
LB12-40	046 62 SE	3
LB12-40	095 62 SW	3
LB12-40	024 69 SE	3
LB12-42	017 80 SE	3
LB12-42	017 70 SE	3
LB12-42	027 78 SE	3
LB12-42	012 77 SE	3
LB12-43	072 90	3
LB12-46	085 43 SE	3
LB12-48	064 74 SE	3

Table 4.1D: Field measurements of fault planes. The ranking system was used to distinguish between strong and poorly developed fabrics, 1 = poor and 3 =strong fabric. Plane measurements are presented in strike, dip format (examples: "164 75 SW" means strike = 164 and dip = 75 SW; "N 29 E 86 SE" means strike = N29E and dip = 86 SE).

FOLD AXIAL PLANE AND LINE		
Station	**Measurement**	**Type**
LB12-05	N 46 W 82 NE	Axial Plane
LB12-05	72 S 86 E	Axial Line

Table 4.1E: Field measurements of fold axial planes and axial lines. Plane measurements are presented in strike, dip format (examples: "164 75 SW" means strike = 164 and dip = 75 SW; "N 29 E 86 SE" means strike = N29E and dip = 86 SE). Line measurements are presented in plunge, trend format (examples: "22 N 27 E" means plunge = 22 and trend = N27E; "09 014" means plunge = 9 and trend = 014).

EARLY SUITE

Station	# of Cores	K_m AVG	K_m STDev ±	L AVG	L STDev ±	F AVG	F STDev ±	P_j AVG	P_j STDev ±	T AVG	T STDev ±
SE		**(SI x 10^{-6})**									
LB08-03B	2	878.344	107.089	1.010	0.004	1.010	0.006	1.019	0.003	-0.028	0.504
LB12-04C	2	16267.020	7493.154	1.016	0.008	1.072	0.008	1.089	0.016	0.653	0.113
E											
LB12-14B	3	653.926	64.399	1.004	0.001	1.003	0.002	1.007	0.003	-0.263	0.329
LB12-15A	5	11809.052	9518.819	1.067	0.019	1.057	0.017	1.128	0.038	-0.078	0.030
LB12-16A	4	52317.903	41089.647	1.044	0.010	1.075	0.033	1.122	0.037	0.212	0.210
W											
LB12-17B	2	68297.515	31663.485	1.017	0.011	1.111	0.038	1.131	0.052	0.737	0.086

Mean		25037.293		1.026		1.055		1.083		0.206	
Median		14038.036		1.016		1.065		1.105		0.092	
Min		653.926		1.004		1.003		1.007		-0.263	
Max		68297.515		1.067		1.111		1.131		0.737	

Table 4.2A: Site averaged early suite AMS results. STDev, standard deviation; AVG, Average; K_m, mean bulk susceptibility; $L = K_1/K_2$; $F = K_2/K_3$; Pj, anisotropy magnitude; T, anisotropy shape where T<0 is prolate and T>0 is oblate.

LATE SUITE

Station	# of Cores	K_m AVG	K_m STDev ±	L AVG	L STDev ±	F AVG	F STDev ±	P_j AVG	P_j STDev ±	T AVG	T STDev ±
SE		**(SI x 10^{-6})**									
LB08-04B	1	13801.400	-	1.038	-	1.055	-	1.095	-	0.185	-
LB12-05A	4	753.732	85.174	1.006	0.004	1.016	0.014	1.023	0.017	0.499	0.425
LB12-12A	3	8047.034	3142.647	1.056	0.018	1.104	0.015	1.169	0.015	0.292	0.191
LB12-21A	2	4804.542	1266.039	1.047	0.006	1.022	0.002	1.072	0.005	-0.354	0.099

LB12-22B	3	14108.583	1350.154	1.038	0.019	1.014	0.012	1.056	0.013	-0.442	0.492
Central											
LB08-05A	2	13631.243	2126.607	1.012	0.001	1.013	0.005	1.025	0.004	-0.010	0.220
LB08-06B	2	253.105	46.826	1.010	0.003	1.056	0.017	1.073	0.022	0.683	0.001
LB08-08A	2	8210.637	8621.107	1.044	0.030	1.061	0.042	1.111	0.016	0.125	0.662
LB08-10A	6	9363.029	1594.453	1.029	0.006	1.046	0.011	1.077	0.017	0.225	0.095
LB08-11A	3	14872.777	1686.432	1.028	0.009	1.067	0.005	1.100	0.008	0.410	0.141
LB12-03A	3	11433.970	2436.498	1.040	0.017	1.052	0.039	1.097	0.030	0.036	0.502
LB12-11A	1	446.528	-	1.034	-	1.009	-	1.045	-	-0.583	-
NW											
LB08-07A	2	588.649	222.990	1.026	0.006	1.019	0.001	1.046	0.008	-0.146	0.064
LB12-37A	1	2158.562	-	1.035	-	1.032	-	1.068	-	-0.042	-
LB12-40B	2	1413.261	273.686	1.019	0.007	1.093	0.015	1.122	0.012	0.639	0.153
NE											
LB12-26A	2	2766.867	781.229	1.022	0.005	1.040	0.013	1.063	0.011	0.279	0.260
LB12-27B	2	389.780	18.149	1.013	0.003	1.026	0.009	1.040	0.008	0.302	0.265
LB12-28B	3	5393.207	585.454	1.008	0.006	1.007	0.004	1.016	0.002	-0.026	0.600
LB12-30A	5	15124.738	4516.088	1.043	0.013	1.055	0.040	1.104	0.039	-0.003	0.492

Mean	6713.771	1.029	1.041	1.074	0.109
Median	5393.207	1.029	1.040	1.072	0.125
Min	253.105	1.006	1.007	1.016	-0.583
Max	15124.738	1.056	1.104	1.169	0.683

Table 4.2B: Site averaged AMS results. STDev, standard deviation; AVG, Average; K_m, mean bulk susceptibility; $L = K_1/K_2$; $F = K_2/K_3$; Pj, anisotropy magnitude; T, anisotropy shape where $T<0$ is prolate and $T>0$ is oblate.

5. Discussion

5.1 Anisotropy of Magnetic Susceptibility (AMS)

Because titanomagnetite is believed to be the dominant carrier of the magnetic signal (Figure 4.2.2 and 4.2.3) and only pseudosingle (PSD) and multidomain (MD) varieties exist in any of the samples (Figure 4.2.1), an inverse magnetic fabric caused by single domain (SD) magnetite can be ruled out. There are some localized paramagnetic readings (Appendix A), primarily in the early suite, caused by biotite. However, the strong magnetic field of titanomagnetite will dominate the weak field of biotite. Even if biotite is locally controlling the magnetic field, the AMS measurements will still reflect the mineral shape fabric. This simple mineralogy allows for very straightforward interpretations of the AMS data; I interpret the principal axes of AMS to coincide with the principal strain orientations.

Scalar AMS parameters were plotted separately for the early and late suites for comparison, and to observe any relationships between: P_j and K_m, T_j and K_m, and T_j and P_j (Figure 5.1.1). In the early suite, low K_m values tend to correspond with neutral P_j values ($P_j = 1$; Figure 5.1.1A). The most intense prolate fabrics are also only seen at low K_m and low P_j values (Figure 5.1.1B, C). In the late suite, there is a large variation between all three parameters, with a slight tendency of samples with the highest anisotropy to have oblate shapes (Figure 5.1.1F). When comparing the two suites to one another, the early suite is dominated by oblate shapes whereas the late suite has a mix of both oblate and prolate shapes (Figures 5.1.1B, C, E, F).

The lack of strong correlation between K_m and either P_j or T indicates that there is no obvious relationship between mineralogy and degree or shape of anisotropy. The difference between oblate versus prolate fabrics between the two suites likely indicates that deformation varied throughout the pluton over time and/or space.

The magnetic foliation dominates (F > L) in both the early and late suites (Table 4.2), and coincides well with the macroscopic foliations of aligned feldspar grains measured in the field. The orientation of the AMS foliations and dominance of F > L fabrics are consistent with the tectonic strain within the region. Therefore, the AMS foliations in the pluton were likely caused by motion associated with the regional thrusts.

5.2 Fabric Orientations: Relationships Between Field Measurements, AMS Analysis and SPO Analysis

Generally AMS measurements parallel field measurements, and are likely formed from motion along neighboring thrusts. The apparent lack of fabric seen upon initial thin section inspection could be due to the large average grain size causing fabrics to only be seen in scales larger than thin section. This is likely the cause for weak relationships seen between AMS and field measurements to SPO mean length vectors. Additionally, because the fabrics are weak, they are not easily identified by visual inspection and would only be reliably evident by SPO analysis if thousands of grains were available for the analysis.

Early Suite Foliations

The mean AMS foliation orientation in the early suite parallels the macroscopic field measurements (Figure 4.1.1). Site specific plots also show an agreement between

field and AMS foliation planes (4.3.1), with a gently dipping NE-SW striking foliation common in active thrust fault regimes. SPO measurements of the K_1K_3 plane show feldspar and opaque mineral fabric in parallel (Figure 4.5.1). However, on the K_2K_3 plane, feldspar and opaque fabrics are shifted ~50° from each other.

The consistency between the AMS and field measurements, and parallelism to regional thrust strike is evidence that the foliations are tectonically derived. The causes for some inconsistencies between the SPO long axis directions could be due to the very large average grain size seen in the early suite. The large average grain size reduces the reliability of the mean length rose ellipse calculation. In the early suite SPO calculations, typically <30 feldspar grains, and <20 opaque minerals were analyzed. Typically SPO analyses use hundreds to thousands of grains (e.g. Hastie et al. 2010, Izquierdo-Llavall et al. 2012).

Late Suite Foliations

The majority of the AMS foliations strike in a NE-SW orientation, which is consistent with the macroscopic field foliations (Figure 4.1.1). Late suite AMS mean foliation orientation dips steeply, whereas the field foliations are shallow (Figure 4.1.1). When comparing the field and AMS measurements within each sample site, K_3 orientations rarely overlap macroscopic field foliation pole measurements, and commonly have much steeper dips. Magnetic foliations in the late suite sweep in a 'girdled' pattern across the stereonet (Figure 4.1.1). The girdle pattern and variations in dip degrees are likely due to the presence of a composite magnetic fabric (Housen et al 1993; Figure 5.1.2). Composite fabrics occur when magnetic minerals' long axes are parallel, but their

short axes vary in multiple directions causing the K_3 susceptibility axis to be the vector sum of the combined K_3 orientations. (Housen et al. 1993). Further supporting the composite fabric is the prevalence of both prolate and oblate mineral grain shapes (Figure 5.1.1; Housen et al. 1993). Late suite SPO feldspar and opaque mean length vectors are typically parallel within each plane (Figure 4.5.1). Similar to early suite SPO, mean length vectors rarely parallel the long axes of magnetic susceptibility (K_1 and K_2).

Based on the majority of AMS foliations striking NE-SW parallel to field measurements, and the likelihood of a composite fabric, the AMS foliations of the late suite are presumed to be tectonically derived from tectonic motion along adjacent thrusts. Field measurements are likely representing finite strain, but due to the composite fabric seen in the AMS measurements strain is likely being partitioned, or represented as combinations of flattening with fault strike parallel extension and simple shear due to thrusting. Some of the differing SPO mean lengths in the late suite may also be attributed to the varying orientations of the magnetic minerals caused by the composite fabric (see Figure 4.3.4).

Early Suite Lineations

AMS lineations in the early suite generally plunge shallowly to the southeast (Figure 4.1.1). The orientation of the early suite lineations corroborate with simple shear strain common in thrust geometries. In simple shear, the long axis of the finite strain ellipsoid (coincident with the lineation) is contained within the shear plane. In a thrust fault, the shear plane is perpendicular to the fault and contains the fault slip direction. At the onset of deformation, the lineation is oriented at 45° angle from the fault and rotates

into parallelism with the fault motion with increasing strain. In a major thrust fault like the Moine or its associated faults, the offset on the fault is great enough so that the lineation should be parallel to the transport direction (e.g. Leslie et al. 2010). Macroscopic lineations were scarce in the early suite, so AMS lineations are compared to measurements of the long axes of internal pseudoleucite aggregates made by Searle et al. (2010) in the Aultivullin quarry (stations LB08-03 and LB12-04), which should correspond with the long axis of the finite strain ellipsoid (Figure 4.1.1). Both feldspar and opaque mean length vector are subparallel to K_1 orientation in SPO analyses (Figure 4.5.1).

AMS lineations parallel the field lineation measurements made by Searle et al. (2010). Both measurements parallel the inferred fault transport direction, which have been interpreted to be products of simple shear caused by regional thrust faults because they are parallel to the inferred fault transport direction (Figure 4.1.1).

Late Suite Lineations

The majority of late suite field lineations and AMS mean K_1 orientations plunge shallowly to either the southwest or northeast sub-parallel to thrust strike. However, some AMS lineations are contained within the approximate shear plane of the thrust faults, and within the foliation plane. Interestingly, neither feldspar nor opaque SPO mean vector lengths show much agreement with K_1 orientations. The weak SPO fabrics are likely due to the large average grain size causing a small number of actual grains analyzed.

The first set of AMS and field lineations plunge NE and SW and suggest thrust strike parallel extension (Figure 4.1.1; e.g. Ellis & Watkinson 1987; Weiler & Coe 1997;

Mookerjee and Mitra 2009). These lineations are not perfectly horizontal, and this is likely due to deformational overprinting from the thrust fault strain. Alternatively, it could be due to oblique extrusion, which has been described in other contractional orogens (Fernández et al. 2013). The second set of lineations detected through AMS contains measurements with various plunges within the shear plane. The lineations that parallel thrust transport direction are dominated by simple shear strain associated with thrusting, and the range of orientations could be related to various degrees of simple shear strain. Alternatively, the lineations within the shear plane could vary in orientation due to the hypothesized curve of the overlying Ben More thrust fault (Figure 1.4.2), which significantly shifts the transport direction.

The two sets of lineations within the pluton are particularly interesting. The pluton could be partitioned so that some sites have primarily thrust signatures, and others primarily lateral extrusion signatures. Another very likely possibility is that many sites have a combination of both thrust and lateral extrusion signatures.

Outcrop Scale Brittle Faults and Shear Zones

The presence of ductile shear zones and brittle faulting in outcrop scale suggests that there was a considerable amount of deformation in both the early and late suites (Figure 4.1.2) and that deformation took place when the pluton was at a range of temperatures during its cooling. However, it is difficult to relate them to kinematics determined from other evidence.

The early suite shows no signs of brittle faults at outcrop scale, further supporting microstructural evidence of dominantly ductile deformation. Shear zones present in the

early suite indicate that significant ductile deformation occurred, however the orientations of shear planes do not correspond well with field and AMS evidence for thrust fault deformation. Shear zones with reverse motion only crudely match predictions for thrust faulting, and do not fit well within the context of flattening of the thrust sheet. The presence of shear zones with normal sense of motion is not expected within a thrust fault, and do not correspond with the hypothesized curve of the Ben More thrust.

The late suite has both outcrop scale shear zones and brittle faults (Figure 4.1.2). Brittle faults are only seen in the NW extent of the pluton, and shear zones are generally only seen in the SE, NE, and west central margins. This spatial variation suggests that the late suite experienced primarily ductile/solidified deformation nearest the Ben More thrust plane, and brittle deformation in the further NW margin. Because the shear zones within the late suite were measured along horizontal (map view) two-dimensional planes, dip angles were difficult to measurement. They have a high variance in orientation with generally steep dip, and do not fit easily into a thrust fault context. It is possible that they may be oblique slip shear zones, but due to the limited two-dimensional view only the strike-slip component of motion is present. Regional evidence for thrust faults truncating folds within their footwalls and later extensional normal faulting overprinting earlier thrusting suggests some out-of-sequence and synchronous motion occurred along the Moine, Ben More, and Sole Thrusts (Searle et al. 2010), which could likely cause shear zones and faults to exhibit oblique orientations and alternating senses of motion. Further work is necessary to relate these to field and AMS measurements.

5.3 Petrographic Microstructures, Emplacement and Deformation Conditions, and Deformation Mechanisms

The thin sections show evidence for deformation occurring under varying temperature regimes, starting with relatively high temperatures (>600°C) and stresses required for dislocation creep in feldspars, and decreasing to low temperatures for recrystallization of quartz (200-300°C; Passchier and Trouw 2005). Feldspar and quartz are the only two minerals with well developed microstructures to be used as evidence, primarily due to the high relative abundance and large grain sizes compared to other minerals.

Deformation Mechanisms in Feldspar

Evidence for crystal plastic deformation in feldspars such as undulose extinction is found in all thin sections (Figure 4.4.6). Bulged and migrated feldspar grain boundaries, formed by recovery mechanisms for dislocation creep, are also seen throughout (Figure 4.4.1 and 4.4.2). In all thin sections a pervasive perthite texture in orthoclase, and occasional myrmekite texture in plagioclase is present. Perthite and myrmekite textures are symplectites that have been shown to grown simultaneously with crystal plastic deformation in a solid-state reaction (Simpson and Wintsch 1989; Vernon 2004; Passchier and Trouw 2005). Feldspars can also be observed bent and kinked, a sign of dislocation creep (Vernon 2004; Passchier and Trouw 2005; Figure 4.4.3).

Feldspars show signs of brittle deformation with pervasive intergranular microfractures, and microfaults throughout the entire extent of the pluton. Interestingly, thin sections with the highest abundance of microfractures also have the evidence for the

highest temperature regimes indicated by abundant perthite and myrmekite. Microfracturing is particularly prevalent in the early suite, and southwest portion of the late suite. Because brittle microstructures typically only occur in low temperature or under fast strain rate conditions, this relationship suggests that the microfracturing occurred once the pluton was very cool, or strain rates were very high (Vernon 2004, Passchier and Trouw 2005). Evidence for frictional grain-boundary processes can occasionally be seen in the form of intragranular microfaults (Figure 4.4.2). Like the microfractures, microfaulting is more abundant in the early suite and southwestern locations.

Deformation Mechanisms in Quartz

Quartz also displayed strong evidence for crystal plastic deformation including recrystallization, grain boundary bulging, and undulose extinction. The recrystallized quartz grains, a product of recovery via grain boundary migration, are interpreted to have formed via dynamic as opposed to static recrystallization. Dynamic recrystallization is generally regarded as syndeformational and static as postdeformational. The recrystallized quartz aggregates exhibit undulose extinction. Therefore, the grains were first recrystallized and then further deformed to form the undulose extinction, which strongly supports dynamic recrystallization. Primary non recrystallized quartz grains display both undulose extinction and grain boundary bulging, another recovery product produced by grain boundary migration.

Quartz showed some evidence for brittle deformation with intragranular microfractures. More commonly, quartz fills fractures. The quartz filled fractures suggest

that the pluton also had fluids interacting with it which could lower the temperatures required for dislocation creep to be active. There is a greater population of microfractures in the SE corner of the pluton possibly suggesting that is nearer to the Ben More thrust fault and later brittle deformation was more localized near the fault. The greater presence of microfractures is associated with more widespread and intense perthite development.

Some fracture sets display 60-120° cleavage, with σ_1 parallel to K_1 and normal to the obtuse angle and σ_3 parallel with K_3 and normal to the acute angle. The parallelism of finite strain axes as determined by AMS principal susceptibilities and late stage stress axes determined from these microfractures suggests that accumulated strain was largely coaxial.

Smaller thin, straight quartz-free fractures can be seen in tandem with quartz filled fractures, suggesting that there were possibly two stages of fracturing. The quartz-filled fractures that occurred during the bulk of the deformation shortly after cooling, and the quartz-free fractures formed in a second stage that may have been much later after the pluton was already cooled.

Deformation Conditions of Feldspars

Petrographic evidence allows some constraints on deformation conditions, particularly temperature. Microstructures suggest deformation took place from high temperature (>600°C) to low temperature conditions (200-300°C; Passchier and Trouw 2005).

Deformation during high temperature conditions was responsible for processes including perthite and myrmekite exsolution, and grain boundary migration resulting in

bulged grain boundaries. The presence of bulged grain boundaries in alkali feldspars forms under high grade deformation temperatures >600°C (Passchier and Rudolph 2005). The presence of perthite within the feldspars is evidence that deformation occurred at medium high temperatures 500-600°C, right around the magmatic to solid state transition, (Simpson and Wintsch 1989; Pryer 1993). The perthite exsolution lamellae occur at the mineral's solvus temperature. For a given mineral composition, the solvus temperature is the point where a homogeneous mixture in solid solution begins to break down (unmixes, exolves) into two minerals (Vernon 2004). The approximate solvus temperature for intermediate feldspars is relatively high, ~600°C (Smith and MacKenzie 1958; Tullis and Yund 1979).

The patchy undulose extinction seen in the feldspars is common in low-medium grade temperatures (Pryer 1993; Passchier and Trouw 2005). The 'bent' or 'kinked' feldspars require low-medium to medium-grade conditions (<500°C) for dislocation creep to occur (Passchier and Rudolph 2005).

Fracturing occurred within feldspars at even lower temperatures, <300°C. The feldspar microstructures confirm that the pluton was being deformed while it was still at a relatively hot temperature, and then continued to deform into the solid state at lower temperatures.

Deformation Conditions of Quartz

Quartz also shows a range in deformation condition temperatures from high (~600°C), to low (200-300°C). The recrystallized quartz grains exhibit grain boundary bulging, which is evidence for medium-high to high temperature conditions. Quartz

experiences grain boundary migration recrystallization under high temperature conditions between 500-700°C (Passchier and Trouw 2005). Undulose extinction and dynamic recrystallization typically occur in low to medium grade conditions between 400-500°C (Passchier and Trouw 2005). The intragranular fractures are evidence for very low-grade conditions <300°C (Passchier and Trouw 2005).

5.4 Relationship Between Emplacement and Deformation of Loch Borralan Pluton and Thrusting

Based on the lack of preserved magmatic fabric and high temperature microstructures present, the pluton was likely being deformed by movements associated with one or multiple regional thrust faults (eg. Moine, Ben More, Borralan, Sole, etc.) from early emplacement to post cooling. Movements along the Moine Thrust calculated from Rb-Sr isotopic ages of synkinematic white micas in Moine mylonites constrain the age of ductile movements to be between 437-408 Ma (Freeman et al. 1998). Unfortunately, evidence to precisely constrain deformation on the other faults is lacking, but the order of thrusting gives relative ages of deformation of the Ben More and Sole thrusts to postdate movements along the Moine Thrust. Even if the majority of deformation on the Moine Thrust ended around 430 Ma, as Freeman et al. (1998) suggests, the pluton's crystallization age calculated from U-Pb isotope dating is approximately 430 Ma (early suite 431 Ma, late suite 429.2 Ma; Goodenough et al. 2011) so the pluton was being deformed during the entire ascent and likely after cooling. This overlap in ages is further evidence suggesting that the pluton began its ascent during the majority of thrusting, deforming from initial ascent into crystallization.

The early suite crystallized before the estimated major cease in deformation around 430 Ma, and based on the high temperature microstructures is interpreted as syn-kinematic. The syn-tectonic emplacement timing is likely the cause for the strong thrust deformation signature seen in the AMS results. The late suite has fabrics that formed primarily during low strain, when strike parallel extrusion caused by the Moine Thrust capping or "roofing" forced the magma to follow the path of least resistance, laterally along the thrust planes. The variation in lineation and foliation AMS patterns seen in the late suite, and the composite fabric could be due to the magma being forced along these thrust planes (strike parallel extrusion) while simultaneously being slowly deformed by the final slight movements of the Moine Thrust Fault or other related thrust faults.

The neighboring Loch Ailsh pluton northeast of the Loch Borralan pluton has a similar crystallization age of 430.6 ± 0.3 Ma (Goodenough et al. 2011). The Loch Ailsh pluton lies directly below the Moine Thrust, and intrudes the Ben More Thrust sheet. Similar to the Loch Borralan pluton, Loch Ailsh has localized shear zones related to thrusting, with recrystallization of large perthitic feldspars to fine-grained albite-rich aggregates (Parsons 1965). With the similar crystallization age, and presence of high temperature microstructures, I would expect the Ailsh pluton to exhibit similar foliation and lineations of the Loch Borralan late suite. Further research is needed to test this hypothesis.

Plutons have been well documented to commonly intrude during the last stages of deformation in contractional orogens (Pitcher 1993 and Brown 1994). These syn-orogenic plutons are coined "stitching" plutons. The "space problem" of plutons is an ongoing debate regarding how plutons make room for themselves within shortening

terranes (e.g. Hutton et al. 1990, Cruden 1998, Fernández & Castro 1999). One possible solution to this "space problem" is thrust parallel extension.

Other studies of thrust faults found evidence for strike parallel lateral extrusion (e.g. Brun et al. 1985; Weiler and Coe 1997; Yang and Liu 2009) based, in part on sub-horizontal stretching lineations parallel to fault strike. Brun et al. (1985) studied stretching lineations within the Main Central Sheet, a thrust and fold belt in the Himalayas of China. They found that stretching lineations parallel thrust transport direction in the lower parts of the sheet, but vary between transport parallel and strike parallel orientations in the upper sheet. These lineations indicate multiple shear components, one subparallel to and one at a high angle to the Himalayan belt. The relationship seen in Brun et al. (1985) between depth, proximity to thrust, and lineation orientation is similar to what is seen in the Loch Borralan Pluton. Wieler and Coe (1997) used paleomagnetic AMS orientations within syn collisional quaternary fluvial sediments formed within a fold and thrust belt in the Erap Valley, northern Papau New Guinea. They concluded that the sediments within this particular unit expressed low angle K_{max} values (lineation) perpendicular to thrust transport direction, parallel to strike, which likely is a result of strike-parallel extension. Yang and Liu (2009) also studied crustal thickening in the Himalayas using a 3D model approximating the Asian continent as a power-law viscous plate indented by a stiff Indian plate. They found that early stages of collision were dominated by crustal thickening (lineations parallel thrust transport direction), but as deformation progressed, lateral extrusion began to dominate. Yang and Liu (2009) even calculated that during present day movements, a small percentage of the land mass once accumulated via crustal thickening is now being lost to lateral extrusion.

The findings of Yang and Liu (2009) substantiate findings within the Loch Borralan pluton where the early suite shows a strong thrusting simple shear fabric (crustal thickening), and the late suite is dominated by fault strike parallel extrusion. Fault parallel extension in contractional orogens may not be uncommon. Much like the models developed for the Assynt region by Peach and Horne (1914), thrust belt models used today are largely two-dimensional in nature (e.g. the classic paper by Boyer and Elliot 1982, which is still largely used today), but further research investigating the presence of deformation along strike could help expand these models to three-dimensions.

Searle et al. (2010) hypothesizes that the Loch Borralan pluton is underlain by a newly proposed thrust, the Borralan Thrust. This interpretation places the Loch Borralan pluton within its own thrust sheet. This is a likely interpretation because of the presence of contact metamorphosed Cambro-Ordovician country rock sitting structurally above lower Sole thrust imbricates in the northwest. Therefore, the Loch Borralan pluton is likely bounded by the Borralan and Ben More thrusts. This project shows little evidence for either the existence or non-existance of the Borralan Thrust. Fabric signatures of the proposed Borralan thrust fault should be largely coincident with the other well-established thrust faults, so attributing particular deformation fabrics to one fault versus another is challenging. Because the lower contact of the Borralan Pluton is not exposed, Borralan Thrust related strain may not be present in the exposed upper portions of the pluton which are nearer to the Ben More thrust plane. The locations nearest the Ben More thrust plane, specifically in the southeastern extent of the pluton show the highest degree of deformation indicated by pervasive fracturing, and perthite growth. These intense deformation features gradually decrease SE to NW following thrust motion, but are never

totally absent. The moderately steep dipping foliations in the early suite and shallowly plunging thrust transport parallel lineations are consistent with a simple shear thrust model, likely caused by Ben More and/or Moine thrusts. The complex fabrics seen in the late suite of localized zones of both simple shear fabric components, and the dominant fabric, strike parallel extrusion fabric components (Figure 5.4.1) could be result of some 'out-of-sequence' thrusting. It is possible that there were multiple stages of movements along each thrust, and that each thrust sheet moved independently and synchronously causing strain partitioning, overprinting, and composite fabrics.

The Ben More thrust curves above the Loch Borralan pluton, and then dips down NW of the pluton to form the Cam Loch Klippe where Archean gneiss overlies Cambro-Ordovician sedimentary country rock (Figure 1.4.2). As the Ben More thrust flattens over the top of the pluton, foliations should become shallower and thrust-related lineations should rotate towards horizontal. As the thrust dips back down, foliations may dip shallowly to the NW and thrust related lineations should begin to plunge NW. This curve in the thrust could also explain some of the fabric orientation variation, especially for AMS lineations within the thrust shear plane. However, field evidence does not display these lineation orientations, which suggests that the AMS fabrics seen in the pluton are likely recording a combination of kinematic signatures.

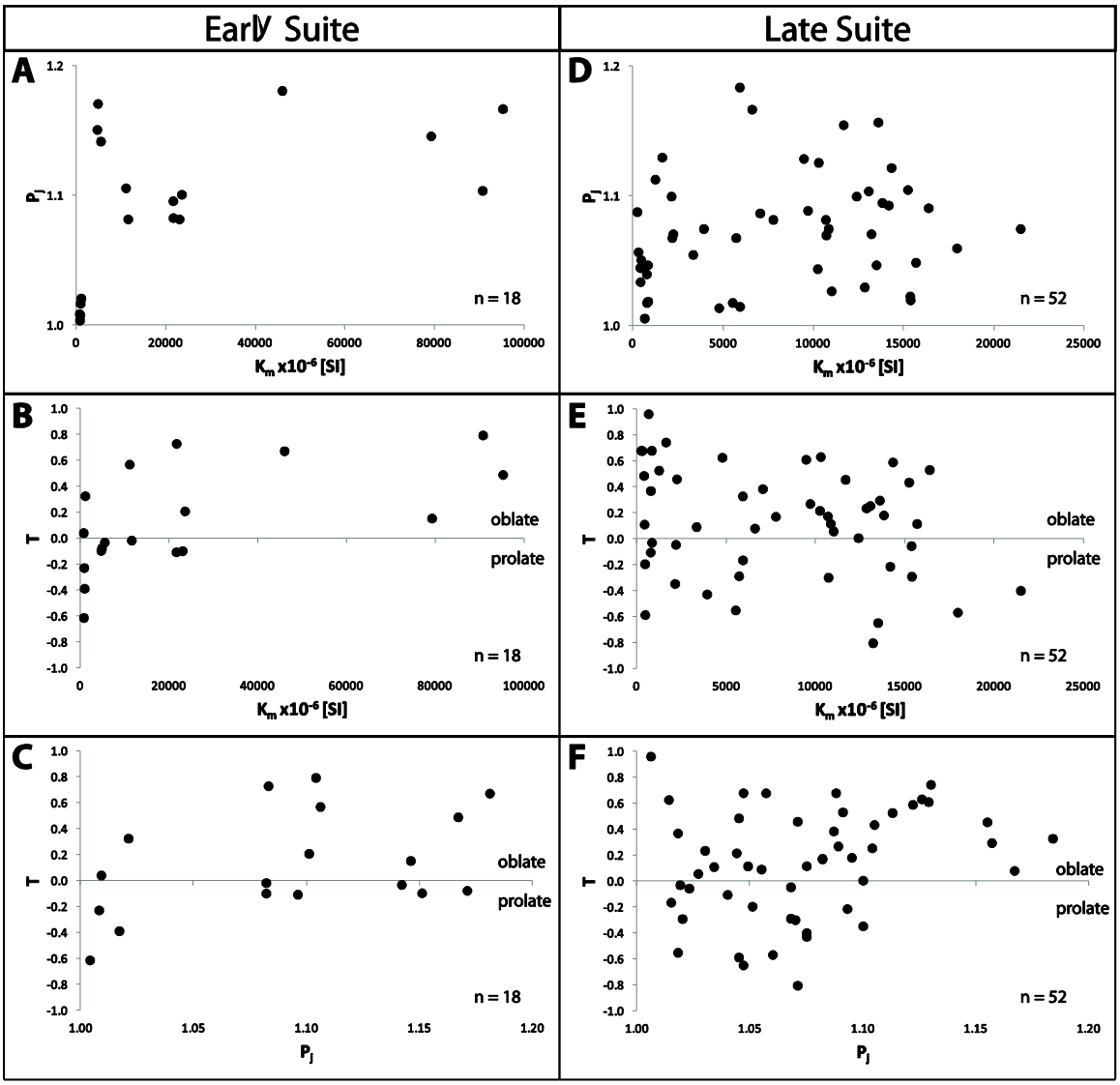

Figure 5.1.1: Plots of AMS data for early (left) and late (right) suite specimens. (A-D) P_j vs. K_m. (B-E) T_j vs. K_m. (C-F) T_j vs. P_j.

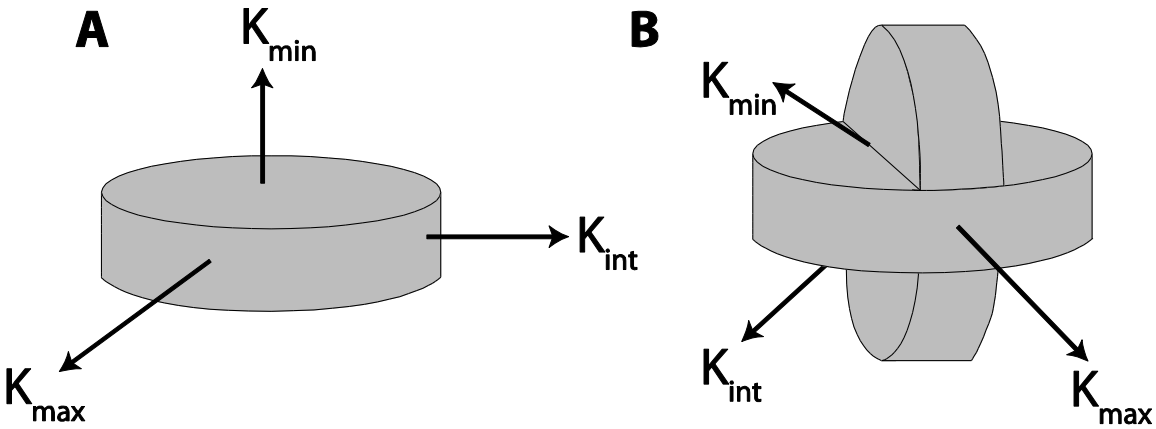

Figure 5.1.2: Schematic illustration of susceptibility axes of discs (magnetic minerals) and the resulting composite fabric. (A) The AMS axes of a single mineral with K_{max} parallel with the long axis of the mineral, and K_{min} normal to the discs flat surface. (B) When two or more orientations of magnetic minerals exist the resulting composite AMS fabric arises from the multiple mineral orientations with K_{min} representing a mean vector of the combination of varying K_{min}. Shown here are two perfectly orthogonal discs, but any mineral angles are possible. Modified from Housen et al. (1993).

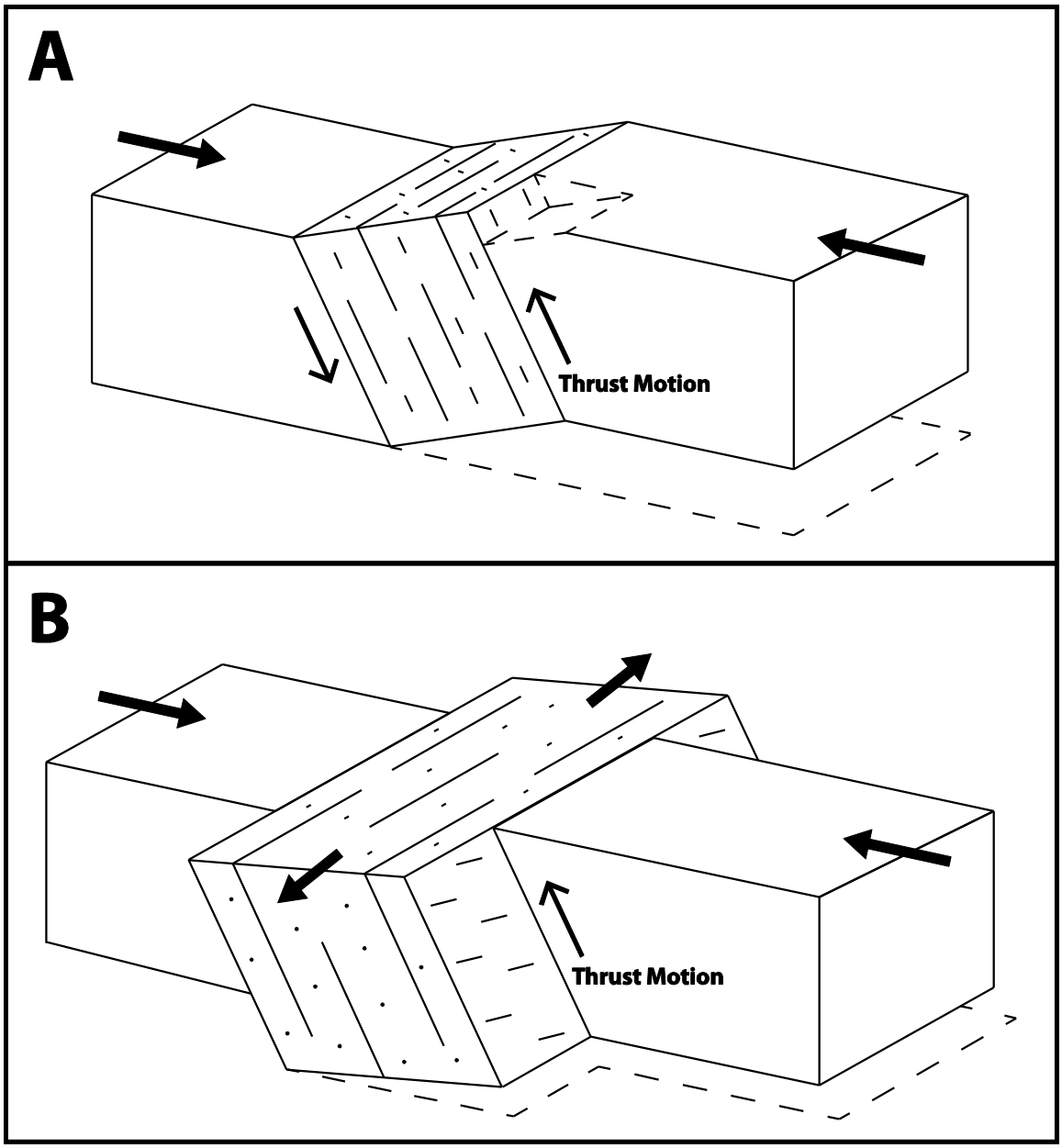

Figure 5.4.1: Schematic of deformation kinematics as interpreted by field and AMS orientations. (A) Represents AMS and field measurements seen in the early suite representing typical simple shear along a thrust plane. (B) Fabrics are drawn for the case in the late suite where strike parallel extension dominates indicated by the rotation of lineations from parallel to thrust transport to shallowly plunging parallel of fault strike. Long lines in the deforming block represent foliations, and short lines represent lineations.

6. Conclusions

The Loch Borralan Pluton was emplaced and cooled synkinematically with motion along regional thrust faults. The mineral shape fabrics seen at the outcrop and thin section scale and the AMS fabrics are all consistent with deformation related to the thrust faults. The fabrics in the early suite (431 ± 1.2 Ma) include shallowly dipping lineations parallel to thrust transport direction and foliations that strike parallel to the strike of regional thrusts, which are consistent with deformation by thrusting accommodated by simple shear. The late suite (429.2 ± 0.5 Ma) has transport parallel lineations in the field, but also a mix of AMS lineations representing both classic thrust motion and fault strike parallel extension. This mixture of AMS lineation orientations may be due to a change in kinematics during emplacement and/or partitioning between localized zones of thrust and lateral extrusion dominated fabrics. The "girdled" AMS foliations in the late suite are likely due to a composite fabric formed by thrust related simple shearing and flattening.

The Loch Borralan Pluton began its ascent around the time of initial movements of the Moine Thrust, indicated by the relative similar crystallization age (~431-429 Ma) to the calculated age of ductile movements (~437-408 Ma; Freeman et al. 1998; Goodenough et al. 2011). The pluton was deformed under a range of temperature conditions from high grade deformation mechanisms seen in feldspars (grain boundary bulging, perthite, myrmekite) and quartz (grain boundary bulging), to medium grade conditions in feldspars (undulose extinction, bending/kinking) and quartz (undulose extinction, dynamic recrystallization), down to low grade brittle deformation in both quartz and feldspars (fractures). The complete lack of pristine magmatically derived microstructures and prevalence of deformation microstructures throughout demonstrates

that the pluton was deforming during emplacement at high temperatures, and continued deforming well into its solidification at cooler temperatures. Assuming the timing of the Sole, Borralan, Ben More, and Moine Thrusts are in-sequence, the Sole Thrust would be the last to propagate meaning the pluton could have been strained by all neighboring faults prior to crystallization. The higher abundance and intensity of microstructures seen in the early suite and southeast late suite, proximal to the Ben More Thrust, suggest that much of the strain in the pluton was due to movements along this fault.

The deformation nature of the Loch Borralan Pluton has significant regional implications. Studies of the neighboring Loch Ailsh Pluton with a crystallization age of (~430 Ma) should be expected to have similar fabrics as the Loch Borralan late suite (~431 Ma). While this study lacks evidence to absolutely date the movements of any particular regional fault, the presence of low temperature brittle deformation microstructures demonstrate that the pluton intruded early enough during deformation to become relatively cool while deformation progressed. So deformation continued after the crystallization age of the Loch Borrlan pluton. The absolute ages of when deformation began, and end remain unknown.

The pluton is an excellent example of the usefulness of fabrics in syn-orogenic magmatism within contractional tectonic regimes for paleo-strain analyses. The early suite is representative of classic lineation/foliation strain studies of simple shear in thrust faults, whereas the late suite provides insight into the variable fabric orientations that may occur in granites with combinations of flattening, shear, and strike parallel extension. Fault strike lateral extension is an interesting solution for the plutonic “space problem,” something that is not thus far documented within all contractual orogens. The use of

commonplace field and laboratory techniques demonstrates that even complex paleo-strain problems can be solved with the combination of detailed field observations and analytical techniques.

7. References

Aranguren, A., Cuevas, J., Tubía, J.M., Román-Berdiel, T., Casas-Sainz, A., and Casas-Ponsati, A., 2003, Granite laccolith emplacement in the Iberian arc: AMS and gravity study of the La Tojiza pluton (NW Spain). Journal of the Geological Society, London, v. 160, p. 435-445.

Archanjo, C.J., Campanha, G.A.C., Salazar, C.S., & Launeau, P., 2012, Using AMS combined with mineral shape preferred orientation analysis to understand the emplacement fabrics of the Apiai gabbro-norite (Ribeira Belt, SE Brazil). International Journal of Earth Science, v. 101, p. 731-745.

Benn, K., 2009, Anisotropy of magnetic susceptibility fabrics in syntectonic plutons as tectonic strain markers: the example of the Canso pluton, Meguma Terrane, Nova Scotia. Earth and Environmental Science Transactions of the Royal Society of Edinburgh, v. 100, p. 147-158.

Blakey, R., 2010, Colorado Plateau Geosystems Inc: http://cpgeosystems.com/425_Sil_EurMap_plates.jpg (accessed December 2013).

Borradaile, G.J., 1988, Magnetic susceptibility, petrofabrics and strain – a review. Tectonophysics, v. 156, p. 1-20.

Borradaile, G.J., and Henry, B., 1997, Tectonic applications of magnetic susceptibility and its anisotropy. Earth Science Reviews, v. 42, p. 49-93.

Borradaile, G.J., and Jackson, M., 2010, Structural geology, petrofabrics and magnetic fabrics (AMS, AARM, AIRM). Journal of Structural Geology, v. 32, p. 1519-1551.

Bouchez, J.L., Gleizes, G., Djouadi, T., & Rochette, P., 1990, Microstructure and magnetic susceptibility applied to emplacement kinematics of granites: the example of the Foix pluton (French Pyrenees). Tectonophysics, v. 184, p. 157-171.

Bouchez, J.L. & Gleizes, G., 1995, Two-stage deformation of the Mont-Louis-Andorra granite pluton (Variscan Pyrenees) inferred from magnetic susceptibility anisotropy. Journal of the Geological Society, London, v. 152, p. 669-679.

Bouchez, J.L., 1997, Granite is never isotropic: an introduction to AMS studies of granitic rocks. In: Bouchez, J.L., Hutton, D.H.W., Stephens, W.E. (Eds.), Granite: From Segregation of Melt to Emplacement Fabrics. Kluwer Academic Publishers, p. 95-112.

British Geological Survey, 2013, Digital Geological Map of Great Britain 1:50,000 scale (DiGMapGB-50) data. Version 7.22. Keyworth, Nottingham: British Geological Survey. Title EW150_Dinas Mawddwy. Release date 15-04-2013.

Brown, M., 1994, The generation, segregation, ascent and emplacement of granite magma: the migmatite-to-crustally-derived granite connection in thickened orogens, Earth Science Reviews, v. 36, p. 83-130.

Brun, J.P., Burg, J.P., Ming, C.G., 1985, Strain trajectories above the Main Central Thrust (Himalaya) in southern Tibet. Nature, v. 313, p. 388-390.

Butler, R.F., 1992, Paleomagnetism: Magnetic Domains to Geologic Terranes. Blackwell Scientific Publications, p. 319.

Callaway, C., 1883, The age of the newer gneissose rocks of the northern Highlands. Quarterly Journal of the Geological Society, London, v. 39, p. 355-422.

Cruden, A.R., 1998, On emplacement of tabular granites. Journal of the Geological Society, London, v. 155, p. 853-862.

Cruden, A.R., Tobisch, O.T., & Launeau, P., 1999, Magnetic fabric evidence for conduit-fed emplacement of tabular intrusion: Dinkey Creek Pluton, central Sierra Nevada batholiths, California. Journal of Geophysical Research, v. 104, p. 10,511-10,530.

Cunningham, R.J.H., 1841, Geognostic account of the County of Sutherland. Transactions of the Highland and Agricultural Society of Scotland, v. 7, p. 73-114.

Czeck, D.M., Maes, S.M., Sturm, C.L., Fein, E.M., 2006, Assessment of the relationship between emplacement of the Algoman plutons and regional deformation in the Rainy Lake region, Ontario. Canadian Journal of Earth Sciences, v. 43, p. 1653-1671.

Day, R., Fuller, M., and Schmidt, V.A., 1977, Hysteresis properties of titanomagnetites: Grain-size and compositional dependence. Physics of the Earth and Planetary Interiors, v. 13, i. 4, p. 260-267.

Deer, A., Howie, R.A., and Zussman, J., 1982, Rock-forming minerals, Vol. 1A: Orthosilicates, 2nd Ed. The Geological Society, London, 932 p.

Deer, A., Howie, R., Wise, W.S., and Zussman, J., 2004, Rock Forming Minerals, Vol. 4B: Framework Silicates: Silica Minerals, Feldspathoids and the Zeolites, 2nd Ed. The Geological Society, London, 982 p.

Dunlop, D.J., 2002, Theory and application of the Day plot (Mrs/Ms versus Hcr/Hc): theoretical curves and tests using titanomagnetite data. Journal of Geophysical Research, v. 107, p. EPM 4-1 – EPM 4-22.

Elliott, D., and Johnson, M.R.W., 1980, Structural evolution in the northern part of the Moine thrust belt, NW Scotland: Transactions of the Royal Society of Edinburgh: Earth Sciences, v. 71, p. 69-96.

Ellis, M. & Watkinson, A.J., 1987, Orogen-parallel extension and oblique tectonics: The relation between stretching lineations and relative plate motions. Geology, v. 15, p. 1022-1026.

Fernández, C., and Castro, A., 1999, Pluton accommodation at high strain rates in the upper continental crust: the example of the Central Extremadura batholith, Spain. Journal of Structural Geology, v. 21, p. 1143-1149.

Fernández, C., Czeck, D. M., and Díaz-Azpiroz, M., 2013, Testing the model of oblique transpression with oblique extrusion in two natural cases: steps and consequences. Journal of Structural Geology, v. 54, p. 85-102.

Freeman, S.R., Butler, R.W.H., Cliff, R.A., and Rex, D.C., 1998, Direct dating of mylonite evolution: a multi-disciplinary geochronological study from the Moine Thrust Zone, NW Scotland: Journal of the Geological Society, London, v. 155, p. 745-758.

Geikie, A., 1884, The crystalline schists of the Scottish Highlands. Nature, v. 31, p. 29-31.

Goodenough, K.M., Millar, I., Strachan, R.A., Krabbendam, M. & Evans, J.A., 2011, Timing of regional deformation and development of the Moine Thrust Zone in the Scottish Caledonides: constraints from the U-Pb geochronology of alkaline intrusions. Journal of the Geological Society, London, v. 168, p. 99-114.

Halliday, A.N., Aftalion, M., Parsons, I., Dickin, A.P., & Johnson, M.R.W., 1987, Syn-orogenic alkaline magmatism and its relationship to the Moine Thrust Zone and the thermal state of the Lithosphere in NW Scotland. Journal of the Geological Society, London, v. 144, p. 611-617.

Hastie, W.W., Aubourg, C., and Watkeys, M., 2011, When an 'inverse' fabric is not inverse: and integrated AMS-SPO study in MORB-like dykes. Terra Nova, v. 23, no. 1, p. 49-55.

Hirth, G., and Tullis, J., 1992, Dislocation creep regimes in quartz aggregates. Journal of Structural Geology, v. 14, p. 145-159.

Housen, B.A., Richter, C., and van der Pluijm, A., 1993, Composite magnetic anisotropy fabrics: experiments, numerical models, and implications for the quantification of rock fabrics. Tectonophysics, v. 220, p. 1-12.

Hunt, C.P., Moskowitz, B.M., Banerjee, S.K., 1995, Magnetic Properties of Rocks and Minerals. Published by American Geophysical Union, p. 189-204.

Hutton, D.H.W., Dempster, T.J., Brown, P.E., and Becker, S.D., 1990, A new mechanism of granite emplacement: intrusion in active extensional shear zones. Nature, v. 343, p. 452-455.

Izquierdo-Llavall, E., Román-Berdiel, T., Casas, A.M., Oliva-Urcia, B., Gil-Peña, I., Soto, R., and Jabaloy, A., 2012, Magnetic and structural study of the Eaux-

Chaudes intrusion: understanding the Variscan deformation in the Western Axial Zone (Pyrenees). International Journal of Earth Sciences, v. 101, i. 7, p. 1817-1834.

Jelinek, V., 1981, Characterization of the magnetic fabric of rocks. Tectonophysics, v. 79: T63-T67.

Lapworth, C., 1883, On the structure and metamorphism of the rocks of the Durness-Eriboll district. Proceedings of the Geological Association, v. 8, p. 438-442.

Lapworth, C., 1885, The highland controversy in British Geology; its causes, course and consequences. Nature, v. 32, p. 558-559.

Launeau, P., & Cruden, A.R., 1998, Magmatic fabric acquisition mechanisms in a syenite: Results of a combined anisotropy of magnetic susceptibility and image analysis study. Journal of Geophysical Research, v. 104, p. 5067-5089.

Launeau, P., & Robin, P.Y.F., 1996, Fabric analysis using the intercept method. Tectonophysics, v. 267, p. 91-119.

Law, R.D., Mainprice, D., Casey, M., Lloyd, G.E., Knipe, R.J., Cook, B., & Thigpen, J.R., 2010, Moine Thrust zone mylonites at the Stack of Glencoul: I – microstructures, strain and influence of recrystallization on quartz crystal fabric development. In: Law, R.D., Butler, R.W.H., Holdsworth, R.E., Krabbendam, M. & Strachan, R.A. (eds) Continental Tectonics and Mountain Building; The legacy of Peach and Horne. Geological Society, London, Special Publications, v. 355, p. 543-577.

Leslie, A.G., Krabbendam, M., Kimbel, G.S., and Strachan, R.A., 2010, Region-scale lateral variation and linkage in ductile thrust architecthure: the Oykel Transverse Zone, and mullions in the Moine Nappe, NW Scotland. In: Law, R. D., Butler, R. W. H., Holdsworth, R. E., Krabbendam, M. & Strachan, R. A. (eds) Continental Tectonics and Mountain Building; The legacy of Peach and Horne. Geological Society, London, Special Publications, v. 355, p. 359-381.

Macculloch, J., 1836. A Geological Map of Scotland. Arrowsmith, London.

Maes, S.M., Tikoff, B., Ferré, E.C., Brown, P.E., Miller Jr., J.D., 2007, The Sonju Lake layered intrusion, northeast Minnesota: Internal structure and emplacement history from magnetic fabrics. Precambrian Research, v. 157, p. 269-288.

Mookerjee, M., and Mitra, G., 2009, Understanding kinematic data from the Moine thrust zone in terms of kinematics-based mathematical model of deforming thrust wedges. Journal of Structural Geology, v. 31, p. 1556-1572.

Murchinson, R.I. & Geikie, A., 1861, On the altered rocks of the western island of Scotland, and the northwestern and central Highlands. Quarterly Journal of the Geological Society, London, v. 17, p. 171-229.

Neilson, J.C., Kokelaar, B.P. & Crowley, Q.G., 2009, Timing, relations and cause of plutonic and volcanic activity of the Siluro-Devonian post-collision magmatic episode in the Grampian Terrane, Scotland, Journal of the Geological Society, London, v. 166, pp. 545-561.

Nicol, J., 1844, Guide to the Geology of Scotland. Oliver and Boyd, Edinburgh.

Oliver, G.J.H., Chen, F., Buchwaldt, R., Hegner, E., 2000, Fast tectonometamorphism and exhumation in the type area of the Barrovian and Buchan zones: Geology, v. 28, p. 459-462.

Oliver, G.J.H., Wilde, S.A. & Wan, Y., 2008, Geochronology and geodynamics of Scottish granitoids from the late Neoproterozoic break-up of Rodinia to Palaeozoic collision. Journal of the Geological Society, London, v. 165, p. 661-674.

Park, R.G., Stewart, A.D. & Wright, D.T., 2002, The Hebridean Terrane, In: Trewin, N. H. (ed.) The Geology of Scotland. Geological Society, London, p. 45-80.

Parsons, I., 1965, The feldspathic syenites of the Loch Ailsh intrusion, Assynt, Scotland. Journal of Petrology, v. 6, p. 365-394.

Parsons, I., 1999, Late Ordovician to mid-Silurian alkaline intrusions of the Northwest Highlands of Scotland. In: Stephenson, D., Bevins, R. E., Millward, D., Highton, A. J., Parsons., I., Stone, P. & Wadsworth, W. J. (eds) Caledonian Igneous Rocks of Great Britain. Geological Conservation Review Series, No. 17. Joint Nature Conservancy Committee, Peterborough, p. 345-394.

Passchier, C.W., & Trouw, R.A.J., 2005, Microtectonics, 2nd ed. Springer-Verlag Berlin Heidelberg, Germany, 365 p.

Paterson, S.R., Fowler, T.K. Jr., Schmidt, K.L., Yoshinobu, A.S., Yuan, E.S., Miller, R.B., 1998, Interpreting magmatic fabric patterns in plutons: Lithos, v. 44, p. 53-82.

Peach, B.N. & Horne, J., 1884, Report on the geology of the North-West of Sutherland. Nature, v. 31, p. 31-35.

Peach, B.N., Horne, J., Gunn, W., Clough, C.T., Hinxman, L.W. & Cadell, H.M., 1888, Report on the recent work of the Geological Survey in the North-west Highlands of Scotland, based on the field-notes and maps of Messers. B. N. Peach, J. Horne, W. Gunn, C. T. Clough, L. Hinxman, and H. M. Cadell. Quarterly Journal of the Geological Society, London, v. 44, p. 378-441.

Peach, B.N., Horne, J., Gunn, W., Clough, C.T., Hinxman, L.W. & Cadell, H.M., 1891, Geological Map of Scotland, 1 inch to 1 mile, sheet 114. Geological Survey of Scotland.

Peach, B.N., Horne, J., Gunn, W., Clough, C.T., Hinxman, L.W. & Teall, J.J.H., 1907, The Geological Structure of the North-West Highlands of Scotland. Memoirs of the Geological Survey of Great Britain. HMSO, Glasgow.

Peach, B.N. & Horne, J., 1914, Guide to the Geological Model of the Assynt Mountains. Edinburgh Geological Survey and Museum, Edinburg, p. 1-32.

Pignotta, G.S. & Benn, K., 1999, Magnetic fabric of the Barrington Passage pluton, Meguma Terrane, Nova Scotia: a two-stage fabric history of syntectonic emplacement: Tectonophysics, v. 307, p. 75-92.

Pitcher, W.S., 1993, The nature and origin of granite. 2nd ed. Blackie Academic & Professional Publishing, Glasgow, 321 p.

Pryer, L.L., 1993, Microstructures in feldspars from a major crustal thrust zone: the Grenville Front, Ontario, Canada. Journal of Structural Geology, v. 15, p. 21-36.

Searle, M.P., Law, R.D., Dewey, J.F. & Streule, M.J., 2010, Relationships between the Loch Ailsh and Borralan alkaline intrusions and thrusting in the Moine Thrust zone, southern Assynt culmination, NW Scotland. In: Law, R. D., Butler, R. W. H., Holdsworth, R. E., Krabbendam, M. & Strachan, R. A. (eds) Continental Tectonics and Mountain Building; The legacy of Peach and Horne. Geological Society, London, Special Publications, v. 355, p. 383-404.

Sibson, R.H., 1982, Fault zone models, heat flow, and depth distribution of earthquakes in the continental crust of the United States: Bulletin of the Seismological Society of America, v. 72, p. 151-163.

Simpson, C., and Wintsch, R.P., 1989, Evidence for deformation-induced K-feldspar replacement by myrmekite. Journal of Metamorphic Geology, v. 7, p. 261-275.

Smith, J.V., MacKenzie, W.S., 1958, The alkali feldspars: IV. The cooling history of high-temperature sodium-rich feldspars. The American Mineralogist, v. 43, p. 872-889.

Stewart, M., Holdsworth, R.E., and Strachan, R.A., 2000, Deformation processes and weakening mechanisms within the frictional-viscous transition zone of major crustal-scale faults: insights from the Great Glen fault zone, Scotland. Journal of Structural Geology, v. 22, p. 543-560.

Strachan, R.A., Smith, M., Harris, A.L., and Fettes, D.J., 2002, The Northern Highlands and Grampian terranes, in Trewin, N.H., ed., The Geology of Scotland: The Geological Society, London, p. 81-148.

Strachan, R.A., and Thigpen, J.R., 2007, Peach and Horne Meeting, in Continental Tectonics and Mountain Building: A Guide to Field Excursions: Ullapool, Scotland, 116 p.

Tullis, J., and Yund, R.A., 1979, Calculation of coherent solvi for alkali feldspar, iron-free clinopyroxene, nepheline-kalsilite, and hematite-ilmenite. American Mineralogist, v. 64, p. 1063-1074.

van Breemen, O., Aftalion, M., Johnson, M.R.W., 1979, Age of the Loch Borralan complex, Assynt, and the late movements along the Moine Thrust Zone. Journal of Geological Society, London, v. 136, p. 489-495.

van Breemen, O., & Bluck, B.J., 1981, Episodic granite plutons in the Scottish Caledonides. Nature, v. 291, p. 113-117.

Vernon, R.H., 2004, A practical guide to rock microstructure. Cambridge University Press, Cambridge, UK, 593 p.

Weiler, P.D. & Coe, R.S., 1997, Paleomagnetic evidence for rapid vertical-axis rotations during thrusting in an active collision zone, northeastern Papua New Guinea. Tectonics, v. 16, no. 3, p. 537-550.

Woolley, A.R., 1965, The Loch Borrolan alkaline igneous complex. Unpublished PhD thesis, University of London.

Woolley, A.R., 1970, The structural relationships of the Loch Borralan complex, Scotland. Geological Journal, v. 7, p. 171-182.

Woolley, A.R. 1973, The pseudoleucite borralanites and associated rocks of the southeastern tract of the Borralan complex, Scotland. Bulletin British Museum of Natural History, v. 2, p. 6.

Yang, Y, and Liu, M., 2009, Crustal thickening and lateral extrusion during the Indo-Asian collision: A 3D viscous flow model. Tectonophysics, v. 465, p. 128-135.

Zak, J., Schulmann, K., & Hrouda, F., 2005, Multiple magmatic fabrics in the Sazava Pluton (Bohemian Massive, Czech Republic); a result of superposition of wrench-dominated regional transpression on final emplacement. Journal of Structural Geology, v. 27, p. 805-822.

Appendix A: Hysteresis Loops

Appendix A: Hysteresis data of 40 representative samples within an alternating field (H) of 1 Tesla (T). Red line represents raw data, blue is just the ferromagnetic component. Magnetization (M).

EARLY SUITE

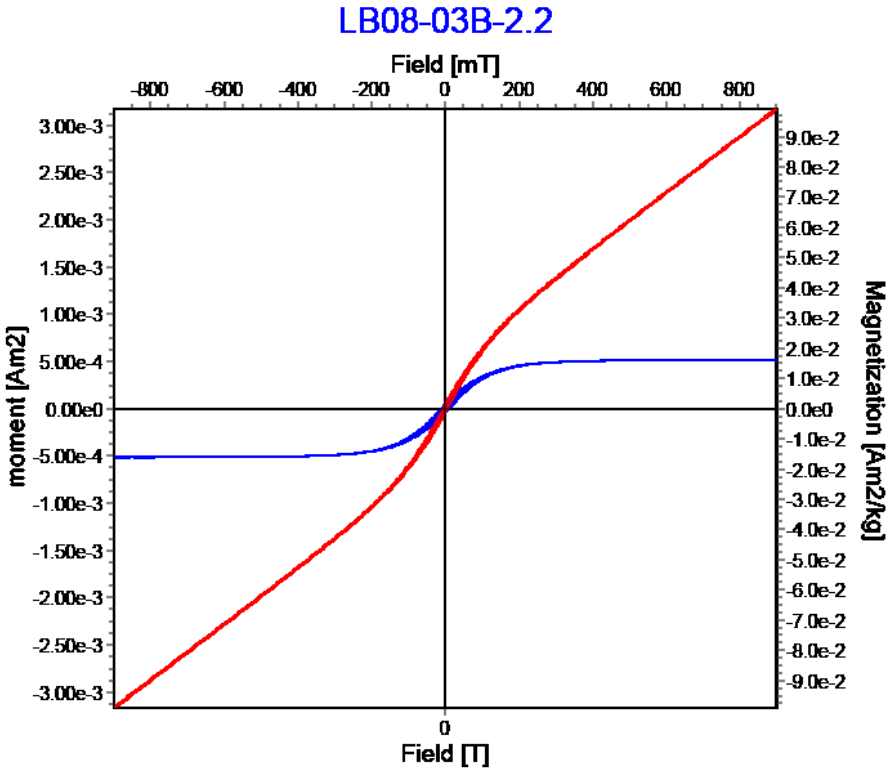
LB08-03B-2.2
Field [mT]
-800 -600 -400 -200 0 200 400 600 800
3.00e-3
2.50e-3
2.00e-3
1.50e-3
1.00e-3
5.00e-4
0.00e0
-5.00e-4
-1.00e-3
-1.50e-3
-2.00e-3
-2.50e-3
-3.00e-3
moment [Am2]
9.0e-2
8.0e-2
7.0e-2
6.0e-2
5.0e-2
4.0e-2
3.0e-2
2.0e-2
1.0e-2
0.0e0
-1.0e-2
-2.0e-2
-3.0e-2
-4.0e-2
-5.0e-2
-6.0e-2
-7.0e-2
-8.0e-2
-9.0e-2
Magnetization [Am2/kg]
0
Field [T]

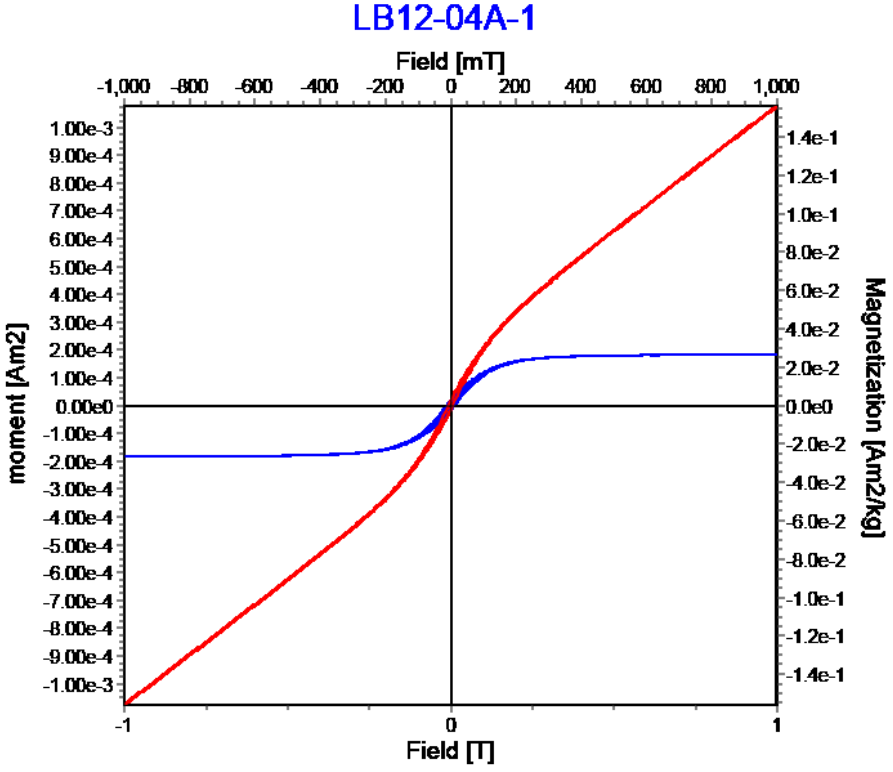
LB12-04A-1
Field [mT]
-1,000 -800 -600 -400 -200 0 200 400 600 800 1,000
1.00e-3
9.00e-4
8.00e-4
7.00e-4
6.00e-4
5.00e-4
4.00e-4
3.00e-4
2.00e-4
1.00e-4
0.00e0
-1.00e-4
-2.00e-4
-3.00e-4
-4.00e-4
-5.00e-4
-6.00e-4
-7.00e-4
-8.00e-4
-9.00e-4
-1.00e-3
moment [Am2]
1.4e-1
1.2e-1
1.0e-1
8.0e-2
6.0e-2
4.0e-2
2.0e-2
0.0e0
-2.0e-2
-4.0e-2
-6.0e-2
-8.0e-2
-1.0e-1
-1.2e-1
-1.4e-1
Magnetization [Am2/kg]
-1
0
1
Field [T]

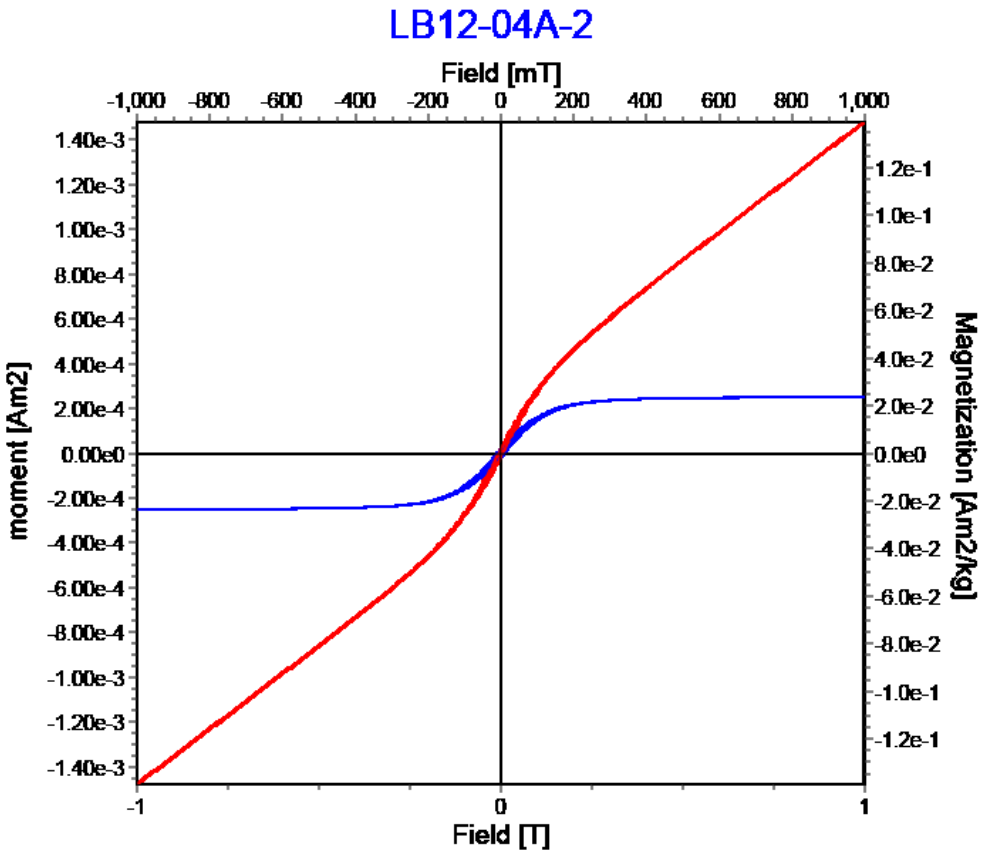
LB12-04A-2
Field [mT]
-1,000 -800 -600 -400 -200 0 200 400 600 800 1,000
1.40e-3 1.20e-3 1.00e-3 8.00e-4 6.00e-4 4.00e-4 2.00e-4 0.00e0 -2.00e-4 -4.00e-4 -6.00e-4 -8.00e-4 -1.00e-3 -1.20e-3 -1.40e-3
moment [Am2]
1.2e-1 1.0e-1 8.0e-2 6.0e-2 4.0e-2 2.0e-2 0.0e0 -2.0e-2 -4.0e-2 -6.0e-2 -8.0e-2 -1.0e-1 -1.2e-1
Magnetization [Am2/kg]
-1 0 1
Field [T]

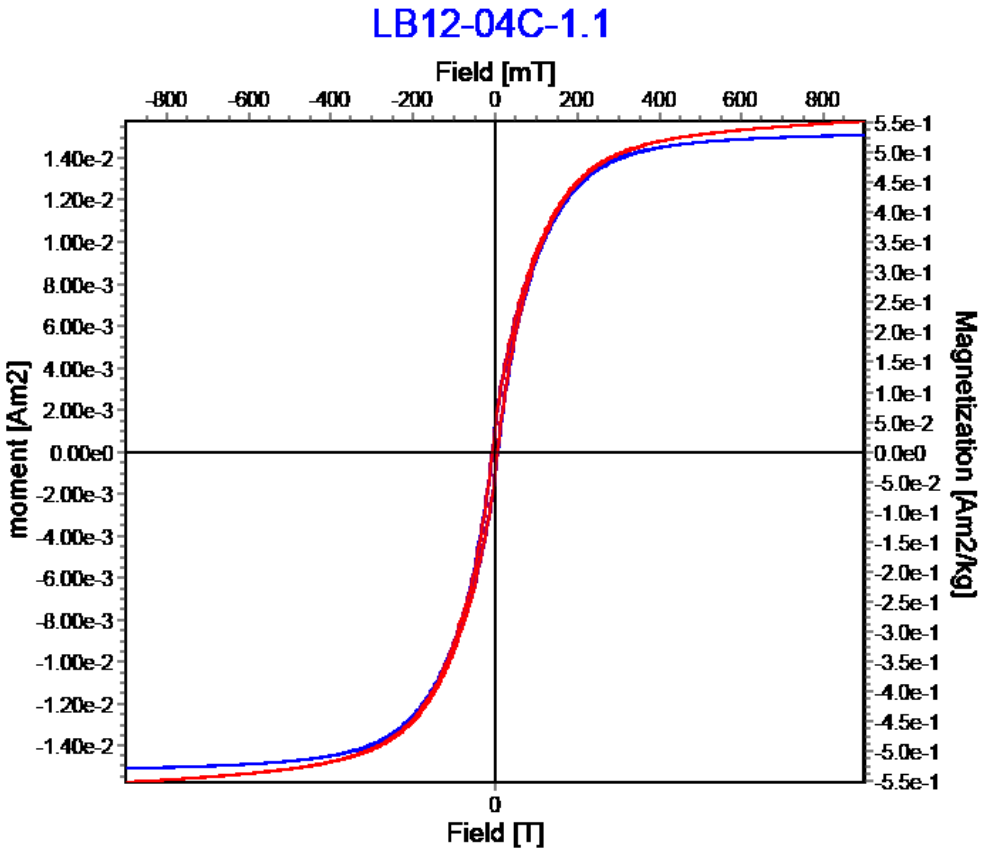
LB12-04C-1.1
Field [mT]
-800 -600 -400 -200 0 200 400 600 800
1.40e-2 1.20e-2 1.00e-2 8.00e-3 6.00e-3 4.00e-3 2.00e-3 0.00e0 -2.00e-3 -4.00e-3 -6.00e-3 -8.00e-3 -1.00e-2 -1.20e-2 -1.40e-2
moment [Am2]
5.5e-1 5.0e-1 4.5e-1 4.0e-1 3.5e-1 3.0e-1 2.5e-1 2.0e-1 1.5e-1 1.0e-1 5.0e-2 0.0e0 -5.0e-2 -1.0e-1 -1.5e-1 -2.0e-1 -2.5e-1 -3.0e-1 -3.5e-1 -4.0e-1 -4.5e-1 -5.0e-1 -5.5e-1
Magnetization [Am2/kg]
0
Field [T]

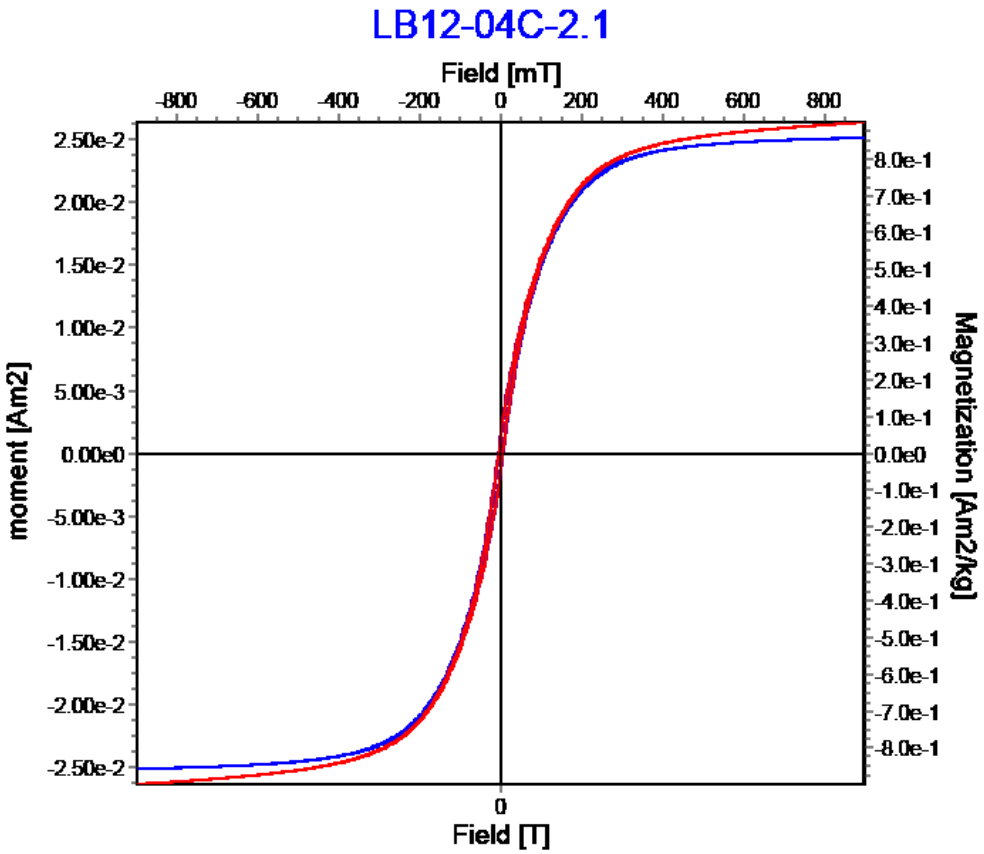
LB12-04C-2.1
Field [mT]
-800 -600 -400 -200 0 200 400 600 800
2.50e-2 2.00e-2 1.50e-2 1.00e-2 5.00e-3 0.00e0 -5.00e-3 -1.00e-2 -1.50e-2 -2.00e-2 -2.50e-2
moment [Am2]
8.0e-1 7.0e-1 6.0e-1 5.0e-1 4.0e-1 3.0e-1 2.0e-1 1.0e-1 0.0e0 -1.0e-1 -2.0e-1 -3.0e-1 -4.0e-1 -5.0e-1 -6.0e-1 -7.0e-1 -8.0e-1
Magnetization [Am2/kg]
0
Field [T]

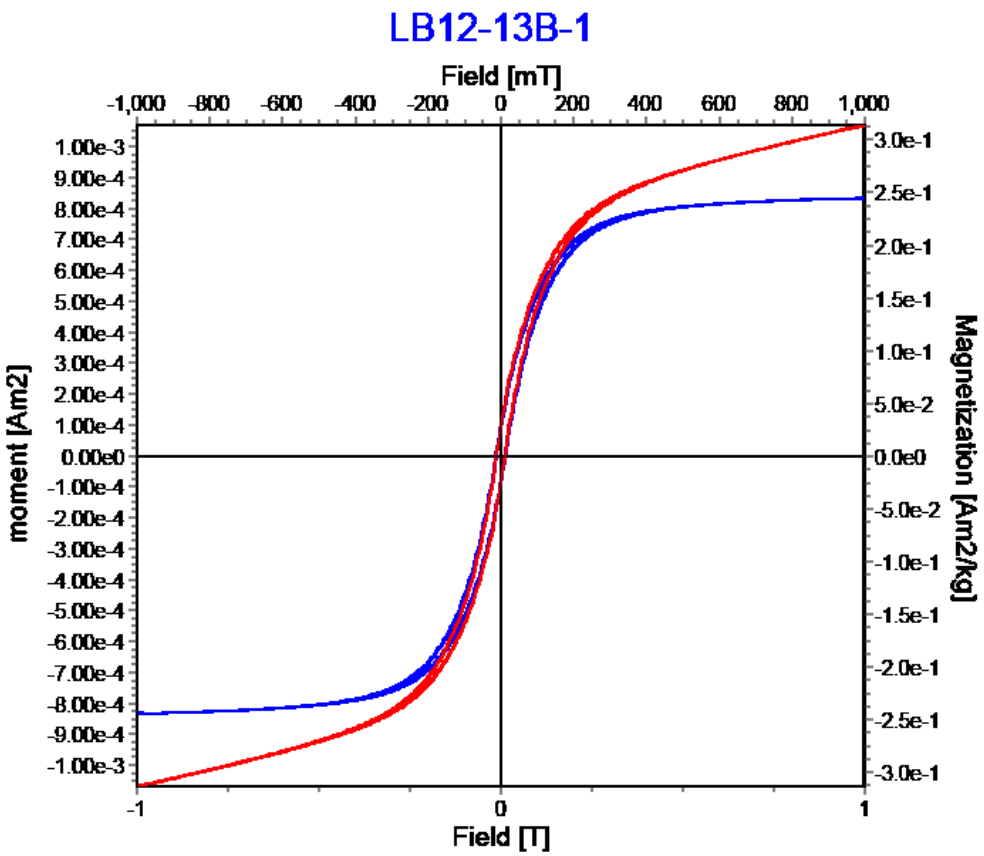
LB12-13B-1
Field [mT]
-1,000 -800 -600 -400 -200 0 200 400 600 800 1,000
1.00e-3 9.00e-4 8.00e-4 7.00e-4 6.00e-4 5.00e-4 4.00e-4 3.00e-4 2.00e-4 1.00e-4 0.00e0 -1.00e-4 -2.00e-4 -3.00e-4 -4.00e-4 -5.00e-4 -6.00e-4 -7.00e-4 -8.00e-4 -9.00e-4 -1.00e-3
moment [Am2]
3.0e-1 2.5e-1 2.0e-1 1.5e-1 1.0e-1 5.0e-2 0.0e0 -5.0e-2 -1.0e-1 -1.5e-1 -2.0e-1 -2.5e-1 -3.0e-1
Magnetization [Am2/kg]
-1 0 1
Field [T]

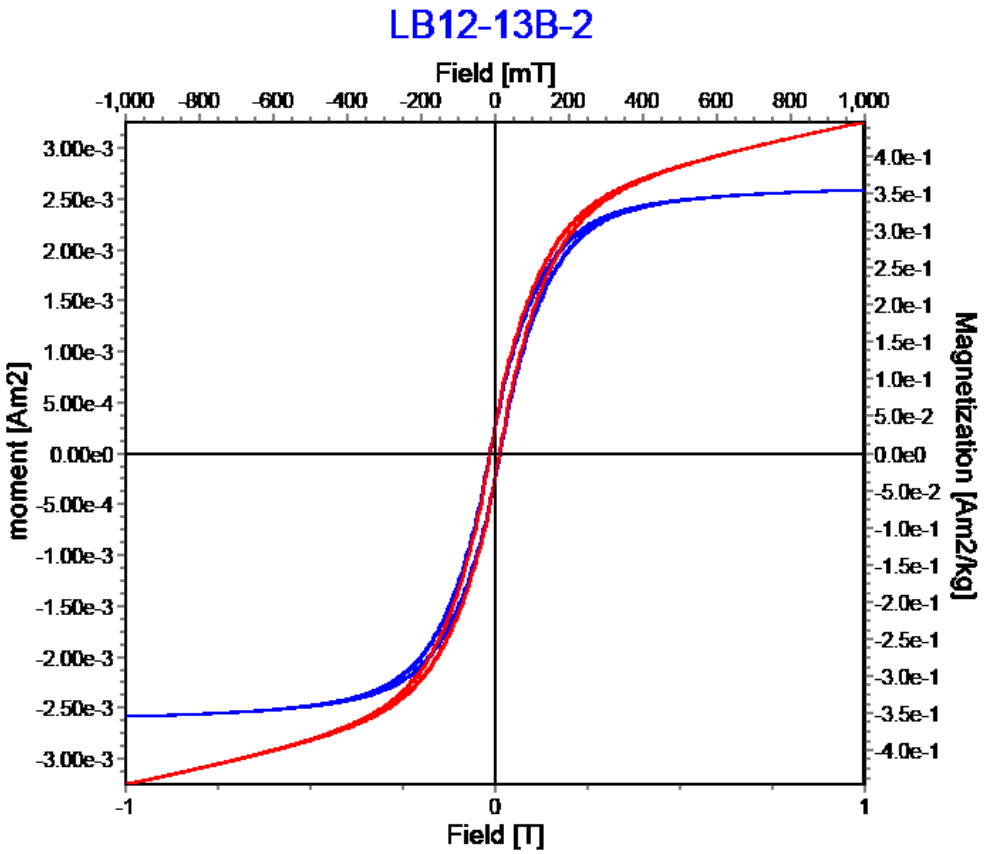
LB12-13B-2
Field [mT]
-1,000 -800 -600 -400 -200 0 200 400 600 800 1,000
moment [Am2]
3.00e-3 2.50e-3 2.00e-3 1.50e-3 1.00e-3 5.00e-4 0.00e0 -5.00e-4 -1.00e-3 -1.50e-3 -2.00e-3 -2.50e-3 -3.00e-3
Magnetization [Am2/kg]
4.0e-1 3.5e-1 3.0e-1 2.5e-1 2.0e-1 1.5e-1 1.0e-1 5.0e-2 0.0e0 -5.0e-2 -1.0e-1 -1.5e-1 -2.0e-1 -2.5e-1 -3.0e-1 -3.5e-1 -4.0e-1
-1 0 1
Field [T]

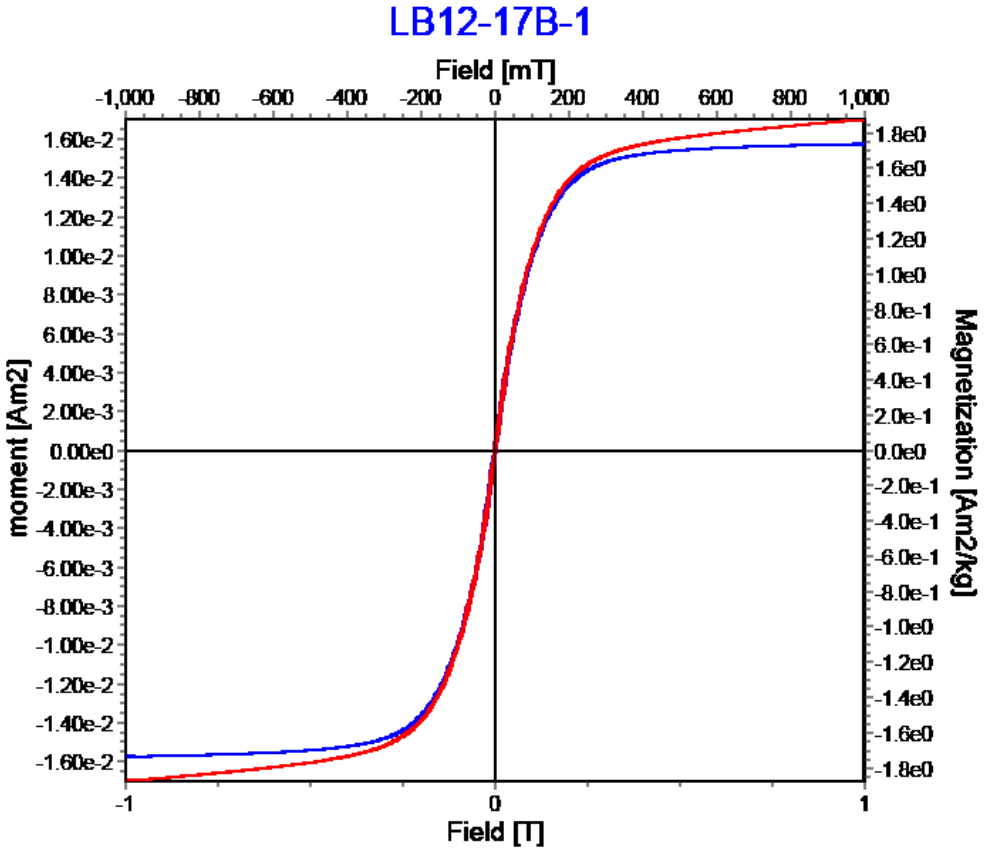
LB12-17B-1
Field [mT]
-1,000 -800 -600 -400 -200 0 200 400 600 800 1,000
moment [Am2]
1.60e-2 1.40e-2 1.20e-2 1.00e-2 8.00e-3 6.00e-3 4.00e-3 2.00e-3 0.00e0 -2.00e-3 -4.00e-3 -6.00e-3 -8.00e-3 -1.00e-2 -1.20e-2 -1.40e-2 -1.60e-2
Magnetization [Am2/kg]
1.8e0 1.6e0 1.4e0 1.2e0 1.0e0 8.0e-1 6.0e-1 4.0e-1 2.0e-1 0.0e0 -2.0e-1 -4.0e-1 -6.0e-1 -8.0e-1 -1.0e0 -1.2e0 -1.4e0 -1.6e0 -1.8e0
-1 0 1
Field [T]

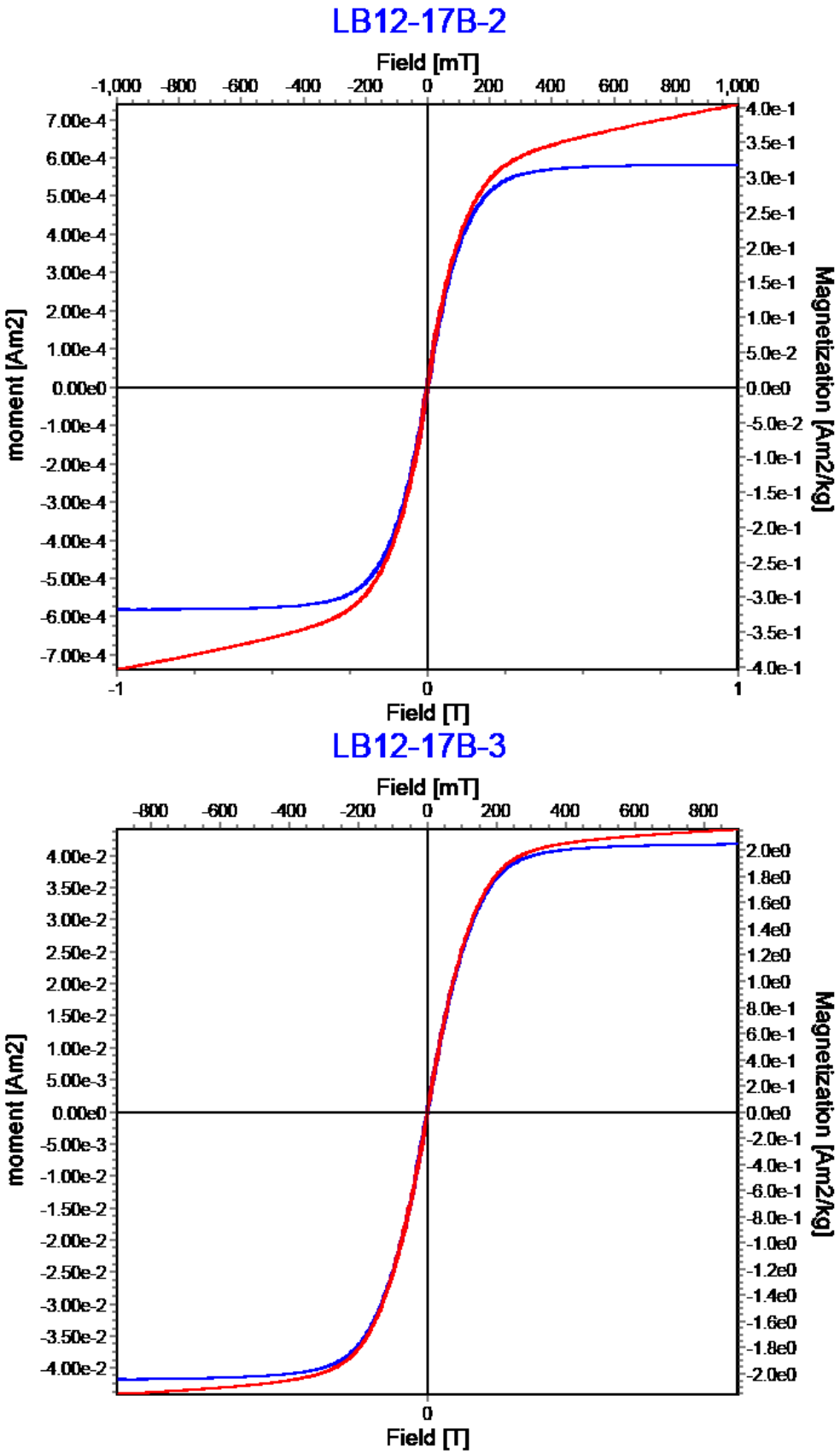
LB12-17B-2
Field [mT]
-1,000 -800 -600 -400 -200 0 200 400 600 800 1,000
7.00e-4 6.00e-4 5.00e-4 4.00e-4 3.00e-4 2.00e-4 1.00e-4 0.00e0 -1.00e-4 -2.00e-4 -3.00e-4 -4.00e-4 -5.00e-4 -6.00e-4 -7.00e-4
moment [Am2]
4.0e-1 3.5e-1 3.0e-1 2.5e-1 2.0e-1 1.5e-1 1.0e-1 5.0e-2 0.0e0 -5.0e-2 -1.0e-1 -1.5e-1 -2.0e-1 -2.5e-1 -3.0e-1 -3.5e-1 -4.0e-1
Magnetization [Am2/kg]
-1 0 1
Field [T]
LB12-17B-3
Field [mT]
-800 -600 -400 -200 0 200 400 600 800
4.00e-2 3.50e-2 3.00e-2 2.50e-2 2.00e-2 1.50e-2 1.00e-2 5.00e-3 0.00e0 -5.00e-3 -1.00e-2 -1.50e-2 -2.00e-2 -2.50e-2 -3.00e-2 -3.50e-2 -4.00e-2
moment [Am2]
2.0e0 1.8e0 1.6e0 1.4e0 1.2e0 1.0e0 8.0e-1 6.0e-1 4.0e-1 2.0e-1 0.0e0 -2.0e-1 -4.0e-1 -6.0e-1 -8.0e-1 -1.0e0 -1.2e0 -1.4e0 -1.6e0 -1.8e0 -2.0e0
Magnetization [Am2/kg]
0
Field [T]

LATE SUITE

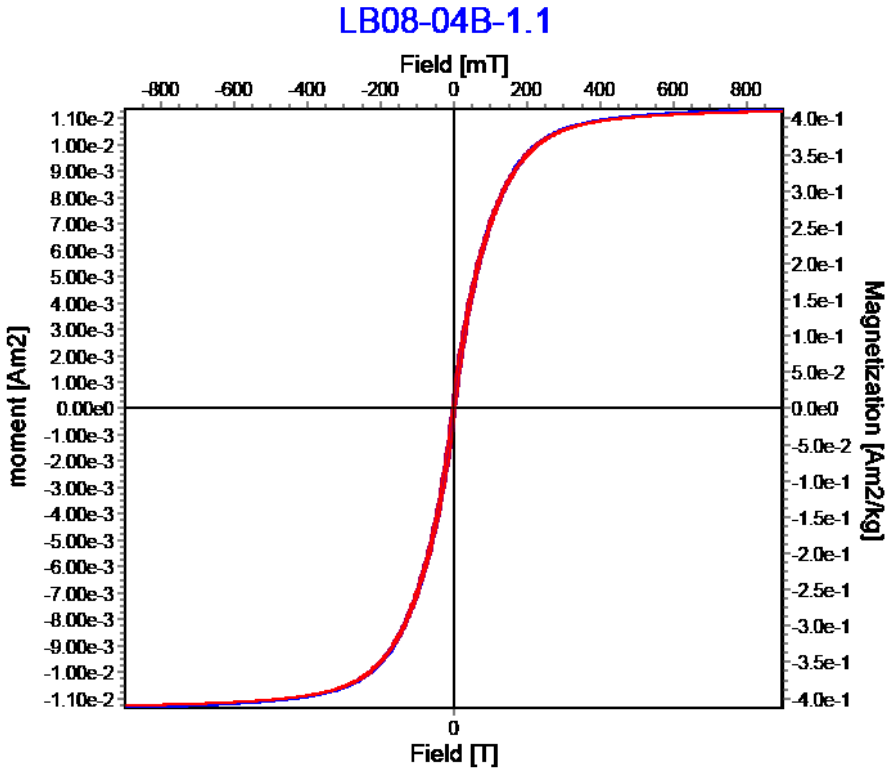
LB08-04B-1.1
Field [mT]
-800 -600 -400 -200 0 200 400 600 800
moment [Am2]
1.10e-2 1.00e-2 9.00e-3 8.00e-3 7.00e-3 6.00e-3 5.00e-3 4.00e-3 3.00e-3 2.00e-3 1.00e-3 0.00e0 -1.00e-3 -2.00e-3 -3.00e-3 -4.00e-3 -5.00e-3 -6.00e-3 -7.00e-3 -8.00e-3 -9.00e-3 -1.00e-2 -1.10e-2
Magnetization [Am2/kg]
4.0e-1 3.5e-1 3.0e-1 2.5e-1 2.0e-1 1.5e-1 1.0e-1 5.0e-2 0.0e0 -5.0e-2 -1.0e-1 -1.5e-1 -2.0e-1 -2.5e-1 -3.0e-1 -3.5e-1 -4.0e-1
0
Field [T]

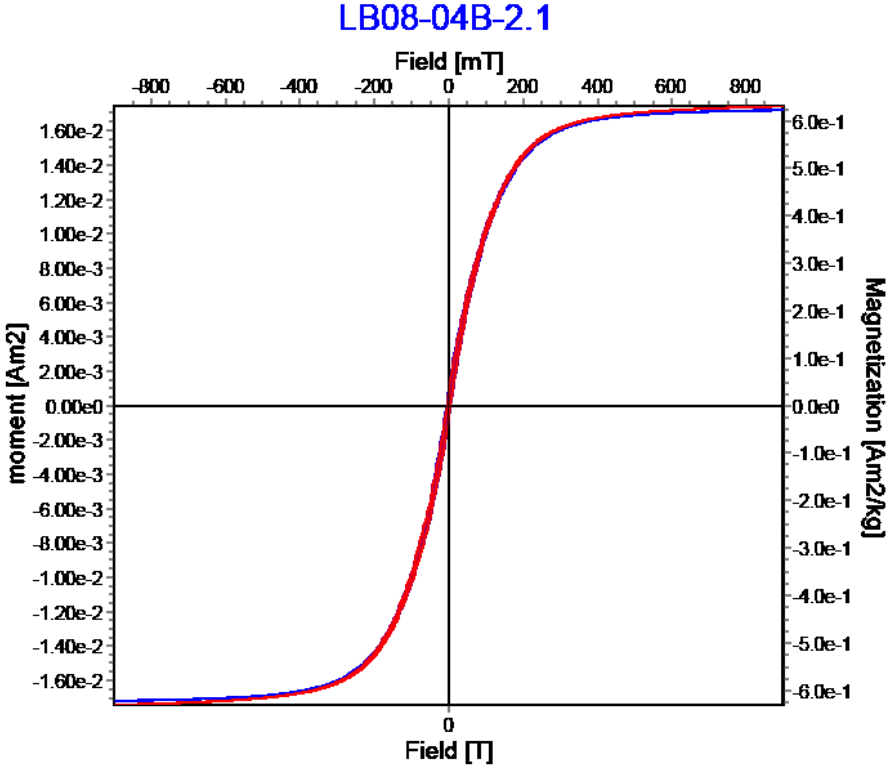
LB08-04B-2.1
Field [mT]
-800 -600 -400 -200 0 200 400 600 800
moment [Am2]
1.60e-2 1.40e-2 1.20e-2 1.00e-2 8.00e-3 6.00e-3 4.00e-3 2.00e-3 0.00e0 -2.00e-3 -4.00e-3 -6.00e-3 -8.00e-3 -1.00e-2 -1.20e-2 -1.40e-2 -1.60e-2
Magnetization [Am2/kg]
6.0e-1 5.0e-1 4.0e-1 3.0e-1 2.0e-1 1.0e-1 0.0e0 -1.0e-1 -2.0e-1 -3.0e-1 -4.0e-1 -5.0e-1 -6.0e-1
0
Field [T]

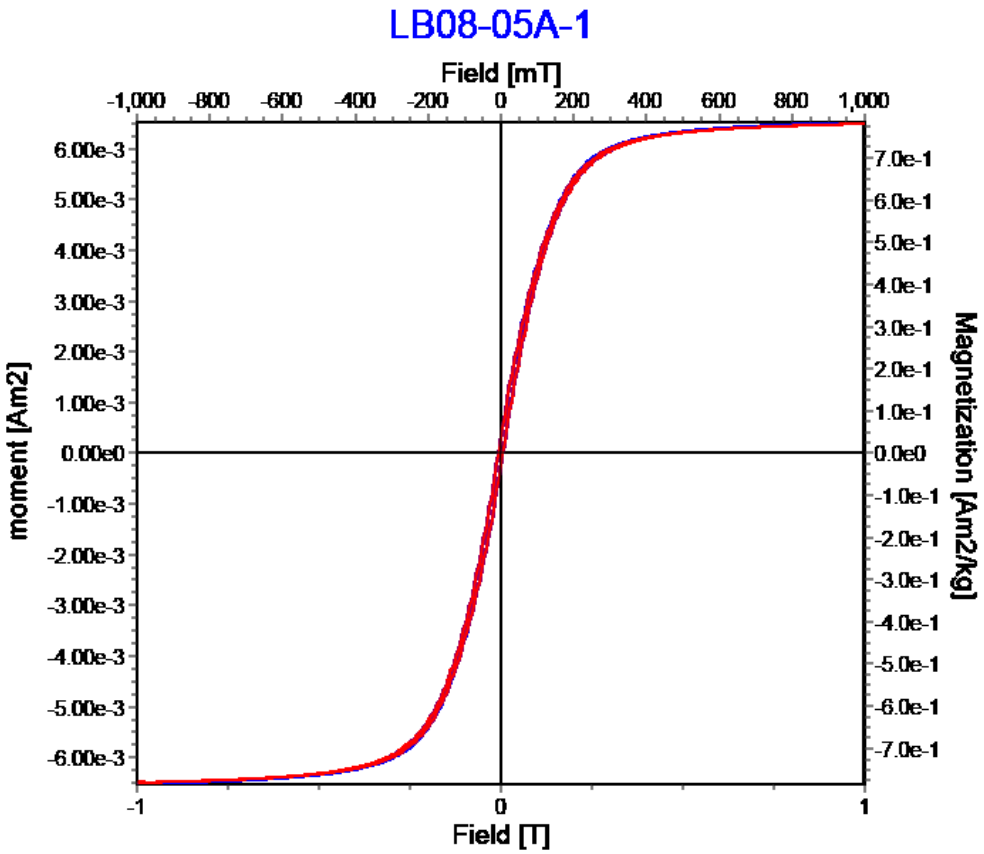
LB08-05A-1
Field [mT]
-1,000 -800 -600 -400 -200 0 200 400 600 800 1,000
6.00e-3
5.00e-3
4.00e-3
3.00e-3
2.00e-3
1.00e-3
0.00e0
-1.00e-3
-2.00e-3
-3.00e-3
-4.00e-3
-5.00e-3
-6.00e-3
moment [Am2]
7.0e-1
6.0e-1
5.0e-1
4.0e-1
3.0e-1
2.0e-1
1.0e-1
0.0e0
-1.0e-1
-2.0e-1
-3.0e-1
-4.0e-1
-5.0e-1
-6.0e-1
-7.0e-1
Magnetization [Am2/kg]
-1
0
1
Field [T]

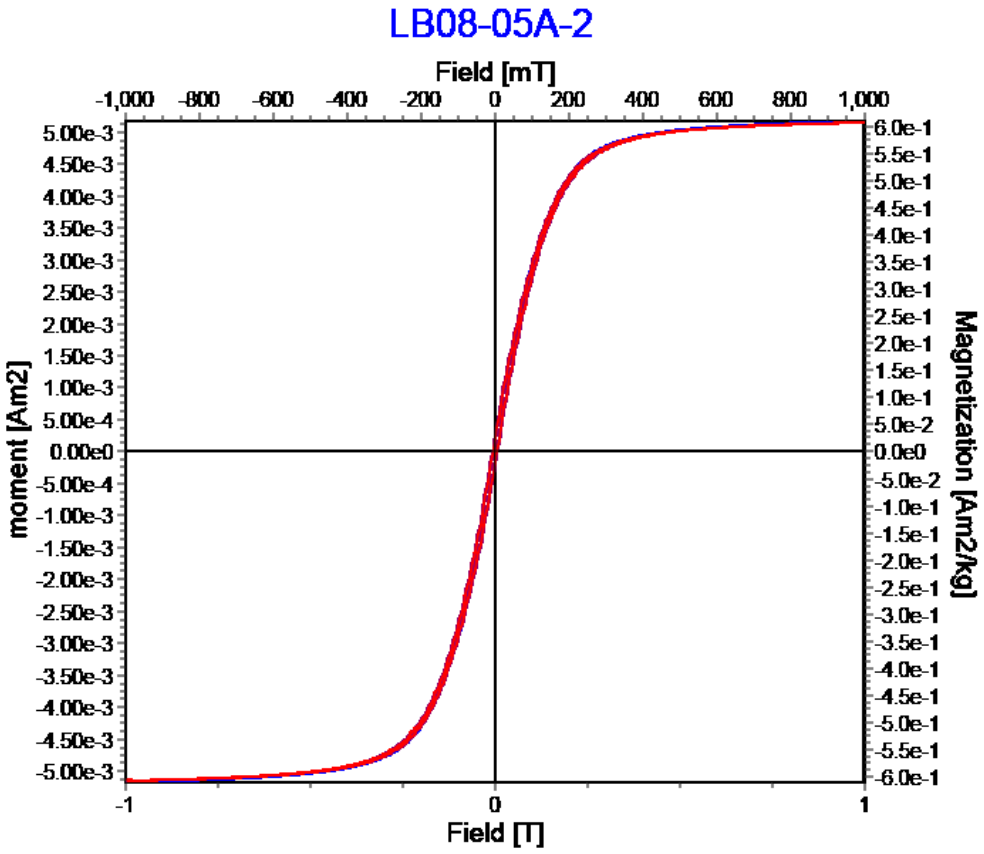
LB08-05A-2
Field [mT]
-1,000 -800 -600 -400 -200 0 200 400 600 800 1,000
5.00e-3
4.50e-3
4.00e-3
3.50e-3
3.00e-3
2.50e-3
2.00e-3
1.50e-3
1.00e-3
5.00e-4
0.00e0
-5.00e-4
-1.00e-3
-1.50e-3
-2.00e-3
-2.50e-3
-3.00e-3
-3.50e-3
-4.00e-3
-4.50e-3
-5.00e-3
moment [Am2]
6.0e-1
5.5e-1
5.0e-1
4.5e-1
4.0e-1
3.5e-1
3.0e-1
2.5e-1
2.0e-1
1.5e-1
1.0e-1
5.0e-2
0.0e0
-5.0e-2
-1.0e-1
-1.5e-1
-2.0e-1
-2.5e-1
-3.0e-1
-3.5e-1
-4.0e-1
-4.5e-1
-5.0e-1
-5.5e-1
-6.0e-1
Magnetization [Am2/kg]
-1
0
1
Field [T]

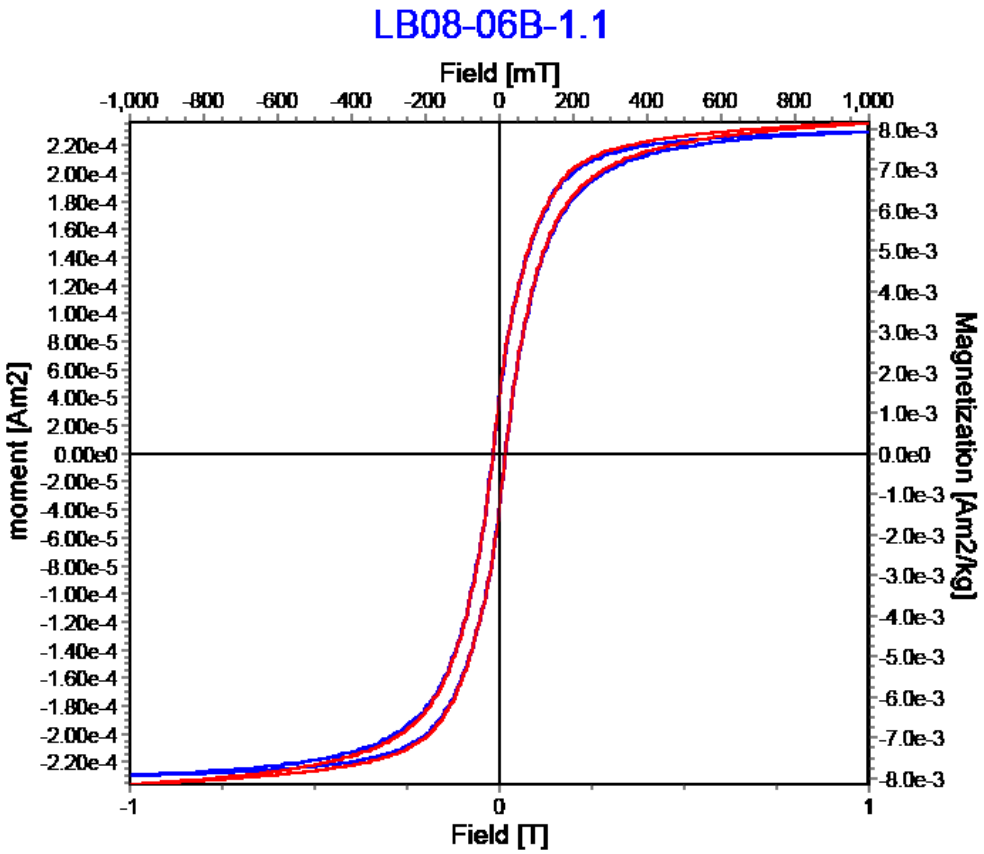
LB08-06B-1.1
Field [mT]
-1,000 -800 -600 -400 -200 0 200 400 600 800 1,000
moment [Am2]
2.20e-4 2.00e-4 1.80e-4 1.60e-4 1.40e-4 1.20e-4 1.00e-4 8.00e-5 6.00e-5 4.00e-5 2.00e-5 0.00e0 -2.00e-5 -4.00e-5 -6.00e-5 -8.00e-5 -1.00e-4 -1.20e-4 -1.40e-4 -1.60e-4 -1.80e-4 -2.00e-4 -2.20e-4
Magnetization [Am2/kg]
8.0e-3 7.0e-3 6.0e-3 5.0e-3 4.0e-3 3.0e-3 2.0e-3 1.0e-3 0.0e0 -1.0e-3 -2.0e-3 -3.0e-3 -4.0e-3 -5.0e-3 -6.0e-3 -7.0e-3 -8.0e-3
-1 0 1
Field [T]

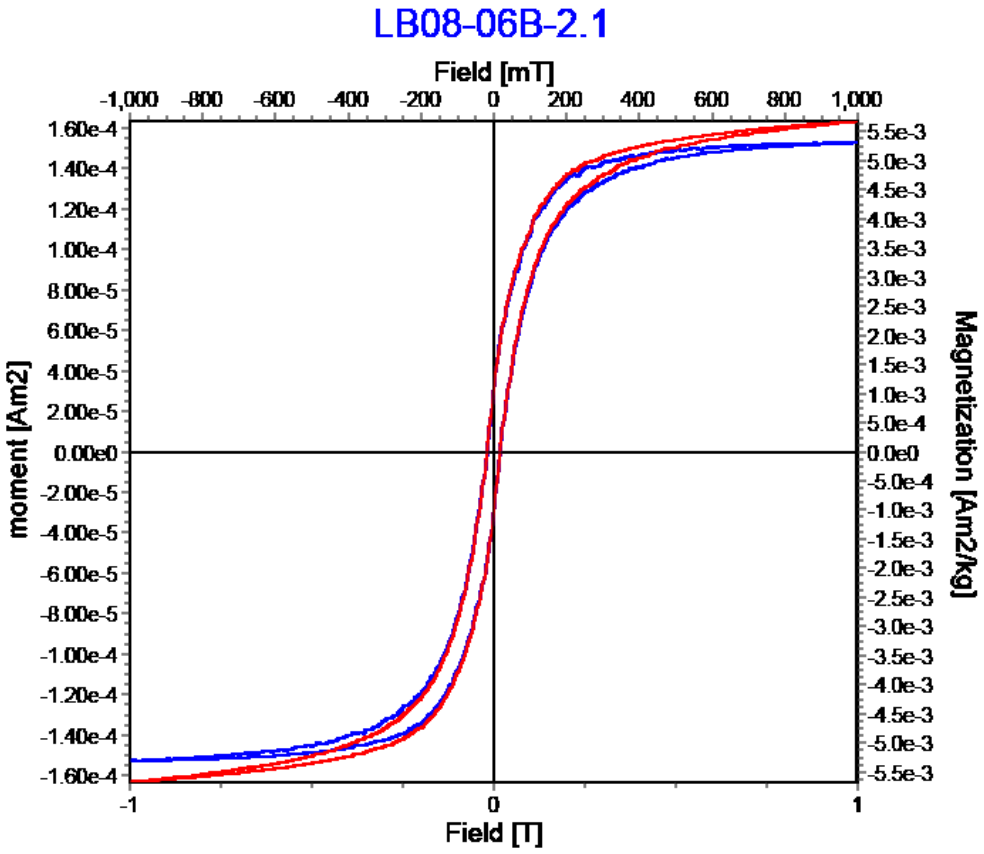
LB08-06B-2.1
Field [mT]
-1,000 -800 -600 -400 -200 0 200 400 600 800 1,000
moment [Am2]
1.60e-4 1.40e-4 1.20e-4 1.00e-4 8.00e-5 6.00e-5 4.00e-5 2.00e-5 0.00e0 -2.00e-5 -4.00e-5 -6.00e-5 -8.00e-5 -1.00e-4 -1.20e-4 -1.40e-4 -1.60e-4
Magnetization [Am2/kg]
5.5e-3 5.0e-3 4.5e-3 4.0e-3 3.5e-3 3.0e-3 2.5e-3 2.0e-3 1.5e-3 1.0e-3 5.0e-4 0.0e0 -5.0e-4 -1.0e-3 -1.5e-3 -2.0e-3 -2.5e-3 -3.0e-3 -3.5e-3 -4.0e-3 -4.5e-3 -5.0e-3 -5.5e-3
-1 0 1
Field [T]

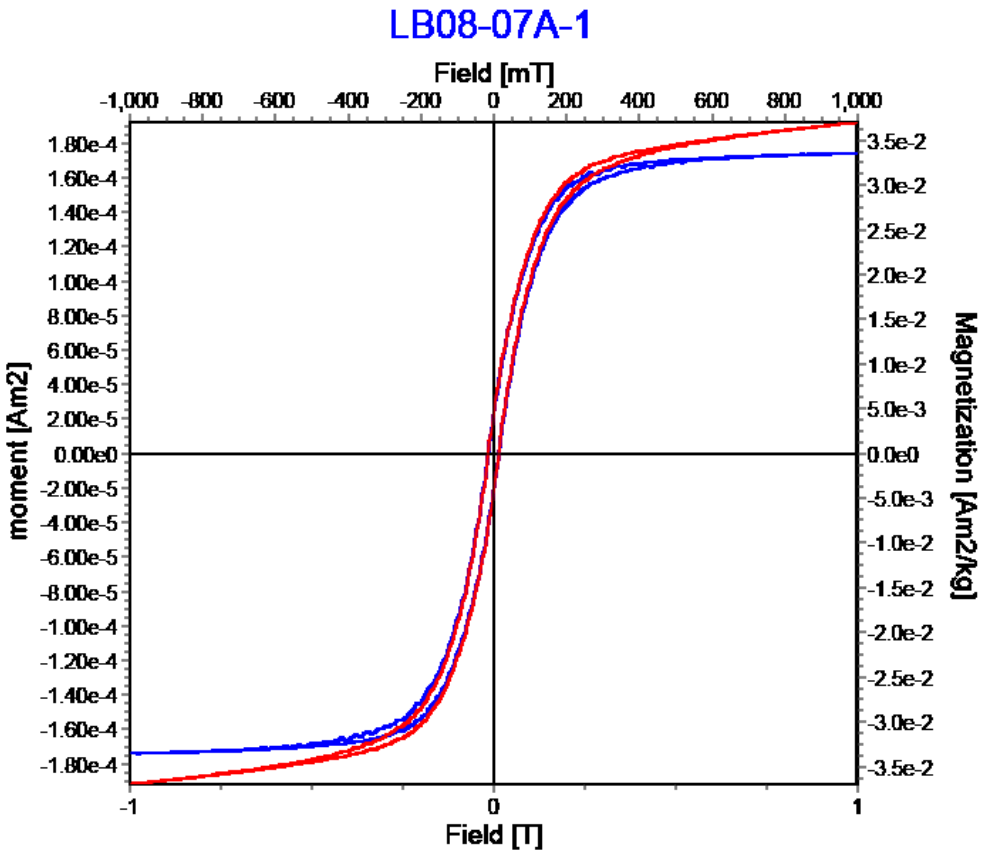
LB08-07A-1
Field [mT]
-1,000 -800 -600 -400 -200 0 200 400 600 800 1,000
moment [Am2]
1.80e-4 1.60e-4 1.40e-4 1.20e-4 1.00e-4 8.00e-5 6.00e-5 4.00e-5 2.00e-5 0.00e0 -2.00e-5 -4.00e-5 -6.00e-5 -8.00e-5 -1.00e-4 -1.20e-4 -1.40e-4 -1.60e-4 -1.80e-4
Magnetization [Am2/kg]
3.5e-2 3.0e-2 2.5e-2 2.0e-2 1.5e-2 1.0e-2 5.0e-3 0.0e0 -5.0e-3 -1.0e-2 -1.5e-2 -2.0e-2 -2.5e-2 -3.0e-2 -3.5e-2
-1 0 1
Field [T]

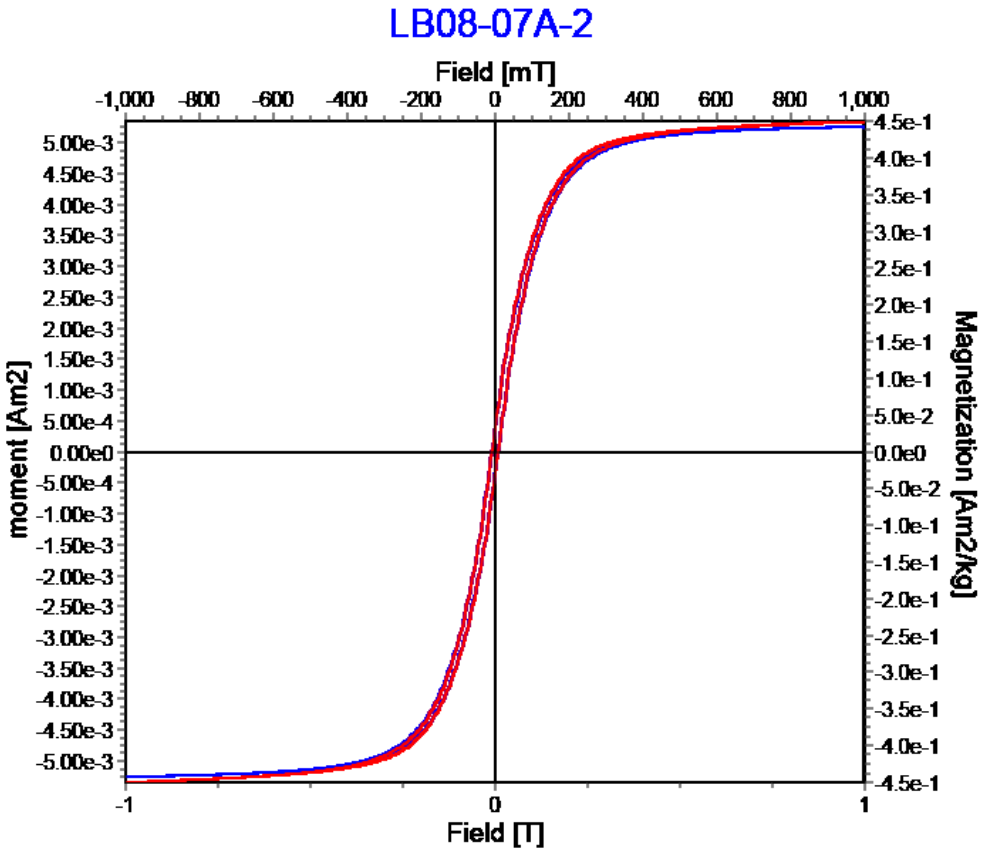
LB08-07A-2
Field [mT]
-1,000 -800 -600 -400 -200 0 200 400 600 800 1,000
moment [Am2]
5.00e-3 4.50e-3 4.00e-3 3.50e-3 3.00e-3 2.50e-3 2.00e-3 1.50e-3 1.00e-3 5.00e-4 0.00e0 -5.00e-4 -1.00e-3 -1.50e-3 -2.00e-3 -2.50e-3 -3.00e-3 -3.50e-3 -4.00e-3 -4.50e-3 -5.00e-3
Magnetization [Am2/kg]
4.5e-1 4.0e-1 3.5e-1 3.0e-1 2.5e-1 2.0e-1 1.5e-1 1.0e-1 5.0e-2 0.0e0 -5.0e-2 -1.0e-1 -1.5e-1 -2.0e-1 -2.5e-1 -3.0e-1 -3.5e-1 -4.0e-1 -4.5e-1
-1 0 1
Field [T]

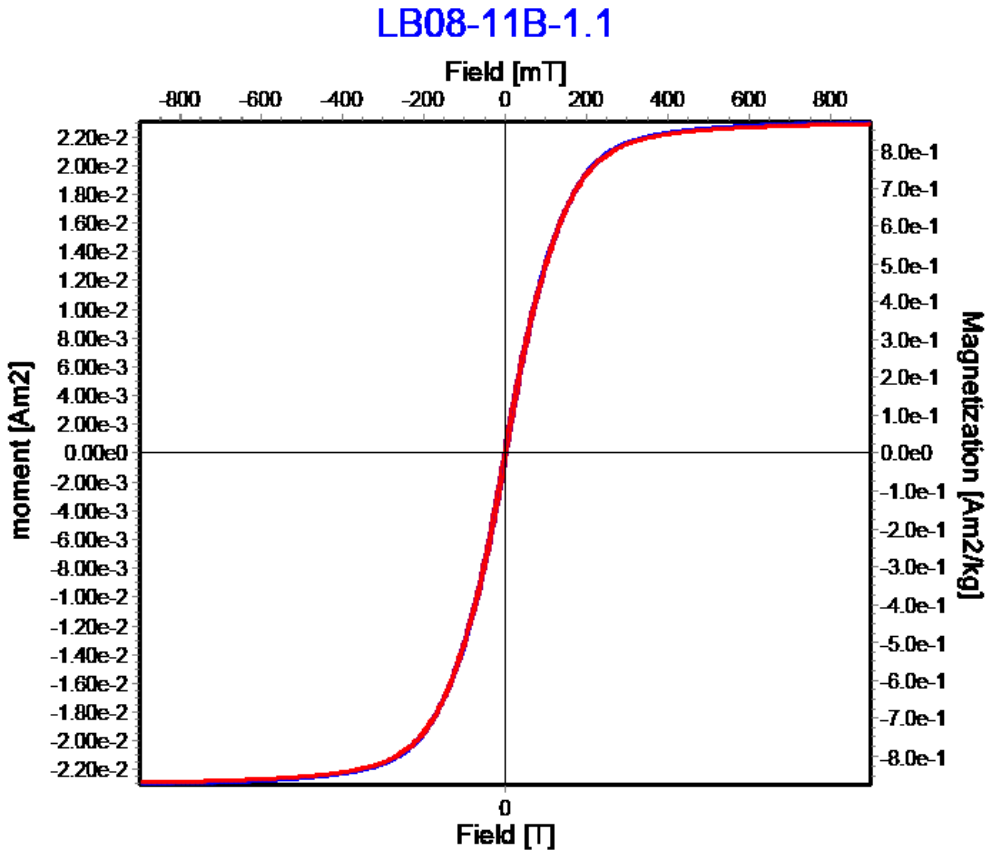
LB08-11B-1.1
Field [mT]
-800 -600 -400 -200 0 200 400 600 800
moment [Am2]
2.20e-2 2.00e-2 1.80e-2 1.60e-2 1.40e-2 1.20e-2 1.00e-2 8.00e-3 6.00e-3 4.00e-3 2.00e-3 0.00e0 -2.00e-3 -4.00e-3 -6.00e-3 -8.00e-3 -1.00e-2 -1.20e-2 -1.40e-2 -1.60e-2 -1.80e-2 -2.00e-2 -2.20e-2
Magnetization [Am2/kg]
8.0e-1 7.0e-1 6.0e-1 5.0e-1 4.0e-1 3.0e-1 2.0e-1 1.0e-1 0.0e0 -1.0e-1 -2.0e-1 -3.0e-1 -4.0e-1 -5.0e-1 -6.0e-1 -7.0e-1 -8.0e-1
0
Field [T]

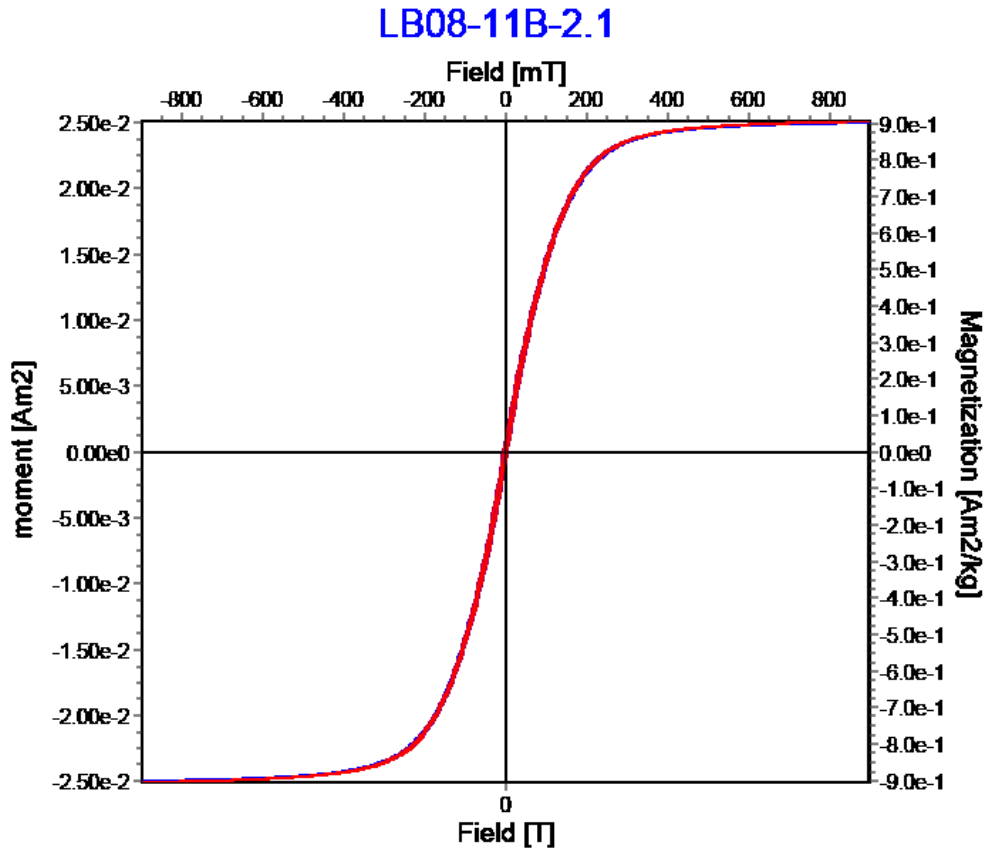
LB08-11B-2.1
Field [mT]
-800 -600 -400 -200 0 200 400 600 800
moment [Am2]
2.50e-2 2.00e-2 1.50e-2 1.00e-2 5.00e-3 0.00e0 -5.00e-3 -1.00e-2 -1.50e-2 -2.00e-2 -2.50e-2
Magnetization [Am2/kg]
9.0e-1 8.0e-1 7.0e-1 6.0e-1 5.0e-1 4.0e-1 3.0e-1 2.0e-1 1.0e-1 0.0e0 -1.0e-1 -2.0e-1 -3.0e-1 -4.0e-1 -5.0e-1 -6.0e-1 -7.0e-1 -8.0e-1 -9.0e-1
0
Field [T]

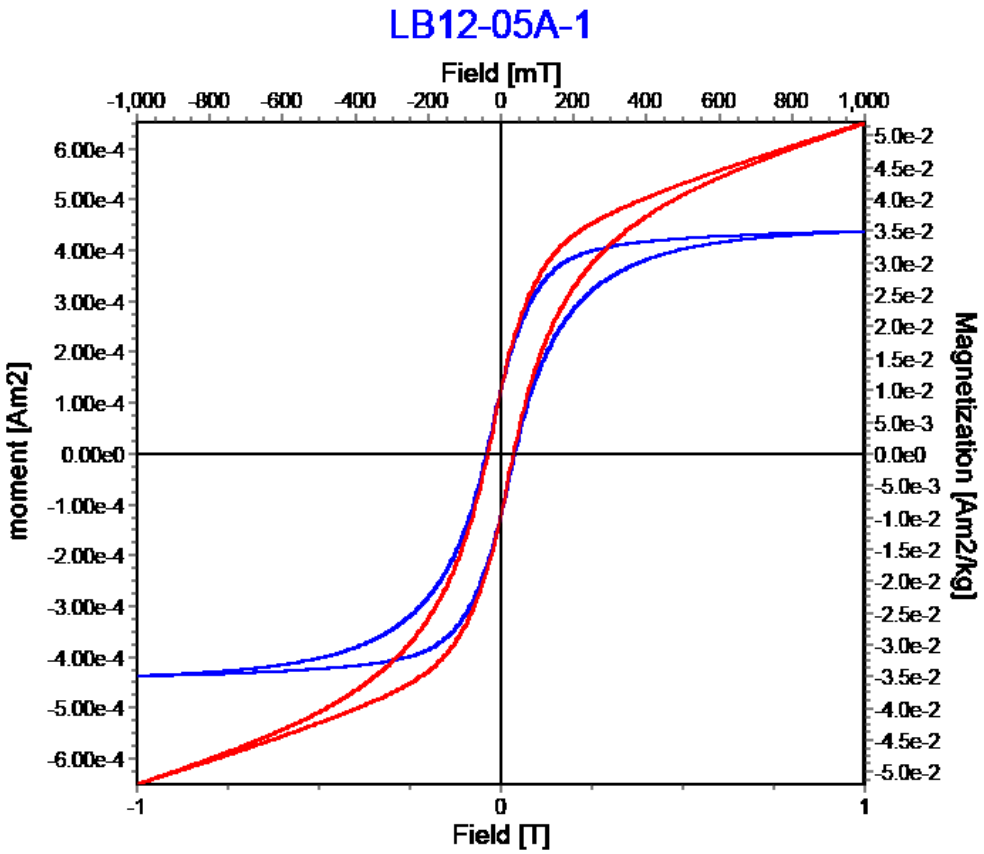
LB12-05A-1
Field [mT]
-1,000 -800 -600 -400 -200 0 200 400 600 800 1,000
6.00e-4
5.00e-4
4.00e-4
3.00e-4
2.00e-4
1.00e-4
0.00e0
-1.00e-4
-2.00e-4
-3.00e-4
-4.00e-4
-5.00e-4
-6.00e-4
moment [Am2]
5.0e-2
4.5e-2
4.0e-2
3.5e-2
3.0e-2
2.5e-2
2.0e-2
1.5e-2
1.0e-2
5.0e-3
0.0e0
-5.0e-3
-1.0e-2
-1.5e-2
-2.0e-2
-2.5e-2
-3.0e-2
-3.5e-2
-4.0e-2
-4.5e-2
-5.0e-2
Magnetization [Am2/kg]
-1
0
1
Field [T]

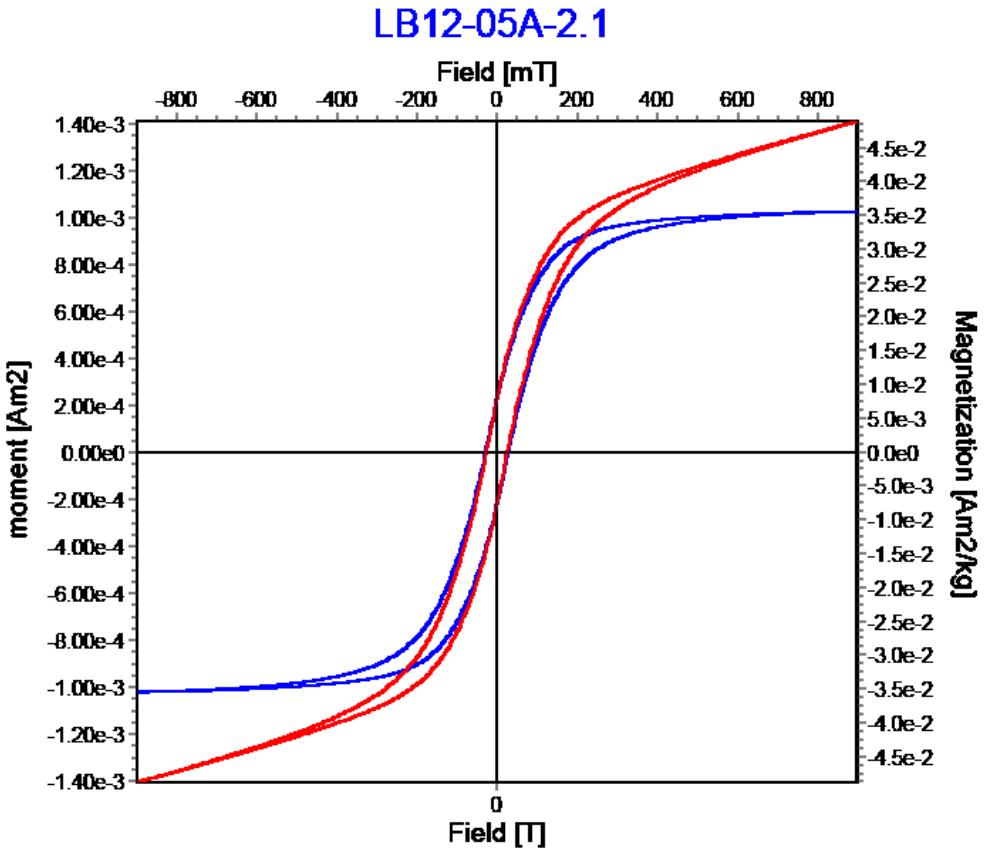
LB12-05A-2.1
Field [mT]
-800 -600 -400 -200 0 200 400 600 800
1.40e-3
1.20e-3
1.00e-3
8.00e-4
6.00e-4
4.00e-4
2.00e-4
0.00e0
-2.00e-4
-4.00e-4
-6.00e-4
-8.00e-4
-1.00e-3
-1.20e-3
-1.40e-3
moment [Am2]
4.5e-2
4.0e-2
3.5e-2
3.0e-2
2.5e-2
2.0e-2
1.5e-2
1.0e-2
5.0e-3
0.0e0
-5.0e-3
-1.0e-2
-1.5e-2
-2.0e-2
-2.5e-2
-3.0e-2
-3.5e-2
-4.0e-2
-4.5e-2
Magnetization [Am2/kg]
0
Field [T]

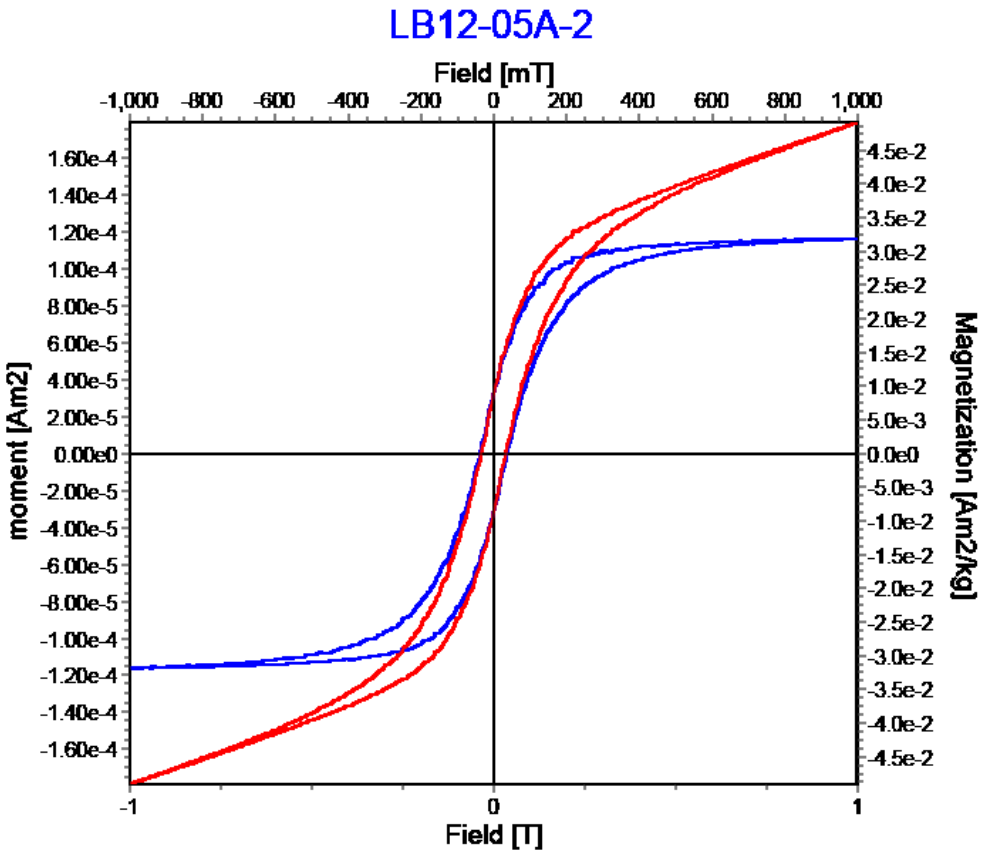
LB12-05A-2
Field [mT]
-1,000 -800 -600 -400 -200 0 200 400 600 800 1,000
moment [Am2]
1.60e-4 1.40e-4 1.20e-4 1.00e-4 8.00e-5 6.00e-5 4.00e-5 2.00e-5 0.00e0 -2.00e-5 -4.00e-5 -6.00e-5 -8.00e-5 -1.00e-4 -1.20e-4 -1.40e-4 -1.60e-4
Magnetization [Am2/kg]
4.5e-2 4.0e-2 3.5e-2 3.0e-2 2.5e-2 2.0e-2 1.5e-2 1.0e-2 5.0e-3 0.0e0 -5.0e-3 -1.0e-2 -1.5e-2 -2.0e-2 -2.5e-2 -3.0e-2 -3.5e-2 -4.0e-2 -4.5e-2
-1 0 1
Field [T]

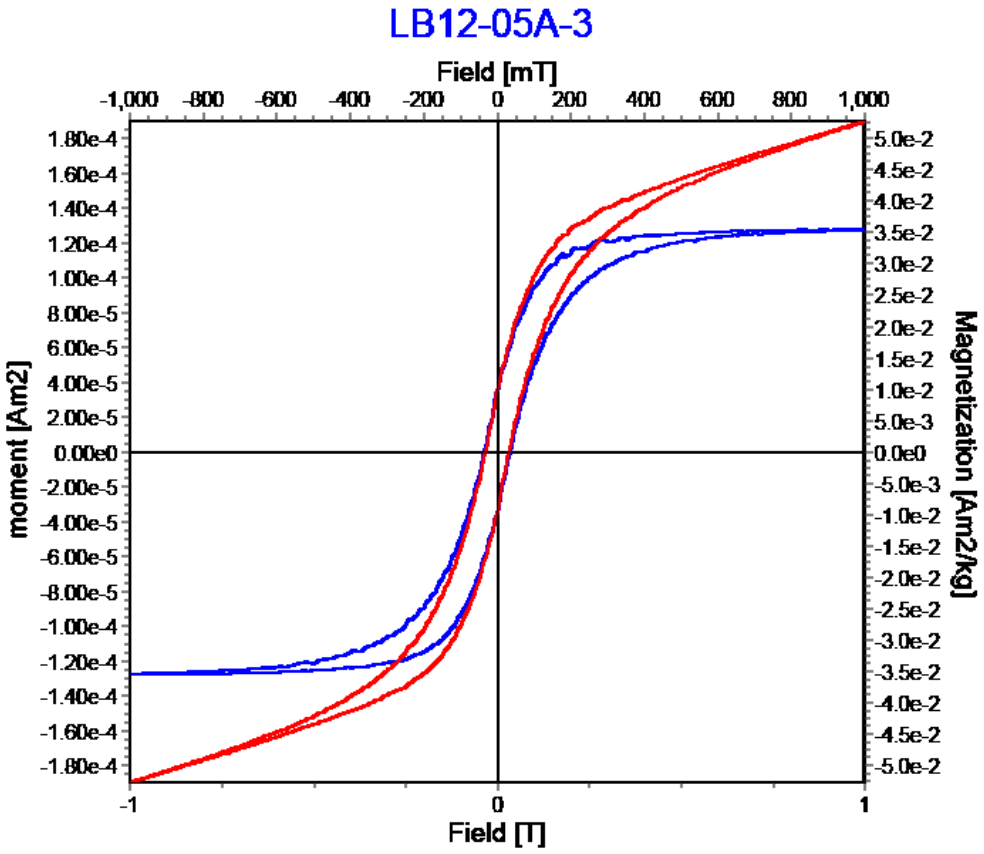
LB12-05A-3
Field [mT]
-1,000 -800 -600 -400 -200 0 200 400 600 800 1,000
moment [Am2]
1.80e-4 1.60e-4 1.40e-4 1.20e-4 1.00e-4 8.00e-5 6.00e-5 4.00e-5 2.00e-5 0.00e0 -2.00e-5 -4.00e-5 -6.00e-5 -8.00e-5 -1.00e-4 -1.20e-4 -1.40e-4 -1.60e-4 -1.80e-4
Magnetization [Am2/kg]
5.0e-2 4.5e-2 4.0e-2 3.5e-2 3.0e-2 2.5e-2 2.0e-2 1.5e-2 1.0e-2 5.0e-3 0.0e0 -5.0e-3 -1.0e-2 -1.5e-2 -2.0e-2 -2.5e-2 -3.0e-2 -3.5e-2 -4.0e-2 -4.5e-2 -5.0e-2
-1 0 1
Field [T]

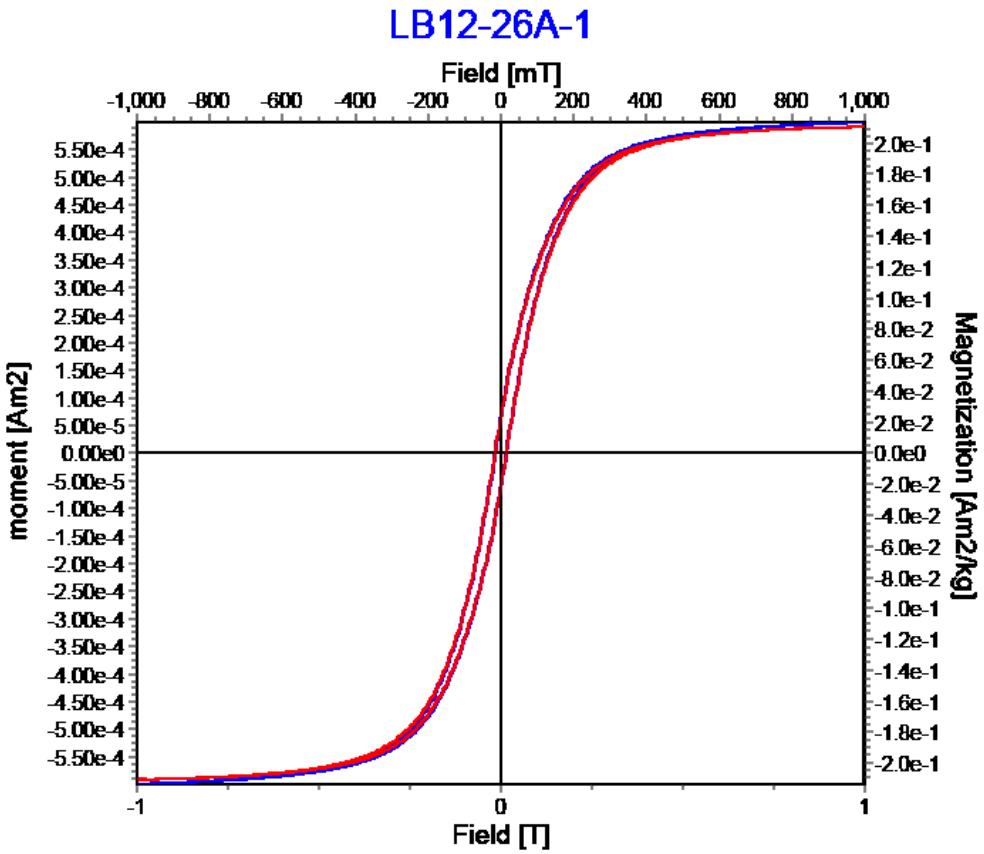
LB12-26A-1
Field [mT]
-1,000 -800 -600 -400 -200 0 200 400 600 800 1,000
moment [Am2]
5.50e-4 5.00e-4 4.50e-4 4.00e-4 3.50e-4 3.00e-4 2.50e-4 2.00e-4 1.50e-4 1.00e-4 5.00e-5 0.00e0 -5.00e-5 -1.00e-4 -1.50e-4 -2.00e-4 -2.50e-4 -3.00e-4 -3.50e-4 -4.00e-4 -4.50e-4 -5.00e-4 -5.50e-4
Magnetization [Am2/kg]
2.0e-1 1.8e-1 1.6e-1 1.4e-1 1.2e-1 1.0e-1 8.0e-2 6.0e-2 4.0e-2 2.0e-2 0.0e0 -2.0e-2 -4.0e-2 -6.0e-2 -8.0e-2 -1.0e-1 -1.2e-1 -1.4e-1 -1.6e-1 -1.8e-1 -2.0e-1
-1 0 1
Field [T]

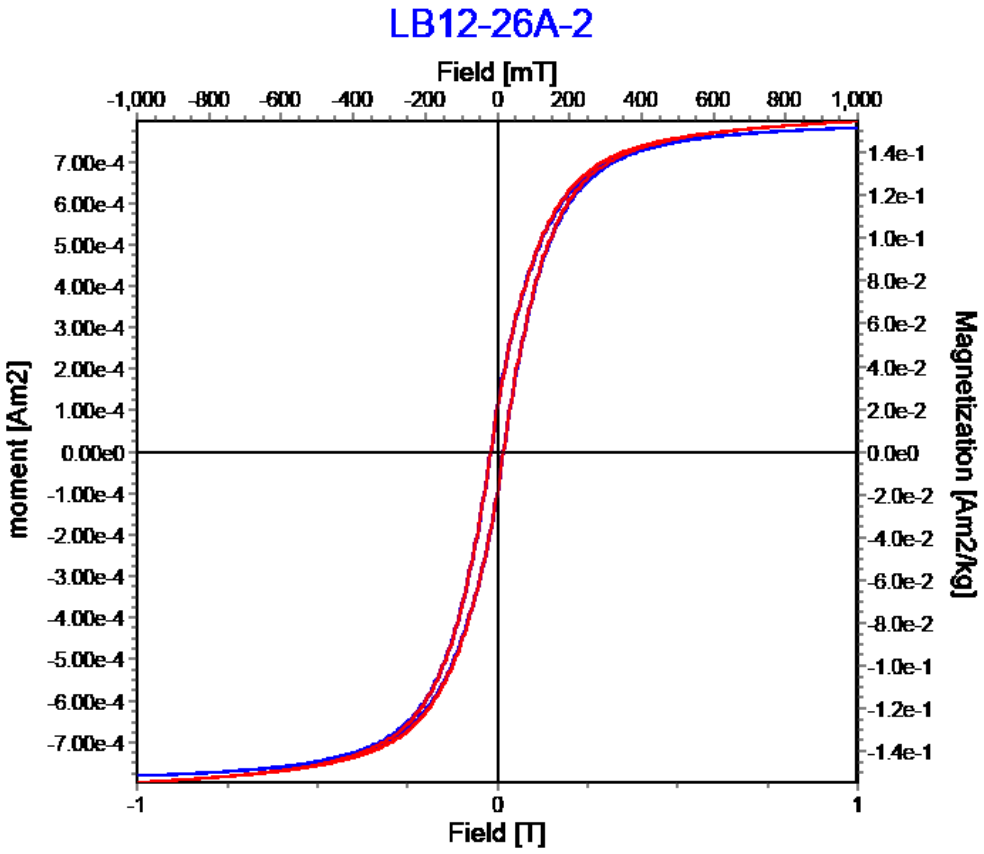
LB12-26A-2
Field [mT]
-1,000 -800 -600 -400 -200 0 200 400 600 800 1,000
moment [Am2]
7.00e-4 6.00e-4 5.00e-4 4.00e-4 3.00e-4 2.00e-4 1.00e-4 0.00e0 -1.00e-4 -2.00e-4 -3.00e-4 -4.00e-4 -5.00e-4 -6.00e-4 -7.00e-4
Magnetization [Am2/kg]
1.4e-1 1.2e-1 1.0e-1 8.0e-2 6.0e-2 4.0e-2 2.0e-2 0.0e0 -2.0e-2 -4.0e-2 -6.0e-2 -8.0e-2 -1.0e-1 -1.2e-1 -1.4e-1
-1 0 1
Field [T]

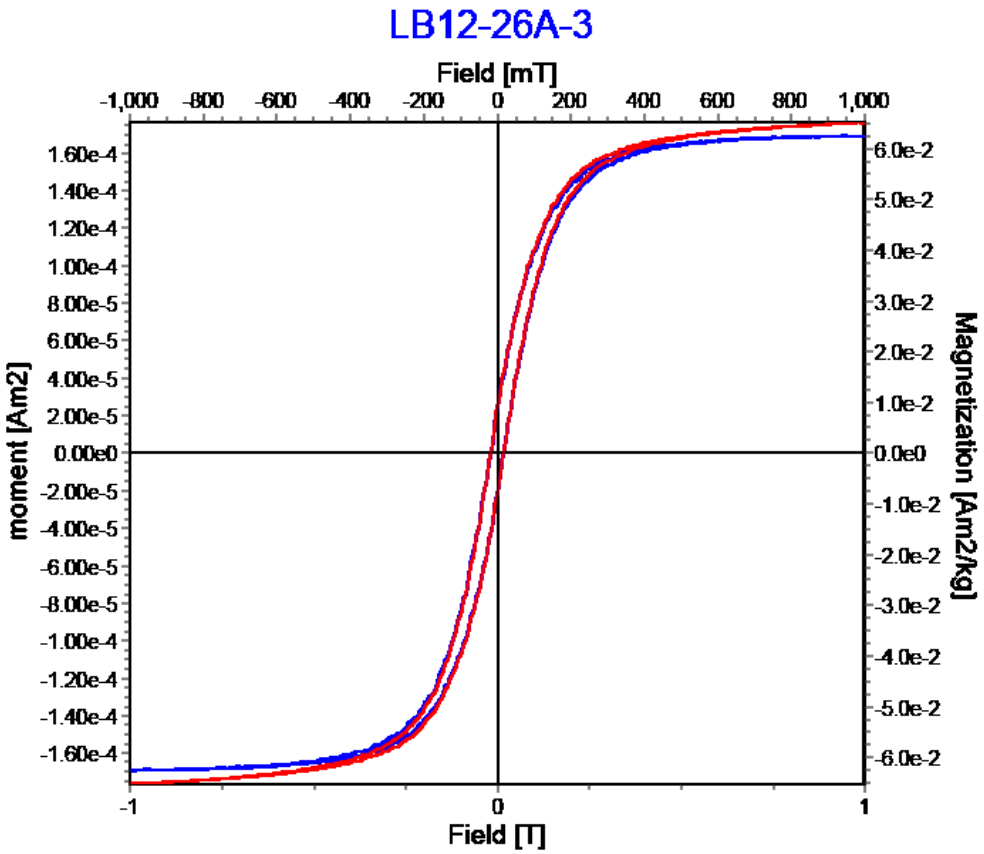
LB12-26A-3
Field [mT]
-1,000 -800 -600 -400 -200 0 200 400 600 800 1,000
moment [Am2]
1.60e-4 1.40e-4 1.20e-4 1.00e-4 8.00e-5 6.00e-5 4.00e-5 2.00e-5 0.00e0 -2.00e-5 -4.00e-5 -6.00e-5 -8.00e-5 -1.00e-4 -1.20e-4 -1.40e-4 -1.60e-4
Magnetization [Am2/kg]
6.0e-2 5.0e-2 4.0e-2 3.0e-2 2.0e-2 1.0e-2 0.0e0 -1.0e-2 -2.0e-2 -3.0e-2 -4.0e-2 -5.0e-2 -6.0e-2
-1 0 1
Field [T]

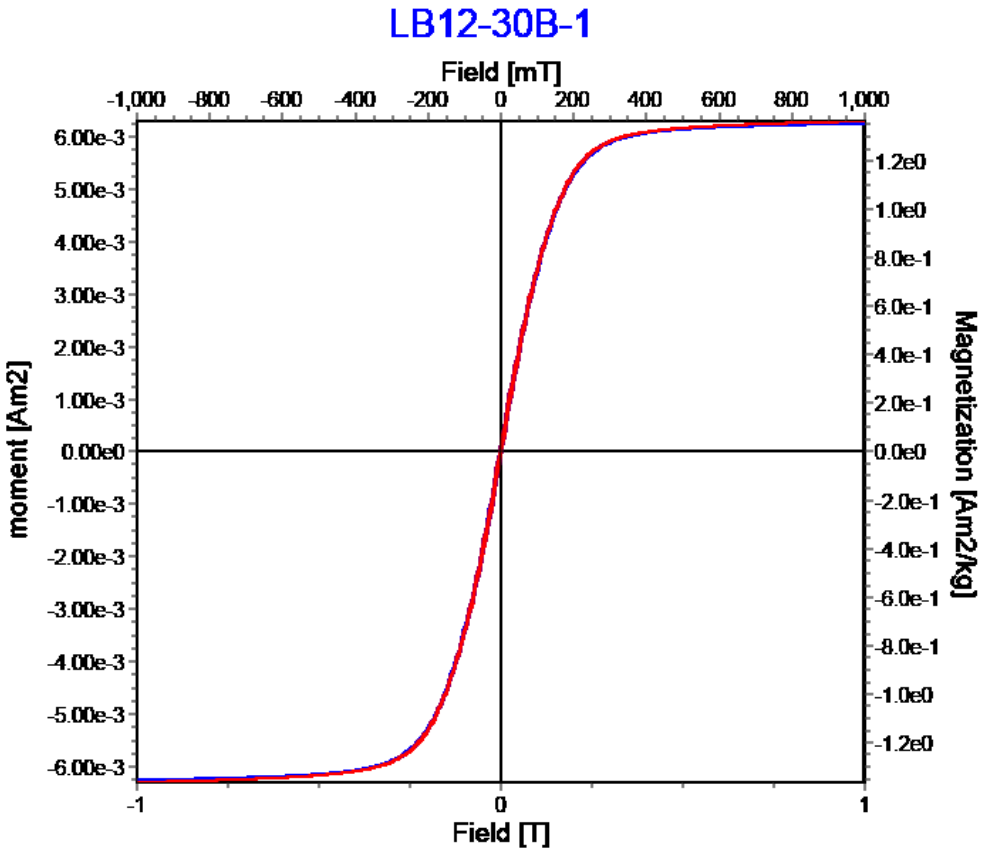
LB12-30B-1
Field [mT]
-1,000 -800 -600 -400 -200 0 200 400 600 800 1,000
moment [Am2]
6.00e-3 5.00e-3 4.00e-3 3.00e-3 2.00e-3 1.00e-3 0.00e0 -1.00e-3 -2.00e-3 -3.00e-3 -4.00e-3 -5.00e-3 -6.00e-3
Magnetization [Am2/kg]
1.2e0 1.0e0 8.0e-1 6.0e-1 4.0e-1 2.0e-1 0.0e0 -2.0e-1 -4.0e-1 -6.0e-1 -8.0e-1 -1.0e0 -1.2e0
-1 0 1
Field [T]

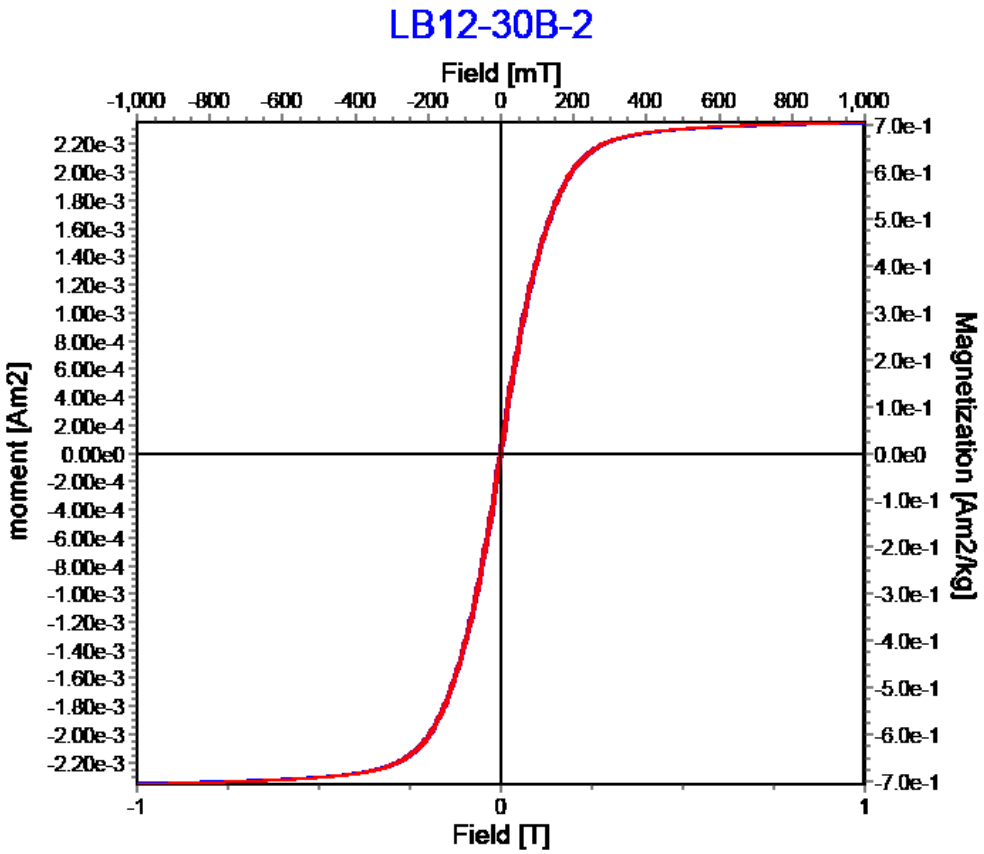
LB12-30B-2
Field [mT]
-1,000 -800 -600 -400 -200 0 200 400 600 800 1,000
moment [Am2]
2.20e-3 2.00e-3 1.80e-3 1.60e-3 1.40e-3 1.20e-3 1.00e-3 8.00e-4 6.00e-4 4.00e-4 2.00e-4 0.00e0 -2.00e-4 -4.00e-4 -6.00e-4 -8.00e-4 -1.00e-3 -1.20e-3 -1.40e-3 -1.60e-3 -1.80e-3 -2.00e-3 -2.20e-3
Magnetization [Am2/kg]
7.0e-1 6.0e-1 5.0e-1 4.0e-1 3.0e-1 2.0e-1 1.0e-1 0.0e0 -1.0e-1 -2.0e-1 -3.0e-1 -4.0e-1 -5.0e-1 -6.0e-1 -7.0e-1
-1 0 1
Field [T]

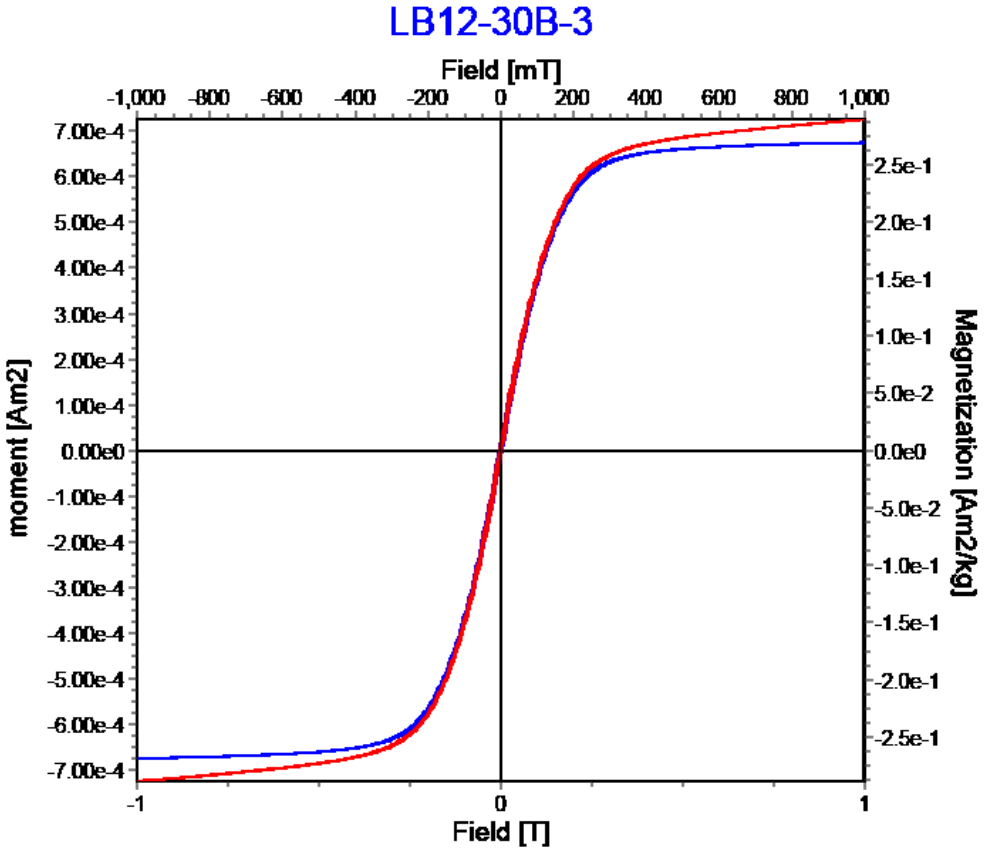
LB12-30B-3
Field [mT]
-1,000 -800 -600 -400 -200 0 200 400 600 800 1,000
moment [Am2]
7.00e-4 6.00e-4 5.00e-4 4.00e-4 3.00e-4 2.00e-4 1.00e-4 0.00e0 -1.00e-4 -2.00e-4 -3.00e-4 -4.00e-4 -5.00e-4 -6.00e-4 -7.00e-4
Magnetization [Am2/kg]
2.5e-1 2.0e-1 1.5e-1 1.0e-1 5.0e-2 0.0e0 -5.0e-2 -1.0e-1 -1.5e-1 -2.0e-1 -2.5e-1
-1 0 1
Field [T]

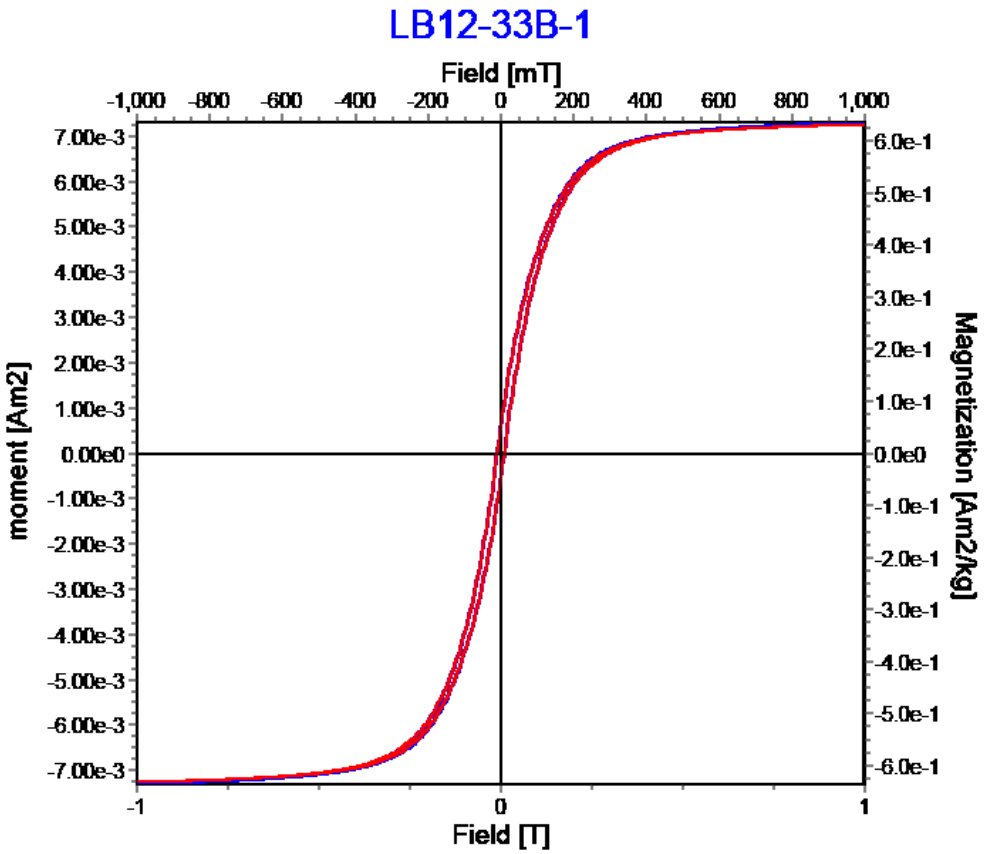
LB12-33B-1
Field [mT]
-1,000 -800 -600 -400 -200 0 200 400 600 800 1,000
7.00e-3
6.00e-3
5.00e-3
4.00e-3
3.00e-3
2.00e-3
1.00e-3
0.00e0
-1.00e-3
-2.00e-3
-3.00e-3
-4.00e-3
-5.00e-3
-6.00e-3
-7.00e-3
moment [Am2]
6.0e-1
5.0e-1
4.0e-1
3.0e-1
2.0e-1
1.0e-1
0.0e0
-1.0e-1
-2.0e-1
-3.0e-1
-4.0e-1
-5.0e-1
-6.0e-1
Magnetization [Am2/kg]
-1
0
1
Field [T]

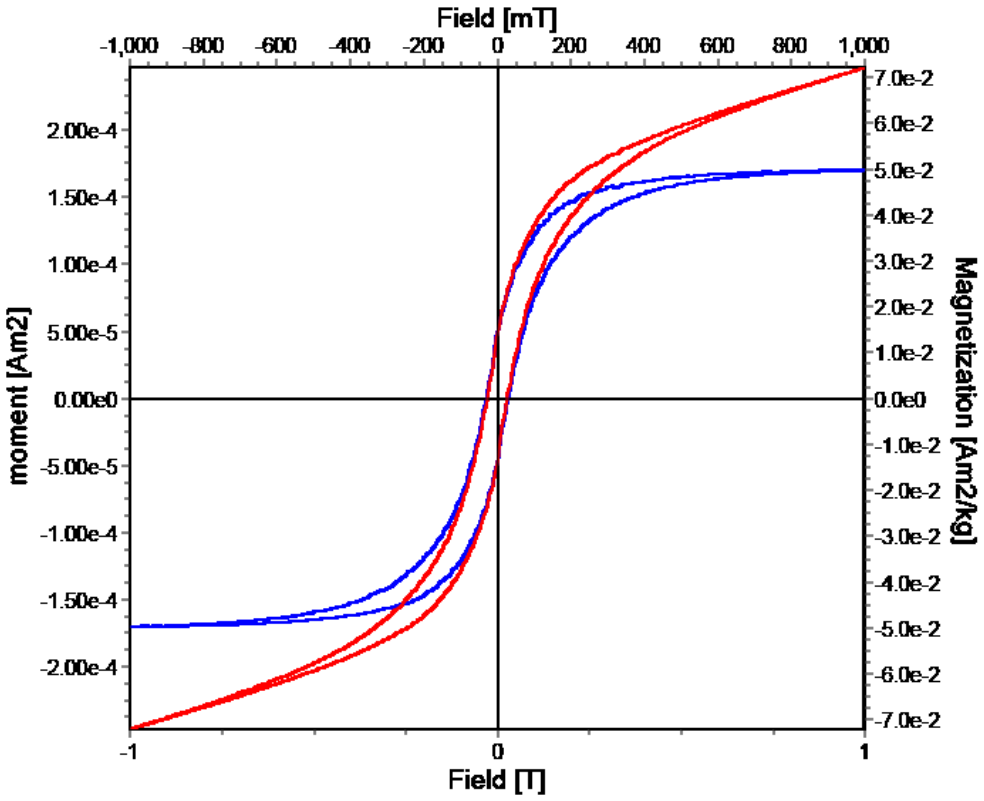
LB12-46B-1
Field [mT]
-1,000 -800 -600 -400 -200 0 200 400 600 800 1,000
2.00e-4
1.50e-4
1.00e-4
5.00e-5
0.00e0
-5.00e-5
-1.00e-4
-1.50e-4
-2.00e-4
moment [Am2]
7.0e-2
6.0e-2
5.0e-2
4.0e-2
3.0e-2
2.0e-2
1.0e-2
0.0e0
-1.0e-2
-2.0e-2
-3.0e-2
-4.0e-2
-5.0e-2
-6.0e-2
-7.0e-2
Magnetization [Am2/kg]
-1
0
1
Field [T]

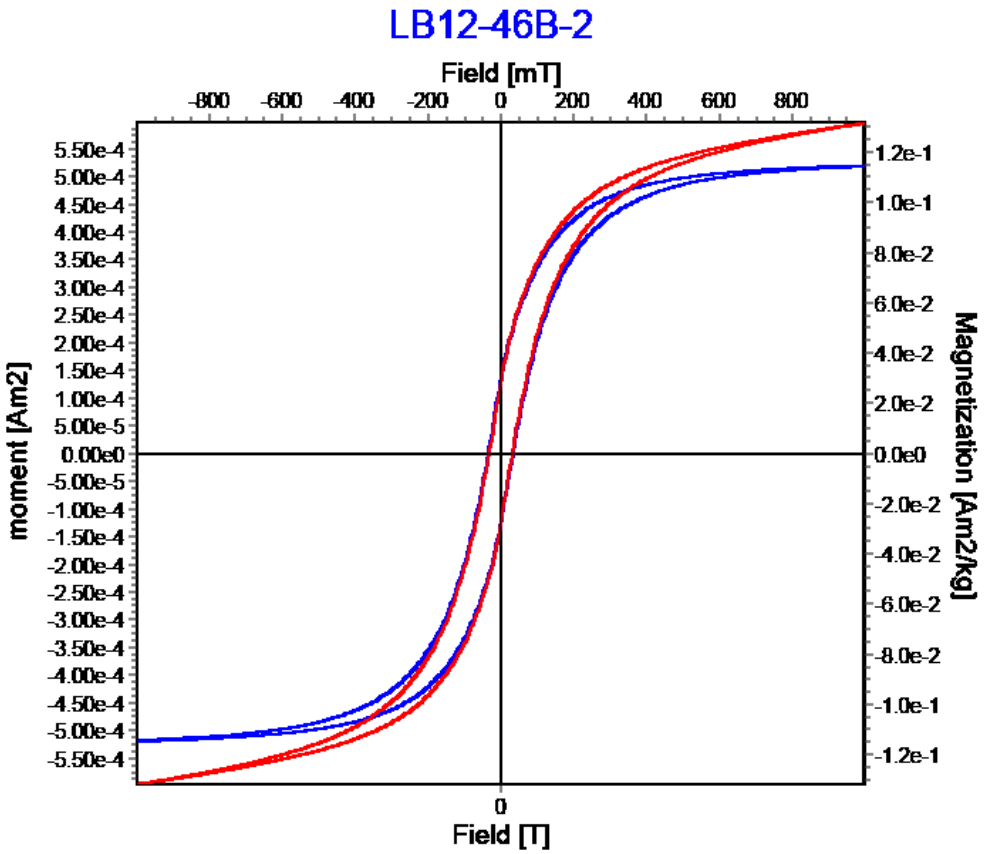
LB12-46B-2
Field [mT]
-800 -600 -400 -200 0 200 400 600 800
moment [Am2]
5.50e-4 5.00e-4 4.50e-4 4.00e-4 3.50e-4 3.00e-4 2.50e-4 2.00e-4 1.50e-4 1.00e-4 5.00e-5 0.00e0 -5.00e-5 -1.00e-4 -1.50e-4 -2.00e-4 -2.50e-4 -3.00e-4 -3.50e-4 -4.00e-4 -4.50e-4 -5.00e-4 -5.50e-4
Magnetization [Am2/kg]
1.2e-1 1.0e-1 8.0e-2 6.0e-2 4.0e-2 2.0e-2 0.0e0 -2.0e-2 -4.0e-2 -6.0e-2 -8.0e-2 -1.0e-1 -1.2e-1
0
Field [T]

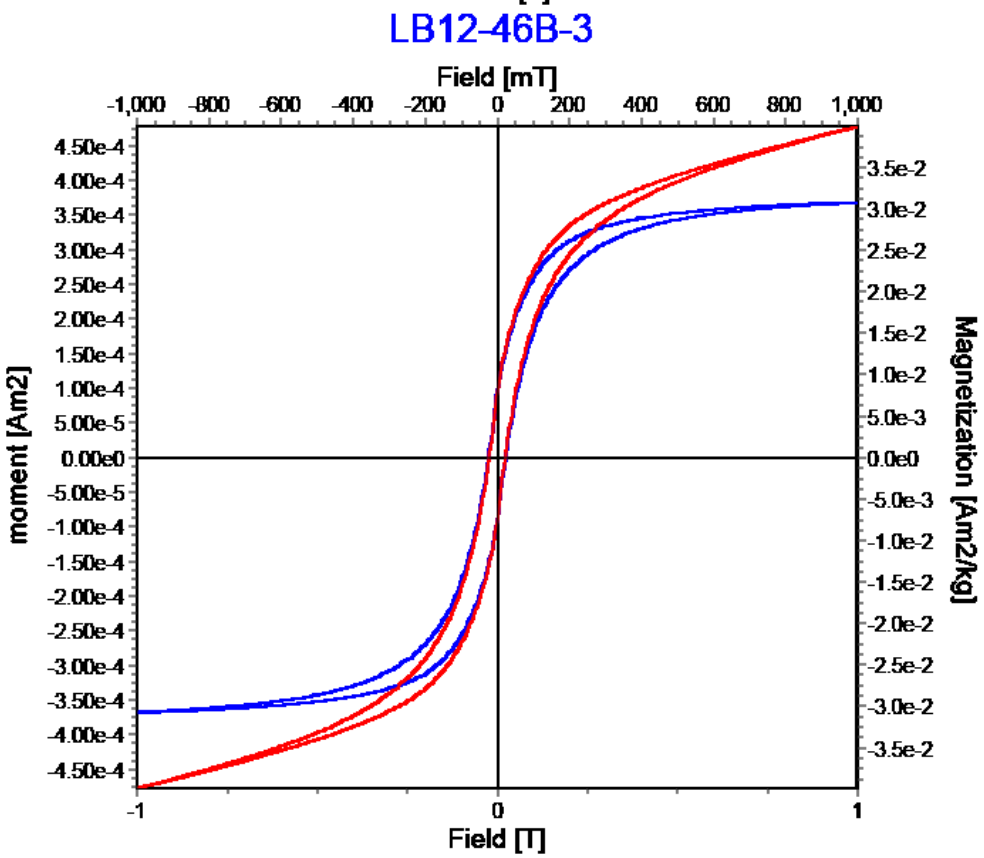
LB12-46B-3
Field [mT]
-1,000 -800 -600 -400 -200 0 200 400 600 800 1,000
moment [Am2]
4.50e-4 4.00e-4 3.50e-4 3.00e-4 2.50e-4 2.00e-4 1.50e-4 1.00e-4 5.00e-5 0.00e0 -5.00e-5 -1.00e-4 -1.50e-4 -2.00e-4 -2.50e-4 -3.00e-4 -3.50e-4 -4.00e-4 -4.50e-4
Magnetization [Am2/kg]
3.5e-2 3.0e-2 2.5e-2 2.0e-2 1.5e-2 1.0e-2 5.0e-3 0.0e0 -5.0e-3 -1.0e-2 -1.5e-2 -2.0e-2 -2.5e-2 -3.0e-2 -3.5e-2
-1 0 1
Field [T]

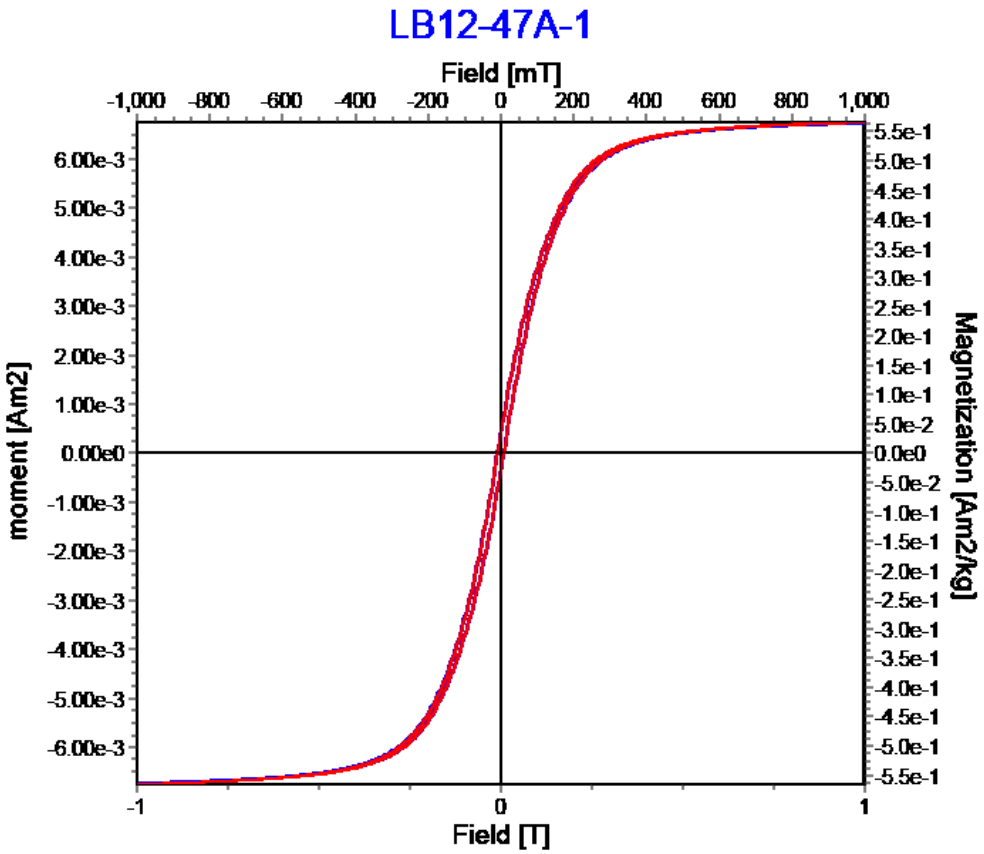
LB12-47A-1
Field [mT]
-1,000 -800 -600 -400 -200 0 200 400 600 800 1,000
6.00e-3
5.00e-3
4.00e-3
3.00e-3
2.00e-3
1.00e-3
0.00e0
-1.00e-3
-2.00e-3
-3.00e-3
-4.00e-3
-5.00e-3
-6.00e-3
moment [Am2]
5.5e-1
5.0e-1
4.5e-1
4.0e-1
3.5e-1
3.0e-1
2.5e-1
2.0e-1
1.5e-1
1.0e-1
5.0e-2
0.0e0
-5.0e-2
-1.0e-1
-1.5e-1
-2.0e-1
-2.5e-1
-3.0e-1
-3.5e-1
-4.0e-1
-4.5e-1
-5.0e-1
-5.5e-1
Magnetization [Am2/kg]
-1
0
1
Field [T]

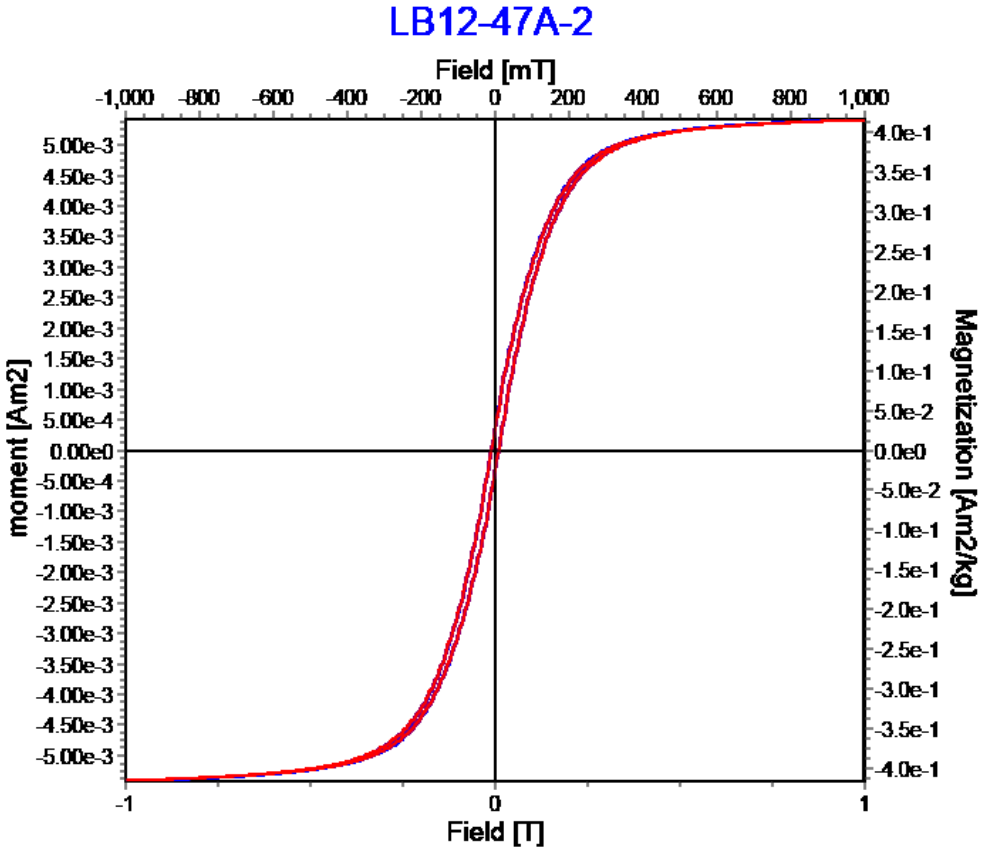
LB12-47A-2
Field [mT]
-1,000 -800 -600 -400 -200 0 200 400 600 800 1,000
5.00e-3
4.50e-3
4.00e-3
3.50e-3
3.00e-3
2.50e-3
2.00e-3
1.50e-3
1.00e-3
5.00e-4
0.00e0
-5.00e-4
-1.00e-3
-1.50e-3
-2.00e-3
-2.50e-3
-3.00e-3
-3.50e-3
-4.00e-3
-4.50e-3
-5.00e-3
moment [Am2]
4.0e-1
3.5e-1
3.0e-1
2.5e-1
2.0e-1
1.5e-1
1.0e-1
5.0e-2
0.0e0
-5.0e-2
-1.0e-1
-1.5e-1
-2.0e-1
-2.5e-1
-3.0e-1
-3.5e-1
-4.0e-1
Magnetization [Am2/kg]
-1
0
1
Field [T]

COUNTRY ROCK (NON LOCH BORRALAN)

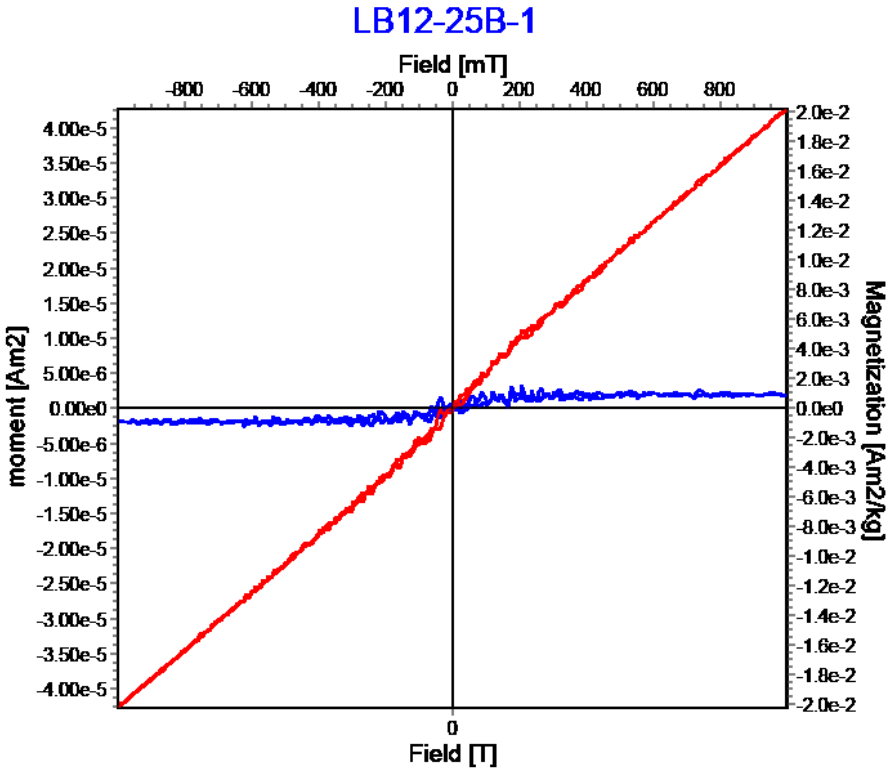

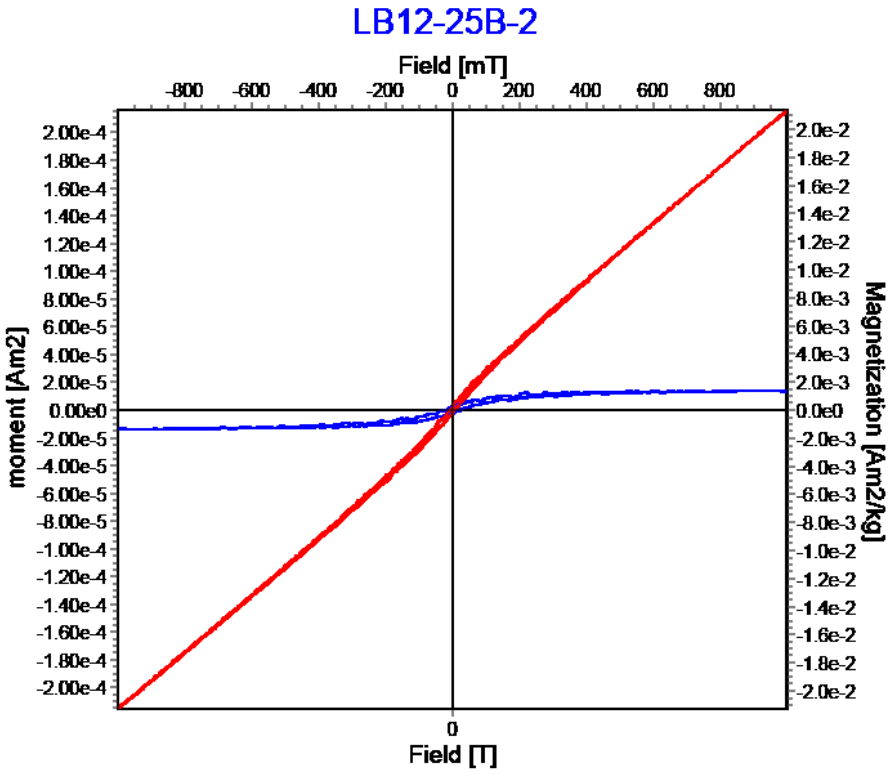

Appendix B: Bulk AMS Data

Note: Values omitted from analysis denoted with (*). Criteria for sample omissions are described in Chapter 4: Results. Samples that were chipped or repaired (glued) denoted with (X) at the end of the sample name. K_m, mean bulk susceptibility (SI $x10^{-6}$); L, K_1/K_2; F, K_2/K_3; Pj, anisotropy magnitude; T, anisotropy shape.

Early Suite Parameters

Name	Km	STDev	L	STDev	F	STDev	P	STDev	P_j	STDev	T	STDev	U	STDev
LB08-03B1.1	954.068	14481.478	1.007	0.021	1.014	0.055	1.021	0.078	1.021	0.085	0.329	0.233	0.325	0.119
LB08-03B2.1	802.621	14588.567	1.012	0.017	1.005	0.062	1.017	0.081	1.017	0.088	-0.384	0.272	-0.387	0.385
LB08-03B2.2*	854.555	14551.844	1.009	0.019	1.801	0.501	1.818	0.485	1.984	0.596	0.969	0.685	0.959	0.567
LB12-04C1.1	10968.560	7400.162	1.021	0.011	1.078	0.010	1.100	0.022	1.106	0.025	0.573	0.405	0.557	0.283
LB12-04C2.1	21565.480	92.992	1.010	0.019	1.066	0.019	1.077	0.039	1.083	0.041	0.733	0.518	0.725	0.402
LB12-12A1.1	11654.300	6915.271	1.038	0.001	1.107	0.010	1.150	0.013	1.155	0.010	0.459	0.325	0.431	0.194
LB12-12B1.1	5901.418	10983.173	1.057	0.015	1.117	0.017	1.181	0.035	1.184	0.030	0.332	0.235	0.295	0.098
LB12-12B2.1	6585.384	10499.536	1.073	0.026	1.087	0.004	1.167	0.025	1.167	0.018	0.084	0.059	0.045	0.079
LB12-14B1.1	721.664	14645.812	1.005	0.022	1.003	0.063	1.008	0.087	1.008	0.094	-0.224	0.158	-0.226	0.271
LB12-14B2.1	646.627	14698.871	1.003	0.024	1.001	0.065	1.004	0.090	1.004	0.097	-0.609	0.431	-0.610	0.542
LB12-14B2.2X	593.487	14736.447	1.004	0.023	1.005	0.062	1.009	0.087	1.009	0.094	0.045	0.032	0.042	0.081
LB12-15A1.1	21508.910	52.991	1.052	0.011	1.042	0.036	1.095	0.026	1.096	0.032	-0.103	0.073	-0.126	0.200
LB12-15A2.1	22924.740	1054.133	1.044	0.005	1.036	0.040	1.082	0.035	1.082	0.042	-0.094	0.066	-0.113	0.191
LB12-15A2.2	26821.250	3809.382	1.050	0.010	1.035	0.041	1.088	0.031	1.088	0.038	-0.171	0.121	-0.191	0.246
LB12-15B1.1	5350.216	11372.932	1.071	0.025	1.067	0.018	1.142	0.007	1.142	0.001	-0.028	0.020	-0.061	0.154
LB12-15B2.1	4707.268	11827.564	1.089	0.037	1.076	0.012	1.171	0.028	1.171	0.021	-0.073	0.052	-0.113	0.191
LB12-15B2.2X	4554.125	11935.853	1.080	0.031	1.066	0.019	1.151	0.014	1.151	0.007	-0.092	0.065	-0.127	0.201
LB12-16A1.1	11443.510	7064.322	1.041	0.003	1.040	0.037	1.082	0.035	1.082	0.042	-0.013	0.009	-0.033	0.134
LB12-16A1.2	23447.640	1423.880	1.038	0.001	1.060	0.023	1.100	0.022	1.101	0.028	0.212	0.150	0.189	0.023
LB12-16B1.1	79168.050	40824.159	1.059	0.016	1.082	0.007	1.146	0.010	1.146	0.003	0.157	0.111	0.124	0.023
LB12-16B2.1	95212.410	52169.235	1.038	0.001	1.117	0.017	1.160	0.020	1.167	0.018	0.493	0.349	0.464	0.217
LB12-17B1.1	45908.050	17305.788	1.025	0.008	1.138	0.032	1.167	0.025	1.181	0.028	0.676	0.478	0.655	0.352
LB12-17B2.1	90686.980	48969.273	1.009	0.019	1.084	0.006	1.094	0.027	1.104	0.026	0.797	0.564	0.789	0.447
Mean	21433.970		1.036		1.092		1.132		1.141		0.177		0.157	
Median	10968.560		1.038		1.066		1.100		1.104		0.084		0.045	

Max	95212.410		1.089		1.801		1.818		1.984		0.969		0.959
Min	593.487		1.003		1.001		1.004		1.004		-0.609		-0.610

Early Suite Susceptibility Axes Orientations

Name	K_1dec	K_1inc	K_2dec	K_2inc	K_3dec	K_3inc
LB08-03B1.1	71.400	59.900	226.900	27.800	322.600	10.600
LB08-03B2.1	116.100	2.400	216.400	76.800	25.600	12.900
LB08-03B2.2*	256.500	67.900	7.500	8.300	100.600	20.400
LB12-04C1.1	73.400	26.400	175.500	23.000	300.800	53.700
LB12-04C2.1	56.400	21.800	160.100	30.600	296.800	50.900
LB12-12A1.1	16.200	25.300	258.200	44.900	125.100	34.500
LB12-12B1.1	2.900	32.300	198.100	56.800	97.400	7.000
LB12-12B2.1	19.000	13.100	148.100	69.700	285.400	15.200
LB12-14B1.1	142.900	20.300	258.500	49.500	38.900	33.300
LB12-14B2.1	157.000	29.800	279.100	42.900	45.500	32.600
LB12-14B2.2X	128.300	37.400	300.800	52.300	35.600	3.600
LB12-15A1.1	223.400	27.800	132.500	1.700	39.200	62.100
LB12-15A2.1	220.000	26.300	310.400	0.700	41.800	63.700
LB12-15A2.2	303.000	51.900	197.200	12.000	98.400	35.500
LB12-15B1.1	124.600	19.000	215.900	3.900	317.100	70.500
LB12-15B2.1	119.300	18.500	211.300	6.000	318.500	70.400
LB12-15B2.2X	114.500	17.300	22.600	6.000	274.100	71.600
LB12-16A1.1	84.000	87.500	257.700	2.400	347.700	0.300
LB12-16A1.2	176.800	79.200	73.300	2.600	342.800	10.500
LB12-16B1.1	114.500	33.700	3.300	28.500	242.900	43.000
LB12-16B2.1	121.100	27.100	19.800	20.900	257.200	54.600
LB12-17B1.1	36.600	21.900	174.600	61.600	299.400	17.200

LB12-17B2.1	175.200	19.200	49.400	59.200	273.700	23.100

Late Suite Parameters

Name	Km	STDev	L	STDev	F	STDev	P	STDev	P_j	STDev	T	STDev	U	STDev
LB08-04B1.1*	8056.166	342.156	1.089	0.043	1.162	0.071	1.266	0.123	1.269	0.121	0.275	0.078	0.220	0.049
LB08-04B2.1	13801.400	3720.338	1.038	0.007	1.055	0.005	1.095	0.002	1.095	0.003	0.185	0.014	0.163	0.009
LB08-05A1.1	15365.790	4826.529	1.012	0.012	1.007	0.039	1.019	0.052	1.020	0.056	-0.287	0.320	-0.292	0.313
LB08-05A2.1	12824.270	3029.403	1.011	0.012	1.018	0.031	1.030	0.044	1.030	0.048	0.239	0.052	0.232	0.058
LB08-05A2.2X	10990.610	1732.810	1.013	0.011	1.014	0.034	1.027	0.046	1.027	0.051	0.061	0.074	0.054	0.068
LB08-05B1.1	15344.300	4811.333	1.012	0.012	1.011	0.036	1.023	0.049	1.023	0.053	-0.052	0.154	-0.058	0.147
LB08-05B2.1*	14765.870	4402.322	1.011	0.012	1.831	0.544	1.852	0.537	2.025	0.655	0.964	0.565	0.951	0.566
LB08-06B1.1	286.215	5836.340	1.008	0.015	1.044	0.013	1.053	0.028	1.057	0.029	0.682	0.365	0.675	0.371
LB08-06B2.1	219.994	5883.166	1.012	0.012	1.068	0.004	1.081	0.008	1.088	0.007	0.683	0.366	0.672	0.369
LB08-07A1.1	746.327	5510.992	1.022	0.005	1.018	0.031	1.040	0.037	1.040	0.041	-0.101	0.188	-0.111	0.185
LB08-07A2.1X	430.971	5733.983	1.030	0.001	1.020	0.030	1.051	0.029	1.051	0.034	-0.191	0.252	-0.203	0.250
LB08-08A1.1X	14306.680	4077.625	1.023	0.004	1.091	0.021	1.116	0.016	1.122	0.017	0.593	0.302	0.575	0.300
LB08-08B1.1	2114.594	4543.481	1.065	0.026	1.031	0.022	1.098	0.004	1.100	0.001	-0.343	0.359	-0.363	0.363
LB08-10A1.1	9678.040	804.683	1.031	0.002	1.055	0.005	1.088	0.003	1.089	0.007	0.273	0.076	0.254	0.073
LB08-10A1.2X	7756.329	554.172	1.033	0.003	1.047	0.011	1.082	0.008	1.082	0.012	0.174	0.006	0.155	0.003
LB08-10A2.1	10825.080	1615.762	1.032	0.002	1.041	0.015	1.075	0.013	1.075	0.017	0.120	0.032	0.102	0.034
LB08-10A2.2	10668.890	1505.319	1.033	0.003	1.047	0.011	1.081	0.008	1.082	0.012	0.177	0.008	0.158	0.005
LB08-10B1.1	10221.510	1188.974	1.017	0.008	1.026	0.025	1.044	0.034	1.044	0.039	0.220	0.039	0.210	0.042
LB08-10B1.2	7028.327	1068.947	1.025	0.003	1.058	0.003	1.085	0.005	1.087	0.008	0.388	0.157	0.371	0.156
LB08-11A1.1	13042.040	3183.390	1.037	0.006	1.063	0.001	1.102	0.007	1.104	0.004	0.258	0.066	0.236	0.060
LB08-11B1.1	15213.380	4718.759	1.027	0.001	1.072	0.007	1.101	0.006	1.105	0.005	0.438	0.193	0.418	0.189
LB08-11B2.1	16362.910	5531.600	1.019	0.007	1.066	0.003	1.086	0.005	1.091	0.005	0.535	0.261	0.520	0.261
LB08-12B1.1X*	40874.780	22864.109	1.008	0.015	1.055	0.005	1.064	0.020	1.069	0.021	0.728	0.398	0.720	0.403

LB12-03A1.1X	14153.510	3969.318	1.055	0.019	1.035	0.019	1.092	0.000	1.093	0.004	-0.210	0.265	-0.231	0.270
LB12-03A2.1	10698.380	1526.172	1.044	0.011	1.024	0.027	1.069	0.017	1.070	0.020	-0.295	0.326	-0.310	0.326
LB12-03B1.1X	9450.021	643.449	1.022	0.005	1.096	0.024	1.121	0.020	1.129	0.022	0.614	0.317	0.596	0.315
LB12-05A1.1	752.280	5506.783	1.005	0.017	1.012	0.035	1.018	0.053	1.018	0.057	0.373	0.147	0.369	0.154
LB12-05A1.2	820.589	5458.481	1.010	0.013	1.009	0.037	1.019	0.052	1.019	0.056	-0.026	0.135	-0.030	0.128
LB12-05A2.1	808.072	5467.332	1.007	0.015	1.037	0.018	1.044	0.034	1.047	0.036	0.683	0.366	0.677	0.372
LB12-05A3.1	633.986	5590.429	1.000	0.020	1.005	0.040	1.005	0.062	1.006	0.065	0.965	0.565	0.965	0.576
LB12-11A1.1	446.528	5722.982	1.034	0.004	1.009	0.037	1.043	0.035	1.045	0.038	-0.583	0.529	-0.589	0.523
LB12-11A1.2X*	286.901	5835.856	1.096	0.048	1.206	0.102	1.322	0.162	1.329	0.163	0.343	0.126	0.281	0.092
LB12-21A1.1	3909.317	3274.421	1.051	0.016	1.020	0.030	1.073	0.014	1.075	0.017	-0.424	0.417	-0.438	0.416
LB12-21A2.1	5699.766	2008.382	1.042	0.009	1.023	0.028	1.067	0.018	1.068	0.022	-0.284	0.318	-0.299	0.318
LB12-22B1.1	15659.060	5033.902	1.021	0.005	1.027	0.025	1.049	0.031	1.049	0.035	0.119	0.033	0.108	0.030
LB12-22B2.1	13192.160	3289.541	1.058	0.021	1.006	0.040	1.064	0.020	1.071	0.019	-0.800	0.683	-0.805	0.676
LB12-22B2.2X	13474.530	3489.206	1.036	0.005	1.008	0.038	1.044	0.034	1.047	0.036	-0.644	0.572	-0.650	0.566
LB12-26A1.1	2214.455	4472.869	1.018	0.008	1.049	0.009	1.068	0.017	1.071	0.019	0.463	0.210	0.450	0.212
LB12-26A2.1	3319.279	3691.640	1.025	0.003	1.030	0.023	1.055	0.027	1.055	0.031	0.095	0.050	0.082	0.048
LB12-27B1.1	402.613	5754.035	1.015	0.010	1.019	0.030	1.034	0.042	1.034	0.046	0.114	0.036	0.105	0.032
LB12-27B2.1	376.946	5772.184	1.011	0.012	1.032	0.021	1.043	0.035	1.045	0.038	0.489	0.229	0.481	0.234
LB12-28B1.1	4759.023	2673.588	1.002	0.019	1.011	0.036	1.013	0.056	1.014	0.060	0.630	0.329	0.628	0.338
LB12-28B1.2	5507.531	2144.313	1.013	0.011	1.004	0.041	1.017	0.054	1.018	0.057	-0.547	0.504	-0.550	0.495
LB12-28B2.1	5913.066	1857.556	1.009	0.014	1.006	0.040	1.015	0.055	1.015	0.059	-0.161	0.231	-0.165	0.223
LB12-30A1.1	13577.470	3561.996	1.052	0.017	1.098	0.026	1.154	0.043	1.157	0.041	0.299	0.094	0.267	0.082
LB12-30A1.2	12375.120	2711.806	1.049	0.014	1.049	0.009	1.100	0.005	1.100	0.001	0.009	0.111	-0.015	0.117
LB12-30B1.1	17937.870	6645.264	1.044	0.011	1.012	0.035	1.057	0.025	1.060	0.027	-0.564	0.516	-0.574	0.512
LB12-30B1.2	21461.760	9137.031	1.050	0.015	1.021	0.029	1.073	0.014	1.075	0.017	-0.396	0.397	-0.411	0.397
LB12-30B1.2X	10271.470	1224.301	1.020	0.006	1.095	0.023	1.118	0.018	1.126	0.019	0.635	0.332	0.619	0.331
LB12-37A1.1	2158.562	4512.391	1.035	0.004	1.032	0.021	1.068	0.017	1.068	0.022	-0.042	0.147	-0.058	0.147

LB12-40B1.1	1219.735	5176.242	1.024	0.003	1.082	0.014	1.108	0.011	1.113	0.010	0.530	0.258	0.512	0.256
LB12-40B2.1	1606.786	4902.556	1.014	0.010	1.103	0.029	1.119	0.019	1.130	0.022	0.747	0.411	0.734	0.413
LB12-47B1.1*	8611.230	50.334	1.049	0.014	1.221	0.112	1.282	0.134	1.301	0.143	0.613	0.317	0.573	0.299
Mean	8540.047		1.029		1.062		1.093		1.099		0.165		0.151	
Median	8611.230		1.024		1.032		1.068		1.071		0.185		0.163	
Max	40874.780		1.096		1.831		1.852		2.025		0.965		0.965	
Min	219.994		1.000		1.004		1.005		1.006		-0.800		-0.805	

Late Suite Susceptibility Axes Orientations

Name	K_1dec	K_1inc	K_2dec	K_2inc	K_3dec	K_3inc
LB08-04B1.1*	281.200	15.000	18.900	26.400	164.600	59.000
LB08-04B2.1	292.000	34.300	185.000	23.200	68.200	46.600
LB08-05A1.1	301.300	22.700	189.400	41.700	51.600	39.700
LB08-05A2.1	297.300	56.900	136.400	31.600	41.000	8.800
LB08-05A2.2X	309.600	48.700	162.300	36.500	59.500	16.600
LB08-05B1.1	174.300	48.000	297.100	26.000	43.700	30.400
LB08-05B2.1*	200.600	24.400	306.200	30.800	79.300	48.900
LB08-06B1.1	309.800	5.500	40.000	1.700	147.600	84.300
LB08-06B2.1	335.000	28.700	72.400	13.200	184.300	57.900
LB08-07A1.1	179.500	8.100	87.900	11.200	304.700	76.100
LB08-07A2.1X	142.900	6.000	52.600	3.500	292.900	83.100
LB08-08A1.1X	200.200	32.000	70.200	45.800	308.700	27.000
LB08-08B1.1	206.900	2.600	65.300	86.700	297.000	2.000
LB08-10A1.1	31.700	0.300	121.900	31.700	301.300	58.300
LB08-10A1.2X	52.800	9.800	149.400	33.800	308.800	54.400
LB08-10A2.1	192.400	13.900	93.200	32.800	302.100	53.600
LB08-10A2.2	21.300	2.300	113.300	40.700	288.700	49.200

LB08-10B1.1	222.400	2.300	131.100	29.300	316.500	60.600
LB08-10B1.2	38.500	12.600	134.700	25.900	284.900	60.800
LB08-11A1.1	176.600	34.100	85.500	1.700	353.000	55.800
LB08-11B1.1	0.700	8.500	269.100	10.100	130.000	76.800
LB08-11B2.1	2.500	9.400	270.000	14.600	124.200	72.500
LB08-12B1.1X*	241.800	17.200	138.100	37.500	351.400	47.400
LB12-03A1.1X	128.000	16.600	29.300	26.700	246.300	57.800
LB12-03A2.1	123.400	6.000	27.300	45.500	219.200	43.900
LB12-03B1.1X	81.100	18.300	336.000	38.300	191.100	46.000
LB12-05A1.1	199.500	30.700	310.200	30.900	75.000	43.700
LB12-05A1.2	192.500	27.500	296.000	24.100	60.800	51.900
LB12-05A2.1	188.500	53.700	355.100	35.500	89.700	6.400
LB12-05A3.1	317.600	29.300	207.600	31.300	81.000	44.500
LB12-11A1.1	332.200	0.400	242.100	13.100	63.800	76.900
LB12-11A1.2X*	1.800	1.000	94.400	69.400	271.400	20.600
LB12-21A1.1	26.500	80.200	197.700	9.700	288.000	1.500
LB12-21A2.1	106.400	84.300	350.900	2.400	260.700	5.100
LB12-22B1.1	5.100	19.500	269.900	14.200	146.100	65.500
LB12-22B2.1	19.700	33.800	283.000	9.900	178.900	54.400
LB12-22B2.2X	29.000	30.300	293.700	8.900	189.100	58.200
LB12-26A1.1	75.700	59.700	314.300	17.000	216.300	24.300
LB12-26A2.1	90.300	53.800	284.400	35.400	189.600	6.700
LB12-27B1.1	3.200	7.600	115.900	70.900	270.800	17.400
LB12-27B2.1	0.900	3.600	99.400	66.700	269.300	23.000
LB12-28B1.1	353.100	3.700	261.500	23.600	91.500	66.000
LB12-28B1.2	209.800	5.000	301.400	17.900	104.600	71.400
LB12-28B2.1	205.100	16.200	105.000	31.100	318.700	54.100

LB12-30A1.1	232.100	25.500	139.200	6.100	36.700	63.700
LB12-30A1.2	238.900	23.200	141.700	16.200	19.900	61.200
LB12-30B1.1	223.200	15.300	318.000	16.800	93.200	66.900
LB12-30B1.2	199.900	0.700	290.000	7.400	104.400	82.600
LB12-30B1.2X	268.700	20.100	165.900	31.200	26.200	51.500
LB12-37A1.1	112.000	13.900	213.900	39.900	6.800	46.800
LB12-40B1.1	177.600	60.100	23.900	27.300	288.000	11.300
LB12-40B2.1	162.400	71.200	19.200	15.200	286.200	10.700
LB12-47B1.1*	24.100	1.900	292.100	47.000	115.900	43.000